Electrical and thermoelectric properties of cuprate superconductors under pressure and in high magnetic fields

Propriétés électriques et thermoélectriques des cuprates supraconducteurs sous pression et champs magnétiques intenses

by

Amirreza Ataei

Mémoire présenté au département de physique

en vue de l'obtention du grade de maître ès sciences (M.Sc.)

FACULTÉ des SCIENCES

UNIVERSITÉ de SHERBROOKE

Sherbrooke, Québec, Canada, 10 April 2019

Le 10 avril 2019

le jury a accepté le mémoire de Monsieur Amirreza Ataei dans sa version finale.

Membres du jury

Professeur Louis Taillefer
Directeur de recherche
Département de physique

Professeur Ion Garate
Membre interne
Département de physique

Professeur Jeffrey Quilliam
Président rapporteur
Département de physique

Abstract

The high-temperature superconductivity and the phases that emerge in its vicinity have been the subject of many research studies and heated debates. We studied a wide range of dopings in the LSCO family of cuprate superconductors, in particular, Nd-LSCO ($La_{1.6-x}$ $Nd_{0.4}Sr_xCuO_4$). We performed electric, thermoelectric and thermal transport experiments to study the charge and spin density wave, pseudogap and strange metal phases and their interplay. Many of these transport experiments were performed in an extreme condition; in high magnetic fields, at low temperatures, and under hydrostatic pressure.

As the charge density wave phase (CDW) appears, it reconstructs the Fermi surface and changes the balance between electron and hole carriers. By entering this phase, the Hall coefficient, R_H, and the Seebeck coefficient, S, starts to decrease by decreasing the temperature. By tracking the signatures of the CDW onset temperature in transport probes at different dopings, we found the end point of this phase (p_{CDW}) and realized that it is different from the pseudogap critical point (p*). We studied the effect of pressure on the CDW phase. We discovered that by increasing pressure, the temperature at which the Seebeck coefficient becomes negative, T_0, decreases, which indicates that the CDW phase becomes weaker. On the other hand, the superconducting transition temperature, T_c, increases since the superconducting phase becomes stronger. In contrary, the onset of the charge order phase, T_{CDW}, which is located right below the structural transition, increases by pressure. This increase has been seen both in the temperature dependence of the R_H, and S/T. This observation shows that one of the constraints for the appearance of the CDW phase is the structure and reveals the competition between the superconducting and CDW phases.

We studied the effect of pressure on the pseudogap phase by using the electric and thermoelectric probes. At p = 0.22 $<$ p* = 0.23, in the temperature dependence of the resistivity and Hall effect, we observed that the upturn corresponding to the pseudogap phase is suppressed by the application of pressure. It shows that the pseudogap critical point moves to lower dopings by increasing pressure. We also observed that the pseudogap onset, T*, does not move by increasing pressure at lower dopings. The effect of pressure on higher dopings above the pseudogap is to decrease the magnitude of the Hall coefficient towards negative values. The conclusion is that the pseudogap phase is sensitive to the topology of the Fermi surface and it cannot exists on an electron-like Fermi surface. We realized that one

of the conditions for the presence of the pseudogap is p* $\leq$ p_{FS}, where p_{FS} is the doping at which the Fermi surface becomes electron-like.

For the first time, we performed the thermoelectricity experiments on cuprate superconductors in high magnetic fields and under pressure. We found that the S/T upturn at p = 0.22 is suppressed by the application of pressure. This result has corroborated the previous one and showed again that p* moves to lower dopings by the application of pressure.

We studied the magnetic field dependence of the resistivity isotherms at dopings above the pseudogap phase in Nd-LSCO (at $p = 0.24 > p^* = 0.23$) and in LSCO (at $p = 0.24 > p^* = 0.18$) up to 84T. We observed that the field dependence of the resistivity is linear at low temperatures and becomes quadratic at higher temperatures.

Résumé

La supraconductivité à haute température est accompagnée par différentes phases ayant été l'objet de nombreuses recherches et débats animés. Pour mieux comprendre ces différentes phases et leur interaction, nous avons étudié une vaste gamme de dopages dans la famille des supraconducteurs cuprates de LSCO, en particulier le Nd-LSCO ($La_{1.6-x}Nd_{0.4}Sr_xCuO_4$). Nous avons effectué des expériences de transport électrique, thermoélectrique et thermique pour étudier les ondes de densité de charge et de spin, le pseudogap et la phase dite de métal étrange. Beaucoup de ces expériences de transport ont été effectuées dans des conditions extrêmes; dans des champs magnétiques élevés, à basses températures et sous de grandes pressions hydrostatiques.

La phase d'onde de densité de charge (ODC ou CDW en anglais) reconstruit la surface de Fermi et modifie l'équilibre entre les porteurs de type électron et de type trou. En entrant dans cette phase, la dépendance en température du coefficient de Hall, R_H, et du coefficient de Seebeck, S, montrent une chute. En traçant les signatures de la température de début CDW dans les sondes de transport à différents dopages, nous avons trouvé le point final de cette phase (p_{CDW}) et constaté qu'il est différent du point critique du pseudogap (p^*). Nous avons également étudié l'effet de la pression sur la phase CDW. Nous avons découvert qu'en augmentant la pression, la température à laquelle le coefficient de Seebeck devient négatif, T_0, diminue, ce qui indique que la phase CDW devient plus faible. En revanche, la température de transition supraconductrice, T_c, augmente car la phase supraconductrice devient plus forte. Au contraire, le début de la phase de CDW, T_{CDW}, qui se situe juste en dessous de la transition structurale, augmente sous la pression. Cette augmentation a été constatée à la fois dans la dépendance en température de R_H et S/T. Cette observation montre que l'une des contraintes pour l'apparition de la phase CDW est la structure cristalline et révèle la compétition entre les phases supraconductrice et CDW.

Nous avons étudié l'effet de la pression sur la phase pseudogap en utilisant les sondes électriques et thermoélectriques. À $p = 0.22 < p^* = 0.23$, dans la dépendance de la résistivité et de l'effet Hall en fonction de la température, nous avons observé qu'une augmentation correspond à la phase de pseudogap supprimée par l'application de la pression. Cela montre que le point critique du pseudogap réduit en dopage en augmentant la pression. Nous avons également observé que T^* n'est pas affecté par la pression aux faibles dopages.

L'effet de la pression sur les dopages supérieurs au pseudogap est de diminuer l'amplitude du coefficient de Hall vers les valeurs négatives. La conclusion est que la phase de pseudogap est sensible à la topologie de la surface de Fermi et qu'elle ne peut pas exister sur une surface de Fermi de type électron. Nous nous sommes rendus compte que l'une des conditions pour la présence du pseudogap est $p^* \leq p_{FS}$, où p_{FS} est le dopage auquel la surface de Fermi devient de type électron.

Pour la première fois, nous avons effectué des expériences de thermoélectricité sur un supraconducteur de cuprate dans des champs magnétiques intense et sous pression. Nous avons trouvé que la hausse de S/T à $p = 0.22$ était supprimée par l'application de pression. Ce résultat corrobore le précédent et montre à nouveau que p^* passe à des dopages inférieurs par application de pression.

Nous avons étudié la dépendance au champ magnétique de la résistivité aux dopages supérieurs à la phase de pseudogap dans Nd-LSCO (à $p = 0.24 > p^* = 0.23$) et dans le LSCO (à $p = 0.24 > p^* = 0.18$) jusqu'à 84 T pour étudier la dépendance en champ de la résistivité dans la partie métal étrange du diagramme de phase. Nous avons observé que la dépendance en champ de la résistivité est linéaire aux basses températures et devient quadratique aux températures plus élevées.

Acknowledgments

Doing research on the subject that I was fascinated with for more than a decade in my life, was not possible without the support of my wonderful supervisor, Louis Taillefer. It did not take more than a week after I arrived in his group to feel that this is the very place for doing outstanding research on superconductivity, which I dreamed of since I began my high school! From the beginning, I was astonished by his intuition and depth of knowledge on various superconductors as well as physical concepts. Louis showed me how a top-notch world-class scientist looks like! I'm thrilled that I had the opportunity to be part of his team. I'd like to appreciate his kindness and generosity both for all of his support and sharing various discussions, ideas and thoughtful comments.

My projects in the group mainly concentrated on different experiments under pressure. In that regard, I'm honored to have collaborations with Adrien Gourgout and Nicolas Doiron-Leyraud. I started to do the first experiments under pressure with Nicolas, then Adrien joined the group, and we continued the electrical transport experiments under pressure and started to develop thermoelectricity measurements under pressure as well.

The good unique personal characters that I found in both Adrien and Nicolas is that they take a long-term view on students, rather than having focused on solving the problem themselves as it appears, this attitude helps a team to build up during the time. Nicolas, taught me every experimental procedures for doing high pressure experiments and even before I arrived, he generously sent me some of his unpublished papers to familiarize me with the kind of research that was ongoing in the group at the time. I got interested in the pressure experiments, and I chose a pressure based project after I arrived. I spent most of my time in the lab with Adrien, and he has the same attitude, instead of solving a problem himself right away and move the project fast, he let me figure out what is not right and assisted me to fix it. He took as much time as it was required to explain why we prefer a specific configuration over the other and we had lots of conceptual discussions on physics as well, he is smart and hard-working. The fact that he is very kind and patient, allowed me to ask lots of questions and figure out the minuscule details, and more importantly, it allowed me to build up my autonomy and run the complicated experiments alone.

Francis Laliberté was the second member of the group that I was in contact with before

I arrived. He helped me to find an apartment and did many other favors for me. We had the same office, and I kept disturbing him by asking many questions. But he always responded patiently; I can't remember a single time that I wanted to talk to him, and he did not reply immediately, even though he was at the middle of something! He has taught me how to do ultra-low-temperature measurements.

I discussed the possibility of doing new experiments with Sven, he always welcomed new ideas. I changed my programing language because of him, and he helped me with coding until his very end of presence in the group. The fact that he is curious and experimentally talented inspired me, and with his cooperation, we explored the unexplored realms of our lab and used many different unused facilities in our free time. Gaël Grissonnanche as an activist physicist, showed me how to be a better physicist and a more caring person. He helped me further with coding and we had many fascinating discussions. He and Simon Verret, showed me how accessible it is to do theoretical calculations for an experimental physicist (and what are the true limitations). Even though Simon was not in our group (he is a theoretician), we often discussed many theoretical concepts together.

Arezoo Afshar was the first member of Louis group that I talked to. She helped me to settle at Sherbrooke. Speaking my mother tongue far away from my home and in our lab, was heartwarming. I would like to thank Bastien Michon, for lots of the good moments and scientific discussions that we had in different parts of the world.

For doing all the different developments in our lab, we had to see Simon Fortier, our laboratory technician, to ask him to design new parts for an experiment. He is always open and had most helpful ideas. Il est toujours souriant et sympathique and he improved my self-confidence to talk in French considerably!

I would like to thank Marie-Eve Boulanger, Maude Lizaire, Clément Girod, Patrick Bourgeois-Hope, Clément Collignon, Anaëlle Legros, Étienne Lefrançois for their amiability, friendliness and the good times that we passed together in Sherbrooke, conferences and high field experiments.

Adrien, Francis and Gaël also helped me to improve the quality of this thesis.

I would also like to thank the experts who were involved in the validation survey for this Master dissertation, Prof. Jeffrey Quilliam, who has participated in different meetings for discussing the progress of my projects and provided valuable detailed suggestions on my thesis. I would like to thank Prof. Ion Garate for his helpful comments on my dissertation too.

Undoubtedly without the support of my parents, I have not come this far. I appreciate their invaluable devotion, love, and support. I recognize their position in my life after being away from them for more than two years. I want to thank my uncle Mohammadreza who has ignited my curiosity for many different physical phenomena including superconductivity.

Ultimately, I must express my gratitude to my wife, Reihaneh Forouhandehpour, for all her love, continual support, and endless encouragement. This accomplishment would not have been possible without her. She showed me how to be upbeat, my true self and love unconditionally.

Contents

List of Figures

Chapter 1

Literature review on transport properties and the effect of pressure in cuprates

Superconductivity is one of the most cutting-edge and influential fields of physics. Research on superconductivity provided insights in many other fields of physics. It was provided the first conjecture of a self-interacting boson field [1] that was later used in the Higgs mechanism and the theoretical development of many body systems. It is also an accessible example of collective phenomena and holographic duality [2]. In physics, we are mostly dealing with approximations and imperfect phenomena, but superconductors have been proven to be perfect conductors with absolute zero resistance [1].

Superconductivity is an emergent phenomenon which appears when the mobile electrons of material form a collective and coherent state. The electronic correlations inside the superconductors become stronger by increasing the lattice complexity (which happens by increasing the number of distinct constituents of a superconductor material).

Superconductors already have many applications in industry and scientific research, for instance as a superconductor material can pass a significant current density when it is in the form of a wire. It can also produce a large magnetic field which is in high demand for particle accelerators like CERN or Magnetic Resonance Imaging (MRI). However, it is foreseen that the significant direct impacts of superconductivity to human civilization are yet to come! The discovery of room temperature superconductors or the economic and efficient means of cooling could have a comparable impact to the discovery of transistors and even conductors themselves. This breakthrough could have possible applications ranging from the electronics industry to transportation and space exploration.

[1] A group of researchers measured zero resistivity in the superconducting state for two and half years [3].

In this chapter, we discuss basic concepts that are being used to explain the mechanisms of superconductivity and related phases close to the superconducting state.

There are two types of superconductors. Type I consists of about 20 elements where the magnetic field remains zero inside it until superconductivity is suppressed by critical field H_c and type II are compounds of two or more elements [2]. In the latter type, the magnetic field can partially penetrate inside the superconductor in fields higher than the lower critical field H_{c1} but the superconductivity gets suppressed only above the upper critical field H_{c2} and, in between, a vortex state exists in the material while it is in the superconducting state. Throughout this thesis, only type II superconductors are discussed. Among the type II superconductors, there are two categories: conventional and unconventional ones. The former type is a kind of superconductor which could be explained by the BCS theory with electron-photon pairing [4] and its maximum T_c is typically less than 30 K [3] [6]. The latter type is the one which cannot be explained by that theory.

A superconductor should have two distinct characteristics. First, its resistivity should go to zero at certain temperatures— T_c— and remains zero $T < T_c$. Second, it should be a perfect diamagnet that is shown by $M = -H$ where H is the applied magnetic field and M is the magnetization of a superconductor in the presence of H.

The normal state of a type II superconductor can be reached above the upper critical field H_{c2}. We are interested in studying the normal state, and our approach is to apply a sufficiently high magnetic field to suppress the superconductivity. For the material that we mostly study here, $La_{1.6-x}Nd_{0.4}Sr_xCuO_4$, we can reach the normal state down to the low temperature at all dopings by applying 30T or less.

1.1 Cuprate superconductors

Cuprate superconductors (we also refer to it as cuprates) are layered materials consist of CuO_2 superconducting planes with stacks of other atoms. According to scholarly indexing websites, cuprates are the branch of condensed matter physics that are most cited after semiconductors and this field is still popular as there are different phases near superconductivity that have yet to be explained. It is ironic that the best-understood phase in cuprate superconductors is the superconductivity itself! The hottest debates are evolving around the other phases such as pseudogap, spin and charge density wave, strange metal and their interplay.

[2] Except Niobium, Vanadium and Technetium.

[3] Although in 2015, H_3 —a BCS superconductor— became superconductor under pressure with T_c = 203 K [5].

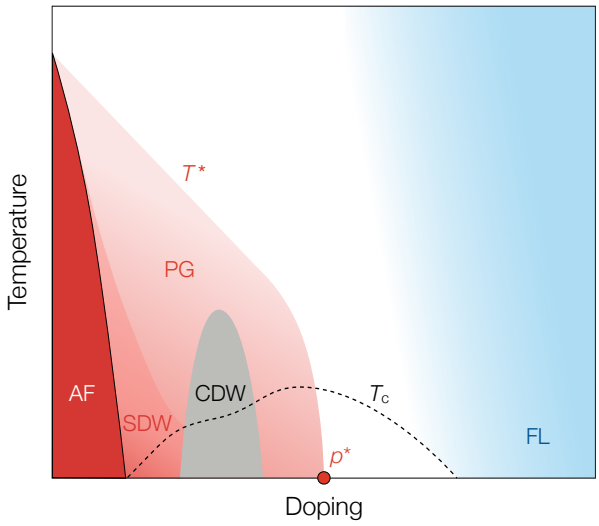

Figure 1.1 Sketch of the general phase diagram of cuprate superconductors. This diagram presents temperature and doping dependence of different phases of cuprates. Starting from the left side of the phase diagram, at p = 0 the material is a Mott insulator. By going to the right side, the percentage of doping is increasing. The dark red region is an Antiferromagnetic phase (AF). The boundary of the AF phase denoted by a black line represents Néel transition temperature. Spin density wave (SDW) is shown by medium red colour and charge density wave phase is coloured gray. The pseudogap phase is shown by the light red colour and its boundary with the strange metal region (white regions) is called the pseudogap temperature onset (T*) and it ends at critical doping (p*). The superconductivity dome is denoted by dashed black line. Fermi liquid phase is denoted by the light blue shades. Courtesy of Francis Laliberté.

1.1.1 Phase diagram and evolution of Fermi surface with doping

Fig 1.1 shows a general sketch of the phase diagram of the cuprates (for the interest of generalizing this sketch for all the cuprates, the y and x-axes have arbitrary units and scales). The undoped material is a Mott insulator [7] where electrons are well-localized because of a strong on-site repulsion. As one dopes the material with holes and removes some electrons from the CuO_2 planes, the electrons become less restrained to move (as the Coulomb repulsion is reduced). However, at low dopings and low temperatures the material still remains an insulator, but by increasing the doping it losses its insulating properties eventually (usually above the hole content of p = 0.08).

Fig 1.1 shows the antiferromagnetic phase (AF) with the boundary of the Néel transition temperature. After that, there is another phase in which a magnetic order has been seen, this phase is known as spin density wave (SDW). The endpoint (p_{SDW}) is material-dependent.

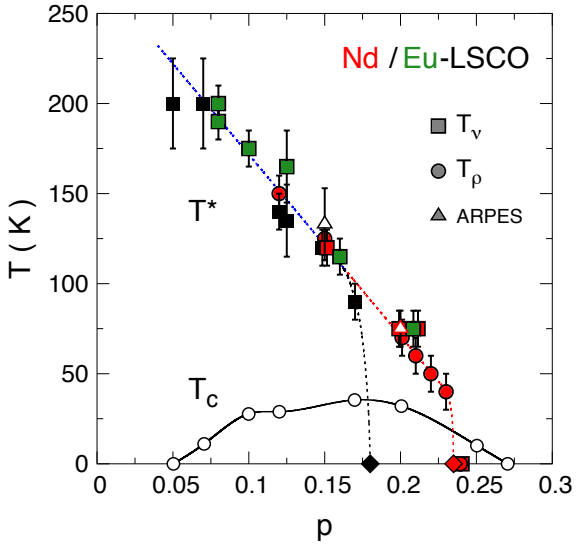

Figure 1.2 Phase diagram of Nd-LSCO (red), Eu-LSCO (green) and LSCO (black). T_ρ (circles) and T_ν (squares) are showing pseudogap onset T* probed by resistivity and Nernst effect respectively [8]. ARPES measurement that observed opening of pseudogap is denoted by squares[9].

For example $p_{SDW} = 0.08$ in YBCO [10] and $p_{SDW} = 0.13$ in LSCO.[11]. This phase is believed to compete with the superconductivity phase [12].

Another short-range order like SDW is charge density wave (CDW) which is denoted by grey in Fig 1.1. There are various studies concerning the symmetry and commensurability of CDW, SDW and the mixture of the two in the cuprates [13, 14, 15]. It was believed that CDW is always observable at higher temperatures compared to SDW order (which is generally true at $p = 0.12$, but not at other dopings). Thus, CDW is a prerequisite to SDW in a stripe phase and the stripe-order transition should be charge driven [16, 17].

All of these phases with short-range order are located inside a much bigger phase: the pseudogap phase. The pseudogap phase and its origin are the most mysterious part of the cuprates so far! It is stronger in the lower dopings and for some cuprates, it abruptly disappears at the doping level referred to as p* (shown in Fig 1.1 with a red circle). T* is the boundary between this phase and the strange metal phase (white shaded region). T* is thought to be a crossover which makes it hard to pin down (as opposed to a phase transition which is easier to observe). The superconducting dome ends at the heavily overdoped region above which there is a Fermi liquid phase that is denoted by blue colour. We call the dopings above the optimal doping—where T_c is highest— overdoped and the dopings below that as underdoped.

In the interest of brevity, we focus primarily on the CDW and pseudogap phases although the Fermi surface of all of the mentioned phases is discussed briefly. Here we study the $La_{2-x}Sr_xCuO_4$ (LSCO) family of superconductors and almost all the focus is

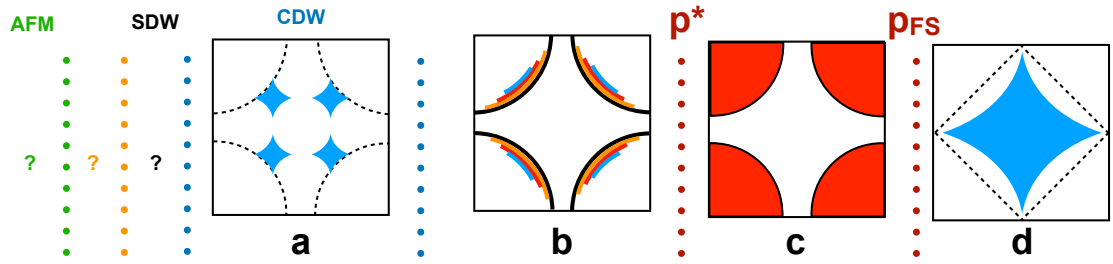

Figure 1.3 Sketch of the Fermi surface in different phases of cuprates. From left to right the doping is increasing. a) Electron pockets of the reconstructed Fermi surface by CDW. b) Fermi arcs that are gapped out by the pseudogap. When pseudogap is bigger and stronger, the Fermi arcs are smaller, and they are located on the antinodal region. c) Big hole-like Fermi surface above the pseudogap critical point p*. d) Above p_{FS} the Fermi surface goes through the Lifshitz transition and becomes electron-like. SDW phase is located below and even inside the CDW. There is a small region between SDW and AFM where there is only superconductivity and pseudogap.

on $La_{1.6-x}Nd_{0.4}Sr_xCuO_4$, labelled as Nd-LSCO hereafter, although $La_{1.8-x}Eu_{0.2}Sr_xCuO_4$ (Eu-LSCO) is in this family and sometimes recalled for comparison. In Nd-LSCO, the doping content is changed by varying the strontium content (x).

Figure 1.2 shows the phase diagram of LSCO family superconductors: T* was determined either by resistivity or via Nernst effect as discussed below and both of these results are in agreement with the ARPES measurements (all the data are obtained from [8] and the references therein).

Fig 1.3 shows the evolution of the Fermi surface in the hole-doped cuprates. Starting from overdoped part of the phase diagram, the Fermi surface consists of a large hole-like cylinder Fig 1.3-c, as seen in Tl-2201 [18]. This hole-like cylinder continues to grow up until the Fermi surface goes through the Lifshitz transition at p_{FS}. It happens at the hot spots where the two large hole-like cylinders touch one another and the Fermi surface becomes electron-like [19] (fig 1.3-d). This electron-like Fermi surface is located inside the antiferromagnetic zone boundaries (dashed line in Fig 1.3-d). Below p*, due to the presence of the pseudogap, some parts of the Fermi surface are gapped out leaving Fermi arcs as shown in Fig 1.3-b. The size of the Fermi arcs depends on the strength of the pseudogap; when the pseudogap is stronger, it can gap out a larger portion of the Fermi surface resulting in smaller Fermi arcs. The pseudogap is more dominant on the Fermi surface at lower dopings and temperatures as seen by STM [20].

Fig 1.3-a shows the reconstructed Fermi surface which is the result of the transformation of these Fermi arcs into the electron pockets by CDW order. These nodal electron pockets are detected by quantum oscillations [21, 22] in YBCO.

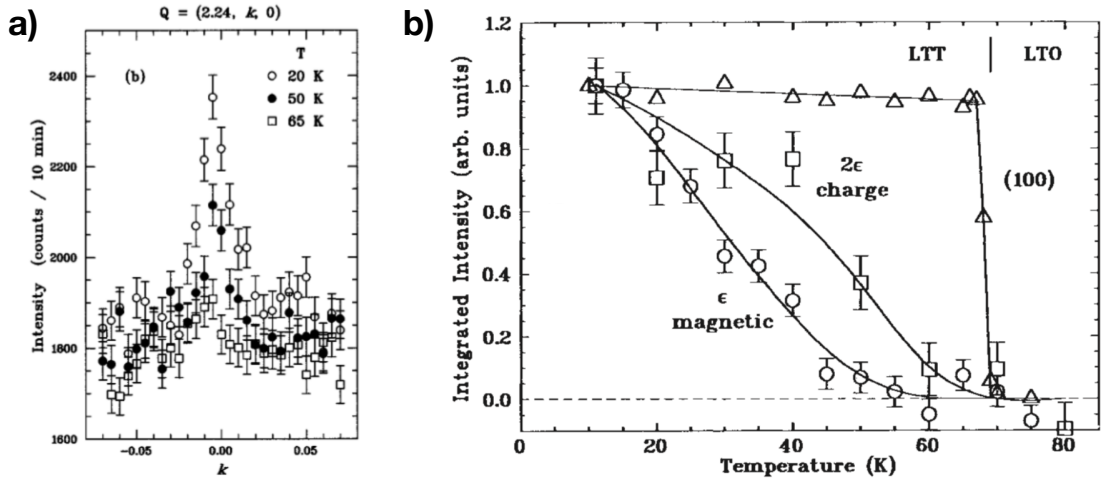

Figure 1.4 a)Transverse neutron scattering scans through Q = (2+2ϵ,0,0) in Nd-LSCO $p = 0.12$ which corresponds to the CDW peak for temperatures as indicated. The data are obtained from Ref [23]. b) Temperature dependence of lattice peak intensities for Nd-LSCO $p = 0.12$ normalized at T = 11K. Circles are the peak intensity that have magnetic origin, squares have CDW origin and triangles are showing the structural transition from LTT to LTO. The data are obtained from Ref [13].

1.1.2 Charge order

A redistribution of electron density in the copper-oxide planes causes the appearance of a periodic charge structure called charge order, which is also known as charge density wave (CDW).

CDW was observed in Nd-LSCO by neutron scattering [13, 23] and also in other cuprates such as YBCO with resonant x-ray scattering [25], resonant soft x-ray scattering [26], x-ray diffraction [27] and with the NMR technique [28] and [29].

Fig 1.4-a shows the peak intensity obtained by neutron scattering [23] through Q = (2+2ϵ,0,0), where $\epsilon \approx$ p ≈ 0.118, which corresponds to the presence of charge density wave in Nd-LSCO at $p = 0.12$. The intensity of this peak increases as temperature decreases showing that the strength of CDW rises.

Fig 1.4-b shows the temperature dependence of integrated peak intensities of the superlattice. The abrupt drop is due to the structural transition from low-temperature tetragonal (LTT) at lower temperatures to low-temperature orthorhombic (LTO) at higher temperatures. The peak that is associated with LTT is not observable when the structure is LTO. The other two peaks corresponding to magnetic and charge order. The peak at Q = (0,2-2ϵ,0) is associated with charge density wave order and at Q = (1/2,1/2$-\epsilon$,0) is related to a magnetic order (also known as spin density wave), and when the charge and magnetic order phase

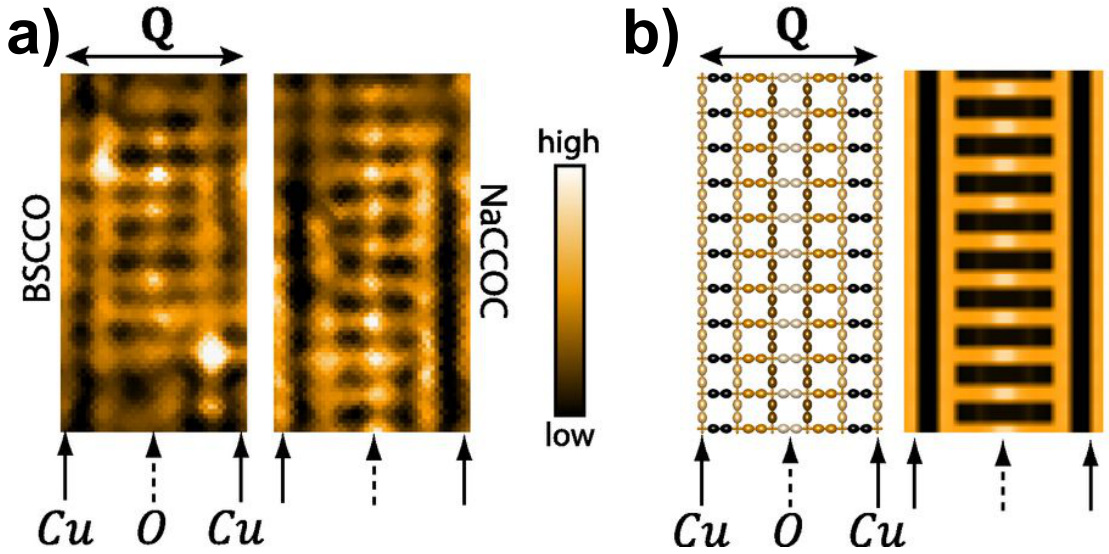

Figure 1.5 a- Real space mapping of charge order intensity in copper-oxide plane of Bi-2212 and NaCCOC along Cu and O_x direction that is denoted by solid and dashed arrows respectively. b- Left: Cartoon of the charge intensity map in the copper-oxide plane with the maximum intensity located at O_x and Q = (0.25,0). The Figures are obtained from the Ref [24].

coexist, they called stipe order. The magnetic order in Nd-LSCO is similar to the CDW phase as the periodicity of their modulations is commensurate and they lock inside each other. The spin density wave is related to a change in the distribution of spins and the creation of periodic modulated magnetic structures. Fig 1.4-b also shows that the onset of CDW and SDW are different and their intensities increase at lower temperatures.

In the cuprates and in more complicated cases, the CDW modulations could be biaxial or unidirectional which are the consequence of different wave vectors that reconstruct the Fermi surface and it is material dependent [30, 31]. CDW modulations have been detected directly by Scanning Tunneling Microscopy (STM) measurements, thereby showing charge order in some other cuprates; notably the Bi_2 Sr_2 Ca Cu_2 O_{8+x} Bi-2212 and $Ca_{2-x}Na_xCuO_2Cl_2$ (NaCCOC) systems, as shown in Fig 1.5. Fig 1.5-a shows the real space map of charge modulations on Cu and O_x sites denoted by solid and dashed arrows respectively. Fig 1.5-b shows a cartoon of the d-form factor density wave and shows that their periodicity is 4 lattice constants. In another words Q = (0.25,0). On the right side of this cartoon the calculated CDW scheme is shown from this d-form factor density wave model.

It is essential to study the CDW phase as it appears to have competition with the superconducting phase. In particular, its presence causes a dip in the superconducting dome [32]. Another signature of CDW is the presence of a dip in H_{c2} vs p [33] measured by thermal conductivity. Furthermore, some theories suggest the pseudogap and CDW have the same critical point and they end at the same doping of p* [34, 16, 35].

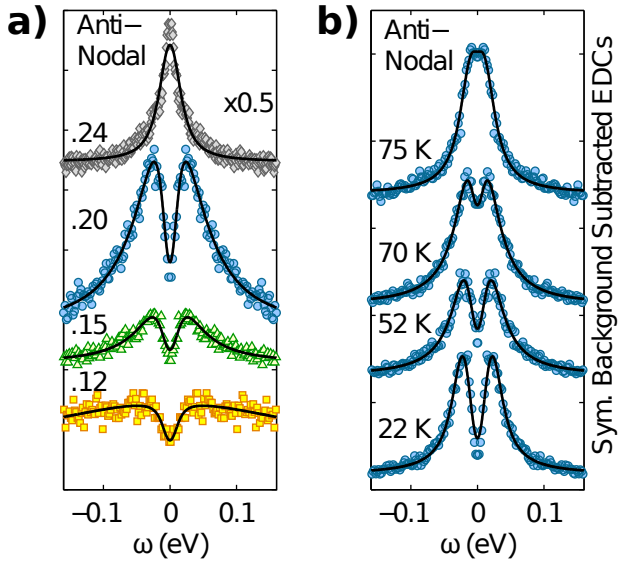

Figure 1.6 a) Energy distribution curves of Nd-LSCO in different dopings at temperatures right above the T_c. The curve at $p = 0.24$ (gray) is above the pseudogap and the rest of the curves are in the pseudogap at p < p*. b) Energy distribution curve for Nd-LSCO p = 0.20 at different temperatures. All the curves are arbitrary shifted vertically for clarity and symmetrized. The Figure is obtained from Ref[9].

Around $p = 0.125$, there is a dip in the superconducting dome as shown in Fig 1.2. As the charge order phase is located around this doping range, it is thought that it competes with superconductivity and is responsible for lowering T_c. One way to investigate that, is to suppress this order by the application of pressure. This has been done in YBCO and by suppressing the CDW via pressure [32, 36], the dip in the T_c dome was removed and the full shape of the dome was recovered, meaning that there is indeed a competition between CDW and superconductivity in this system. We verified the possibility of CDW suppression by pressure in Nd-LSCO and we discuss it further in chapter three.

1.1.3 Pseudogap phase

The pseudogap was discovered via the NMR technique in less than three years after the discovery of superconductivity in the cuprates [37, 38]. It is currently the central puzzle of the cuprate superconductors, and different theoretical and experimental groups are trying to delineate the relationship between the pseudogap and other phases with different approaches (e.g. by suppression of the density of states).

The onset of the pseudogap in temperature is represented by T* and the endpoint of the pseudogap in doping is known as p* (the doping at which T* goes to zero), both of which

have signatures in transport probes as well as spectroscopic measurements. We discuss its transport signatures later on in this chapter. By using angle-resolved photoemission electron spectroscopy, ARPES, one can find spectroscopic evidence of this phase [39, 40, 41, 42].

Fig 1.6-a, shows symmetrized energy-distribution curves for several dopings of Nd-LSCO at temperatures just above T_c. A gap (manifested by a drop in the spectral weight at ω = 0 eV) in the anti-nodal region appears at dopings 0.12, 0.15 and 0.20, but at $p = 0.24$ it disappears. The presence of this gap means that the density of states decreases and is associated with the pseudogap. Hence, one can conclude that the pseudogap closes between p = 0.20 and 0.24 [9]. In Nd-LSCO, by tracking the signatures of resistivity and Hall effect, the pseudogap endpoint was pinned at p* = 0.23 $\pm$ 0.01 [43].

The pseudogap phase also has a signature in temperature. Fig 1.6-b, shows the spectral weight in the anti-nodal direction for Nd-LSCO at p = 0.20 $<$ p*. At 75K there is no gap in the spectrum. By decreasing the temperature, a gap opens up and becomes bigger down to 22K (which is still above T_c).

In Fig 1.2, if one extrapolates the T* line up to the overdoped region, it ends at the end of the superconductivity dome which suggests that the same interactions might be responsible for the pseudogap and superconductivity (nevertheless, the pseudogap suddenly disappears at p*). The left side of the T* line at the zero doping intercepts the onset of the Néel temperature (fig 1.1) which provides support for the antiferromagnetic origin of the pseudogap. Spin modulations (spin density wave or SDW) have been detected right after the AFM phase(Fig 1.1), hence their origin might be the same as the AFM phase, even though the SDW modulations are short-range. The endpoint of the SDW phase is thought to be located at p* [11] (experimental evidence is required here, but the fact that SDW phase is still present after the endpoint of the CDW phase and before p*, as in Nd-LSCO, supports this hypothesis) which again promotes the AFM origin of the pseudogap phase.

Later on in this chapter, we focus on the signatures of the pseudogap in the transport experiments and discuss some of these theories but the pseudogap is a highly debated phase and it is not evident if it is a friend or foe or a friendly foe of the superconductivity and the other phases in cuprates [34].

1.1.4 Fermi Liquid and strange metals

In Fermi-Dirac statistics, conduction electrons in a metal are treated as non-interacting fermions in a Fermi gas and the system is called Fermi liquid. Based on the Pauli exclusion principle, electrons at the Fermi surface are only allowed to have a sort of collision that can change their momentum with the assumption of a one-one condition (there is no interaction between many electrons simultaneously). In the low temperature limit where the one-one condition holds, the interactions are renormalized the parameters like the effective mass

(m^*) which gives the T^2 resistivity and the specific heat becomes linear in temperature as the resistiv

In the marginal Fermi liquid theory [44] this assumption has been modified so that it can explain other transport signatures that could not be explained with Fermi liquid theory. Some theories suggest that the superconductivity in cuprates is born from the over-doped side of the phase diagram where the Fermi liquid regime starts to break [7]. Between the Fermi liquid phase and the pseudogap in high-temperature superconductors, there is a phase called strange metal that is the consequence of this "alteration" or "break down" of Fermi liquid regime. In this system, one should consider the collective interaction of electrons together (instead of just taking the one-one condition into account) in order to explain the deviation from the T^2 resistivity of the Fermi liquid regime.

In a temperature range above T* for $p = 0 < p < p^*$ and at $T \rightarrow 0$ for $p^* < p_c$ [4], the normal state resistivity in the cuprates has a linear temperature dependence, which can not be explained by the conventional theory of metals. It has been shown recently, both in the hole and electron-doped cuprates, that regardless of the governing inelastic scattering mechanisms, whenever the scattering rate ($1/\tau$) reached its Planckian limit $1 / \tau = k_B T / \hbar$ the resistivity becomes T-linear [45]. It is why this region in the phase diagram is called "Strange Metal".

The temperature dependence of the resistivity at $p > p_c$ has the form of T^{α} where $1 < \alpha < 2$ [46]. On top of that, the AC conductivity has a frequency dependence [47] which is also incompatible with the conventional theory of metals. Besides, through the suppression of superconductivity at the dopings in the vicinity of p*, the residual resistivity has a linear field dependance [48] which has not yet been explained.

To study this phase of cuprates, we looked at the temperature and field dependence of resistivity that is discussed in the last part of chapter 3.

1.2 Electrical transport properties

1.2.1 Resistivity

Resistivity is a measure of scattering of electrons in the lattice. At T = 0, the dominant mechanism for scattering is due to all possible kinds of impurities and imperfections in the crystal such as vacancies, interstitials, and dislocations. At T > 0 K, other scattering mechanisms (such as electron-phonon inelastic scattering) come into play. We use the Drude

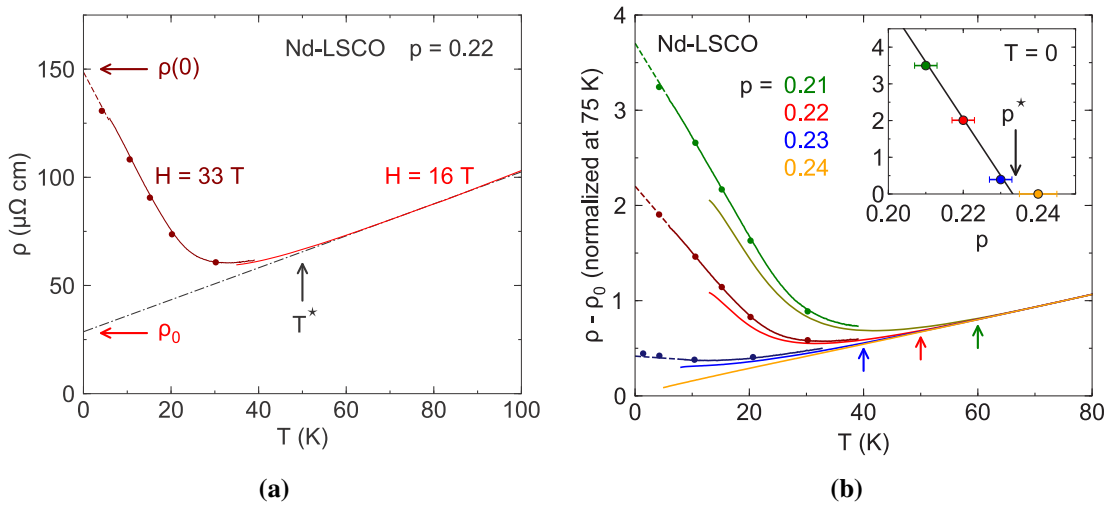

Figure 1.7 a) Temperature dependence of resistivity at p = 0.22 < p* = 0.23 in Nd-LSCO. Dashed black line shows linear fit of resistivity in either zero magnetic fields or H = 16T and the point that resistivity deviates from linear fit is shown with arrow [43] b) Temperature dependence of resistivity at different dopings, different colours showing different doping and same colour code used for arrows to show T* [43]. All Figures present the in-plane resistivity.

formula to interpret resistivity $\rho = m/ne^2\tau$, where τ is the scattering rate, m and e are the mass and electric charge of electron respectively and n is the density of electrons.

More than two decades ago it was discovered that the temperature dependence of resistivity deviates from linearity [49]. The point below which resistivity is not linear and it shows either a downturn in YBCO [49] or an upturn in Nd-LSCO [49] is known as the onset of the pseudogap—T*. Here we only focus on the upturn of pseudogap for Nd-LSCO. Resistivity depends on the number of carriers and scattering (elastic and inelastic). When the pseudogap appears, the density of states, the carrier density and the inelastic scattering all decrease (and the decrease in the magnitude of one may or may not be the consequence of a decrease in another). In a clean system such as YBCO, when the pseudogap opens, as the dominant source of scattering is the elastic scattering, the inelastic scattering decreases which results in a decrease in resistivity. But in a dirty system like Nd-LSCO, when the pseudogap, the inelastic scattering does not change that much as it is dominant, so, as there are fewer carriers in the system, the resistivity rises.

In Fig 1.7-b T* is shown for different dopings of Nd-LSCO by different arrows. At the dopings above the pseudogap p* < p, there is no T* and the resistivity presents no upturn related to the pseudogap as shown in Nd-LSCO at $p = 0.24$ in Fig 1.7-b, where ρ remains T-linear down to T→0.

[4] p_c is the highest doping at which superconducting dome ends in the overdoped region.

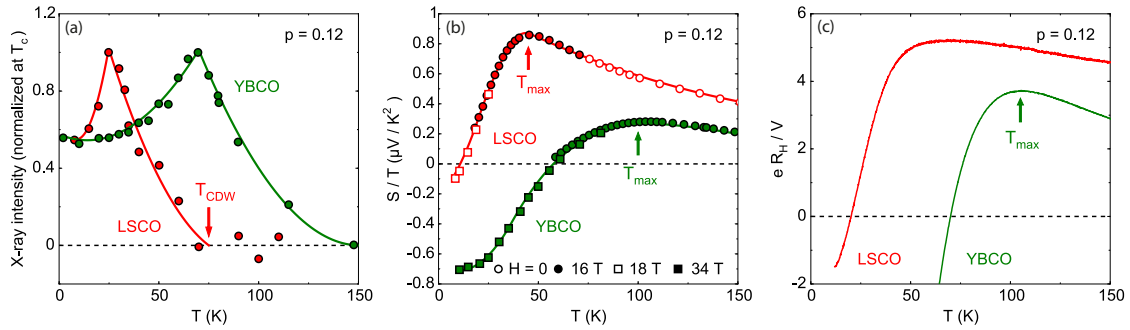

Figure 1.8 Comparison of LSCO (red) and YBCO (green) at $p = 0.12$ a)X-ray intensity as a function of temperature associated with the CDW modulations, normalized at T_c, detected in LSCO [50] and YBCO [27], the peak is at T_c. b) Temperature dependence of Seebeck coefficient over temperature measured in YBCO [51] and LSCO [52] in the presence of magnetic field (normal state) c)Hall effect of YBCO at 15T [53, 54] and of LSCO at 16T [52].

1.2.2 Hall Effect

In the simplest model of an isotropic Fermi surface, R_H is the Hall number that is calculated as $R_H \approx \pm 1/ne$, where n is the number of carriers per unit volume and e is the electron charge. The carriers determine the sign of R_H, if the majority of carriers are holes the sign of R_H is positive, otherwise it is negative. One can calculate the Hall number n_H

$$n_H = \frac{V}{R_H e} \tag{1.1}$$

where V is the unit cell volume.

The effect of CDW in LSCO and YBCO is a clear drop in Hall coefficient [52]. Fig 1.8-a shows the intensity of X-ray vs temperature for LSCO and YBCO. The temperature at which the intensity is increasing is related to the onset of CDW.

It should be mentioned that the superconductivity could cause a downturn as well, but the difference is that it must happen near T_c and it is much more abrupt compared to the downturn that signifies CDW. This makes observing CDW hard for transport probes, especially when T_{CDW} is located near or even below T_c. In this case, one needs to suppress superconductivity and consequently the downturn that corresponds to it; to be able to locate T_{CDW}. We do this through the application of high magnetic fields. [5] We argue that when we

[5] One must notice that the magnetic field is being used only to suppress the superconductivity. Also, it does not have any effect on the CDW. One must notice that the CDW phase is not field-induced or field dependent. As the drop in the Hall coefficient vs T does not change at different fields (at least for a considerable range of temperature) both above and below the T_c.

apply the magnetic field on dopings for which T_c is well-separated from T_{CDW}, the magnetic field cannot move T_{CDW} at all.

Positive and negative curvatures of the Fermi surface cause hole and electron-like Hall response as discussed in Ref [57] (the interpretation of the Fermi surface geometry on the Hall coefficient is obtained by using the conventional Boltzmann theory). However, when the Fermi surface has both a positive and negative curvatures the Hall response is the balance between the hole and electron-like contributions of the Fermi surface [58]. Thus, Hall effect can reveal any phase that reconstructs the Fermi surface and changes its geometry, but one should be aware of the complications behind the Hall signal (e.g., the presence of positive and negative curvatures both in a single Fermi surface and in a multi-band system). In cuprates superconductors at the CDW phase, the drop in R_H vs T marks the onset temperature at which Fermi surface starts to get reconstructed by CDW.

Pseudogap also has a signature in Hall effect. In Fig 1.9-a, temperature dependence of Hall effect is shown in Nd-LSCO for several dopings; at p < p*, there is an upturn as was the case for resistivity.

In Nd-LSCO, by obtaining the Hall coefficient at low temperature and in high magnetic fields and knowing that V/e in this material is 0.625 m^3/C (as in LSCO), one can calculate the normal state Hall number, n_H. Fig 1.10 shows the trace of Hall number for two completely different materials at different dopings. It is shown that there is a drop in carrier density from 1+p to p as the doping drops below the p*. Having 1+p carrier density means that the Fermi surface is hole-like (a large hole like Fermi surface has been seen in Tl-2201 [18] by ARPES). In an antiferromagnetic scenario, this large Fermi surface folds and makes nodal hole pockets and antinodal electron pockets in the drop between 1+p to p. However, the nature of Fermi surface reconstruction at p* is not yet known.

1.3 Thermoelectric transport properties

Thermoelectric coefficients are also sensitive to the band structure. In all of the thermoelectric measurements that are mentioned in this thesis, the magnetic field is applied along the c-axis, a longitudinal thermal gradient is applied within the CuO_2 planes and a Seebeck or Nernst voltage in the a-b plane has been measured. The schematic of our experimental setup is discussed in chapter two.

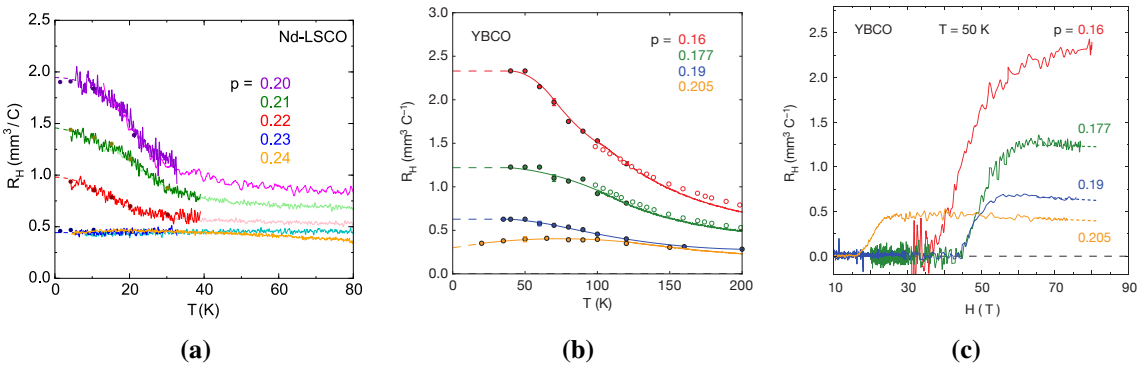

Figure 1.9 a) Temperature dependence of Hall coefficient at the dopings below and above p* in Nd-LSCO in low (light colour) and high magnetic field of 33T (dark colours) [43] b) Back extrapolation of Hall coefficient vs temperature in YBCO in high magnetic fields up to 80T, circles are field sweep cuts that are shown in plot (c) [52]. At p = 0.205 which is located above p*, there is no upturn that is the characteristic of pseudogap. c) Field dependence of Hall coefficient in YBCO. Compared to Nd-LSCO, YBCO requires higher magnetic fields for the suppression of superconductivity needed to reveal $R_H(0)$ [52].

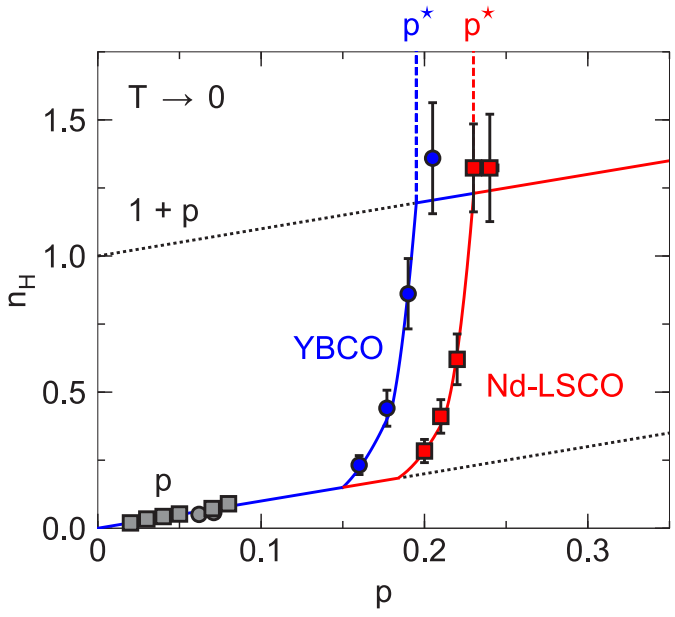

Figure 1.10 Doping dependence of Hall number n_H is shown for Nd-LSCO (red squares) and YBCO (blue circles). In low dopings the gray squares are Hall number in LSCO [55] and gray circles are for YBCO [56]. Solid lines are guide to the eye and p* at 0.195 $\pm$0.01 and 0.23$\pm$0.01 for YBCO and Nd-LSCO respectively. The Figure is obtained from the Ref [43].

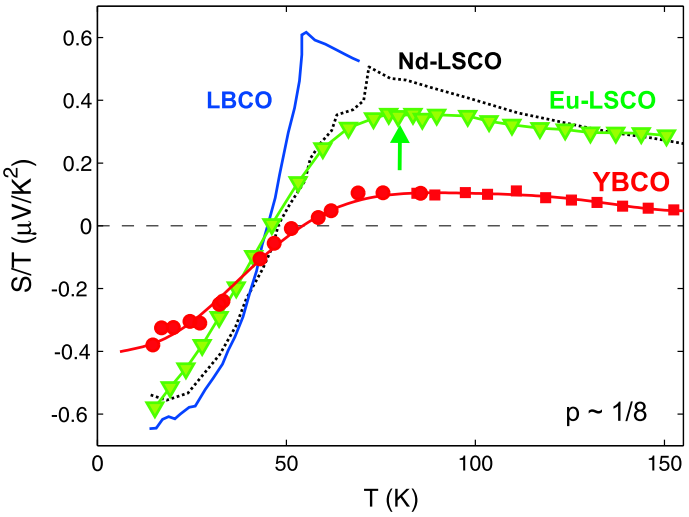

Figure 1.11 Seebeck coefficient over T as a function of temperature in different superconductors at $p = 0.12$ (1/8 anomaly) data and Figure obtained from Ref [59] and references therein.

1.3.1 Seebeck Effect

We obtain the Seebeck coefficient, S, via $S = \frac{V_S}{dT_x}$, where V_S is the longitudinal Seebeck voltage and dT_x is the longitudinal temperature difference (the detailed discussion on how we measure the Seebeck effect is mentioned in the second chapter). Like the Hall effect, the Seebeck coefficient can determine the sign of the majority of carriers. The balance between the electrons and holes that are moving in the thermal gradient can determine the sign of the carriers. The difference with the Hall effect is that in this case, it is not necessary to apply a magnetic field.

As shown in Fig 1.8-b, CDW has an effect on the Seebeck coefficient that is similar to its effect on the Hall coefficient (R_H). Fig 1.11 shows the Seebeck effect in different materials at $p = 0.12$ which is also known as the 1/8 anomaly.

In summary, charge density wave modulations cause a Fermi surface reconstruction [60] which has a clear signature in our transport probes.

1.3.2 Nernst Effect

In the presence of an applied magnetic field, a thermal gradient inside a conductor, that does not have any net electrical current flowing inside it, can produce a transverse voltage that is

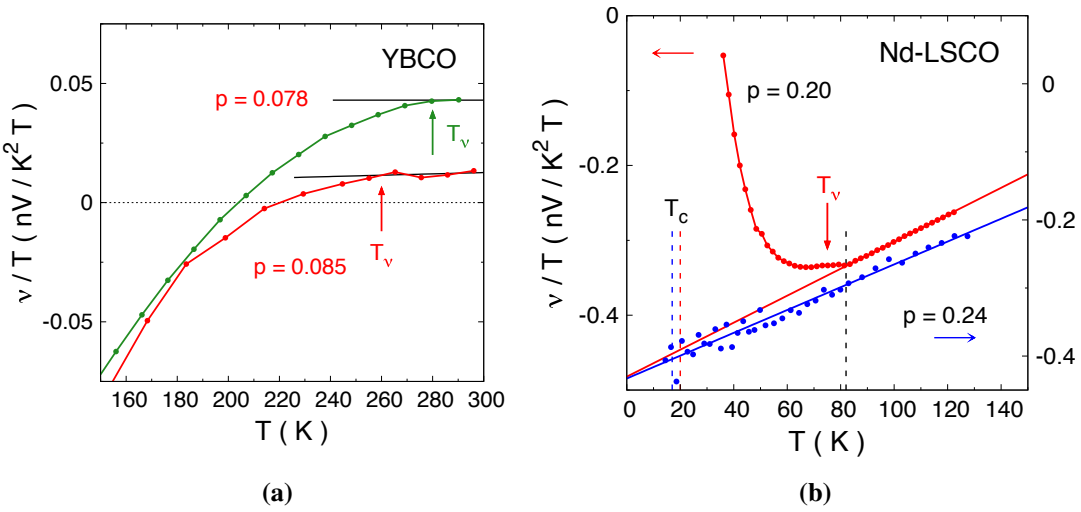

Figure 1.12 Temperature dependence of Nernst coefficient over temperature for a) highly underdoped YBCO at two dopings and b) in Nd-LSCO at p = 0.20 (red) and $p = 0.24$ which are below and above the pseudogap respectively. Tν marks the onset of pseudogap, T*. Figure obtained from Ref [8].

called the Nernst voltage, N, and is calculated as:

$$N = \frac{-E_y}{\nabla T_x} \tag{1.2}$$

The Nernst coefficient is ν = N/H where H is the magnetic field. In the T = 0 limit, it has approximately the following magnitude:

$$\nu = \frac{\pi^2}{3}\frac{k_B}{e}\frac{k_B T}{E_F}\mu \tag{1.3}$$

Where E_F is Fermi energy and μ is mobility, which means that the Nernst coefficient is determined by the Fermi energy and mobility. There are three physical phenomena that could contribute to this signal which are quasi-particles, superconducting fluctuations and superconducting vortices [61]. Again, we will suppress the latter two contributions by applying a large field. In two dimensions, the magnitude of the Nernst coefficient is inversely proportional to the carrier density, as in low carrier densities the Fermi energy is lower. Here we plot ν over T instead of ν.

To delineate the pseudogap more precisely, one can use the Nernst effect. Fig 1.12 shows the temperature dependence of the Nernst coefficient as a function of temperature for YBCO and Nd-LSCO. T_ν is the temperature at which ν/T deviates from linearity which coincides

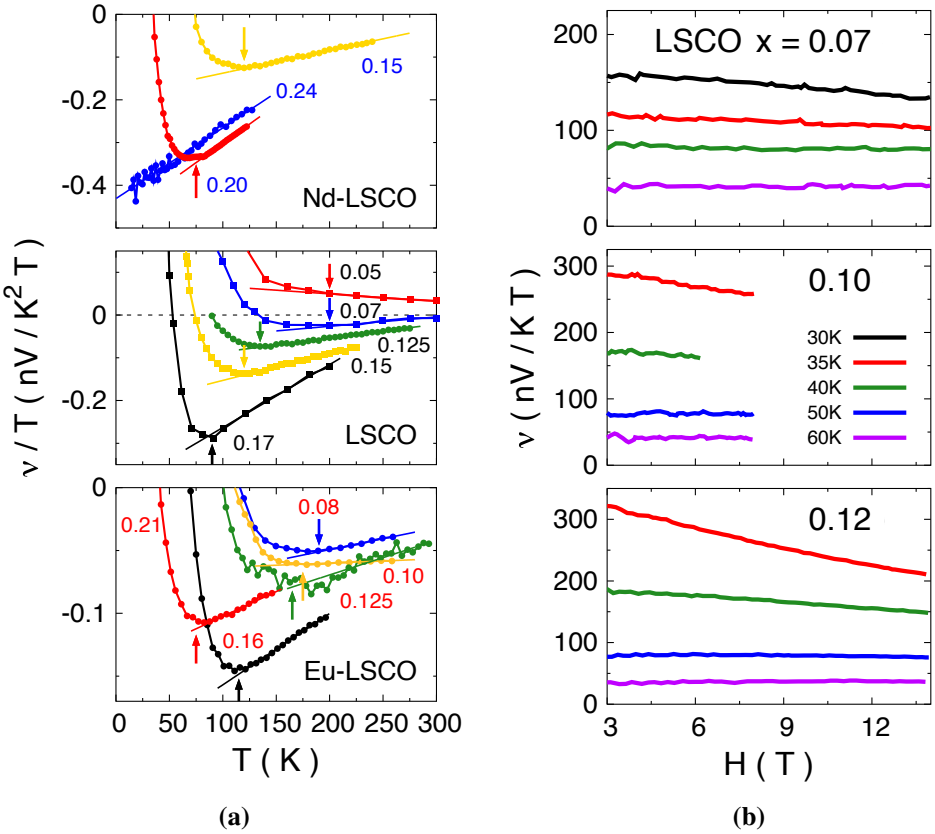

Figure 1.13 a) Temperature dependence of ν/T in LSCO family superconductors at different dopings. b) Magnetic field dependence of Nernst coefficient in LSCO at different dopings. Note that at high temperatures the Nernst coefficient becomes more field dependent. Obtained from [8]

with T* measured by resistivity and the pseudogap onset that is determined by ARPES, so T_ν = T* [8]. It is important to notice that it is much more straightforward to determine T* via the Nernst coefficient compared to the resistivity, as it is shown in Fig 1.13-a, the deviation from linearity below p* is much more pronounced in the Nernst coefficient as compared to the resistivity, regardless of the type of material. In Fig 1.13-b the field dependence of the Nernst signal in underdoped Nd-LSCO is shown.

1.4 Crystal structure and pressure effect

The effect of pressure on Hg-1223 [62] was to increase the T_c up to 164K and this increase of the T_c saturates above 16GPa, which inspired many advances in the superconducting research at that time [6]. In general, pressure squeezes the lattice in the real space, and that may tune the band structure too, by doing so, it can affect the transport properties of materials. Depending on the material and the magnitude of pressure, this effect might be dramatic or not. One of the motivations behind the study of the effect of pressure in cuprates is to study the phases that are competing or contributing to superconductivity and to demystify the nature of those phases too. Here we only mention the related pressure effect on our material of interest Nd-LSCO.

CDW modulations in LSCO itself have been studied and are found to cause distortion in the CuO_2 planes near the doping of $p = 0.12$ which is thought to be the source of 1-D modulations [63]. Observing the structure of CuO_6 octahedra in this material could be useful for understanding this phase. In this material, two different simultaneous modulations have been detected. In Fig 1.14 the two different kinds of octahedron structures that give rise to these different stripe modulations are shown. The Cu sites form stripes of the distorted lattice (D-stripes), that are intercalated by the stripes of an undistorted lattice (U-stripes). Moreover, the LTT (low temperature tetragonal) type of distorted CuO_6 octahedra is assigned to the D-stripes and the U-stripes are assigned to the LTO (low temperature orthorhombic) structure. As LSCO is the strongest material (its lattice is less susceptible to deform by the application of pressure) in Lanthanum family of superconductors [66], the effect of pressure should not be highly noticeable in it. So to check the effect of pressure in stripe or charge order, we turn to LBCO, that is the first cuprate that was discovered [67], which is both close to Nd-LSCO structure-wise and is in the same family of Lanthanum superconductors. Fig 1.15-a shows the crystal structure of LBCO. At the copper oxide plane, where the super-current passes, any sort of distortion could affect the superconductivity. Above and below that plane are two oxygen atoms that form the CuO_6 octahedra that are mentioned above. In Fig 1.15-b, the configuration that gives rise to the LTO phase is depicted. The tilting angle (direction) which is a measure of the orientation of this octahedron are shown as well. In Fig 1.15-c the configuration of an octahedra which is responsible for the LTT phase is shown.

The situation is more or less the same in Nd-LSCO too. In Fig 1.15-d the CuO_6 octahedra in Nd-LSCO is shown. To better categorize different structures in Nd-LSCO, one can define an order parameter called Q. It determines the tilting direction of these octahedron. The HTT rotation axes are defined as (110) and (1-10) as shown in Fig 1.15-d. If the octahedron

[6] However, the highest T_c record holder is sulfur hydride [5] at the moment with the T_c of 203K, it is not a cuprate though and it is the classical BCS superconductor so does not have lots of practical advantage of cuprates, for instance, its critical field at 200K is below 500Oe, on the other hand, reaching the pressure of 200GPa is extremely difficult (the pressure of the outer core of the earth is 330GPa and Iron melts at that pressure).

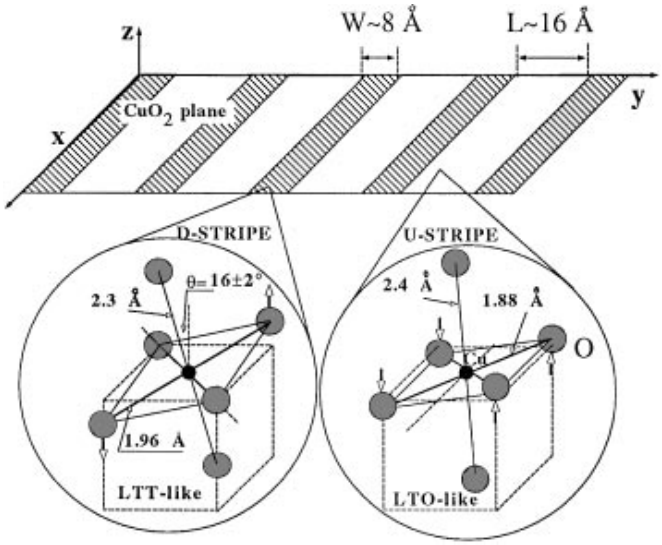

Figure 1.14 The CuO_6 octahedron is distorted due to the stripes. In the right side the so called D-stripe type has the form of LTT and on the left side the U-stripe type has the LTO structure specific width for each stripe is shown. This pictorial view is obtained from Ref[63].

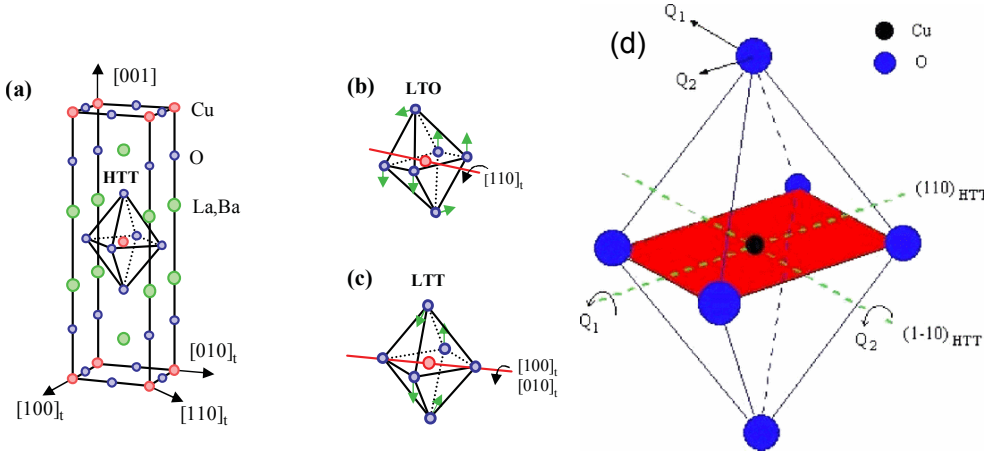

Figure 1.15 a) Crystal structure of LBCO in HTT phase is shown. b) The LTO phase and the tilting direction is shown. c) LTT phase and its tilting direction, obtained from Ref [64]. d) octahedra structure of CuO_6 in Nd-LSCO, blue and black circles are showing oxygen and copper elements respectively different axis of copper oxide plane are shown and rotation around these axis with order parameters of Q_1 and Q_2 are shown. Depending on the rotation, sample goes through LTT, LTO 1 or LTO 2 transitions, obtained from Ref [65].

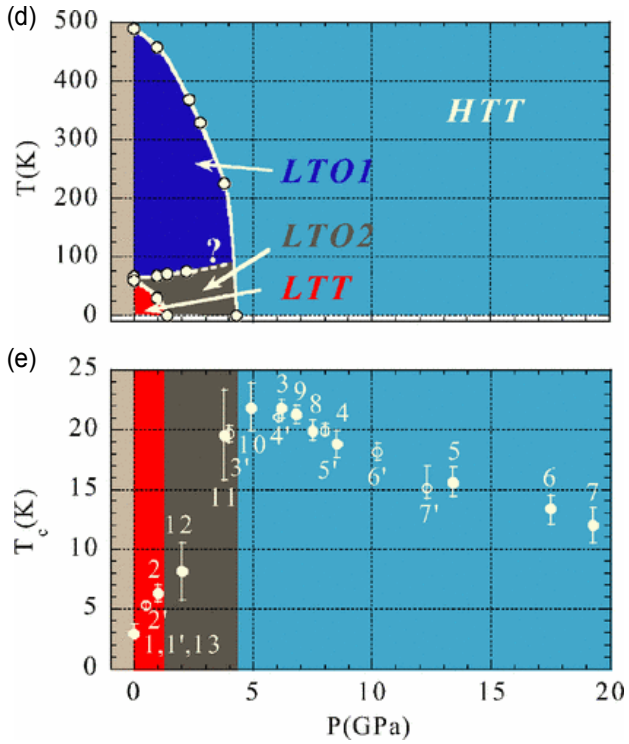

Figure 1.16 Structural phase diagram of Nd-LSCO as a function of temperature and pressure obtained by x-ray diffraction. Top: LTT phase (red) is located at low temperatures and could be suppressed by modest pressure of less than 2GPa. LTO2 (gray) and LTO1 (blue) are located above LTT and the transition between LTO2 and LTO1 fades out above 2GPa marked with a question mark. Above 4.2 GPa all the CuO_6 octahedron become ordered and the tilt angle $\rightarrow$0 that cause a structural transition to HTT. Bottom: Critical temperature of Nd-LSCO $p = 0.12$ vs applied pressure. The colour code is the same as the top Figure. At ambient pressure T_c = 3K and the highest T_c is 22K at P = 5GPa in HTT phase. Obtained from Ref [65].

rotates with respect to any of these axes in a single rotation by the magnitude of $|Q_1|$ or $|Q_2|$ the LTO1 structure appears. The twin structure of LTO1 is LTO2 that is obtained by simultaneous rotations with the magnitude of Q_2 and Q_1 around both HTT rotation axes, provided that $Q_1 \neq Q_2$. Finally for the formation of LTT lattice $Q_1 = Q_2 \neq 0$.

The effect of pressure has been studied in Nd-LSCO at $p = 0.12$ with x-ray diffraction [65] up to very high pressures. The top panel in Fig 1.16 shows the structural phase diagram of Nd-LSCO as a function of pressure and temperature. By increasing the pressure, the LTT phase (red) is suppressed and the structural transition from LTO2 (grey) to LTO1 (blue) increases to higher temperatures. However, the structural transition itself becomes harder to resolve (discussed in chapter 3 and denoted by a question mark in this Figure). Finally, in pressures higher than 4.2GPa, the tilt angle $\rightarrow$ 0 and the structure transforms to HTT up to the highest achievable pressures. It is shown that pressure favours the orthorhombic

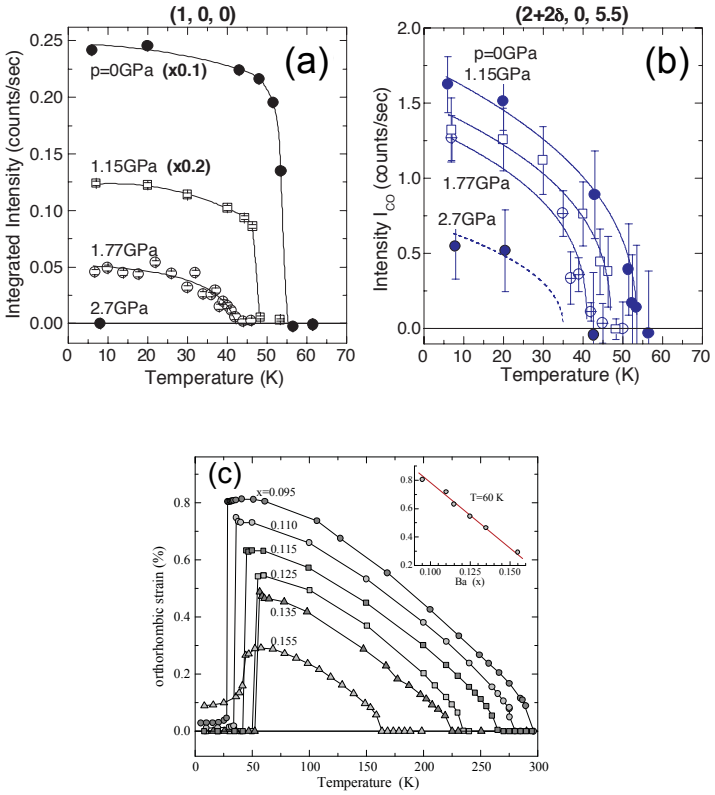

Figure 1.17 a) Temperature dependence of the integrated intensity of x-ray diffraction peak at (100) which is the signature of LTT phase, by 2.7GPa this phase is fully suppressed. b) Temperature dependence of the intensity of the peak that is corresponding to charge order. Same pressure did not suppress charge order whereas it suppressed LTT phase. Obtained from Ref[68]. c) Orthorhombic strain as a function of doping. The sharp drop is a structural transition from LTT to LTO and the curve for x = 0.15 is different due to mixture of these different phases, obtained from Ref. [64].

structure (LTO2) of the lattice by reducing the tilt angle of CuO_6 octahedra (fig1.16) and eventually it favours the HTT phase in pressures higher than 4GPa. The bottom of Fig 1.16 shows the evolution of T_c vs pressure. T_c from 3K increases up to 22K at 5GPa and after that it decreases again and this drop might be due to the fact that higher pressures squeeze the c-axis. [7]

In this work, we study the effect of pressure on both thermoelectrical and electrical transport properties of Nd-LSCO under pressure at dopings which are located in the CDW region and at dopings around p*. Below, a few relevant studies on the nature of the pseudogap and CDW phases are mentioned.

X-ray and neutron scattering experiments have detected stripe order in the $La_{2-x}Ba_xCuO_4$ (LBCO) superconductor around the doping level of $p = 0.12$ [64]. It is shown that the

[7]The resistivity can reveal the structural transition in Nd-LSCO for some dopings, by showing an anomaly (a glitch) in the temperature dependence of resistivity.

presence of these stripes is not necessarily due to the crystal structure. By suppression of the LTT structure in LBCO (that is shown by a disappearance of the (100) peak), the stripe order is not fully suppressed as shown in Fig 1.17-a. The LTT phase fades out but the CDW phase is not yet fully suppressed (In Fig 1.17-b the peak, that is the signature of charge order, partially fades out). Fig 1.17-c shows a systematic decrease of the LTO strength as a function of doping. The jumps show the LTO to LTT transition. Only at x = 0.15 the transition is a result of mixed LTO and LTT phases; the rest have sharp transitions [64]. Hence, one can conclude that the effect of pressure is the same as increasing the doping; that in both cases the intensity of LTT phase decreases. Another important conclusion is that the LTT phase is not necessary for the CDW formation.

Magnetization and muon spin rotation studies under pressure in LBCO reveal the competition between superconductivity and spin stripes and show that the pressure of 2.2 GPa can partly suppress the spin stripe modulations and reduce the magnetic volume fraction of the static stripe phase, although, they are still present after the suppression of LTT phase[8] (x = 0.125) [70].

For the first time, we were able to measure thermoelectricity of cuprate superconductors under pressure and in high magnetic fields. We have developed our setup based on the following studies. Thermoelectricity under pressure has been measured in the organics [71] and more recently in pnictide family of superconductors [72]. The seebeck coefficient has been measured in YBCO and LSCO [73, 74] in a different range of doping up to 1.5GPa, but not at many different pressures. Thermoelectric power has been measured in a polycrystalline sample of Hg-1245, however in less than 1GPa [75]. The temperature dependence of the Seebeck effect in the pnictides has been studied under pressure as well [72]. The Seebeck effect under pressure is also measured in $La_{1-x}Nd_xCuO_3$ at x = 0.5 which is close to the Mott-Hubbard transition and is not a superconductor [76].

Electrical transport studies under pressure have been done on Nd-LSCO at $p = 0.12$ [77], but the data are not systematic. We had a closer look at this material and investigated the effect of pressure on the adjacent and the same doping to study the competition between charge order and superconductivity by tuning the CDW with pressure.

[8] Based on the pressure dependence of LTT phase [69, 64].

Chapter 2

Experimental techniques and developments

In this chapter, the expertise that we developed to perform transport measurements under hydrostatic pressure, AC thermoelectricity measurements and high pulsed magnetic field experiments are discussed.

2.1 Transport experiments at ambient pressure

2.1.1 Resistivity and Hall Effect

Nowadays electrical transport measurements are considered to be one of the most available and conventional experimental probes. By applying the electrical current between two points and measuring the voltage drop, one can obtain resistivity based on Ohm's law. The applied potential exerts the force of F = $-e$E on free electrons in a metal. Then for each electron $-e$E = m (dv/dt) where m is the electron mass. If the time between the collisions, defined as τ (Drude's relaxation time), the electron velocity is:

$$v = \frac{-eE}{m}\tau \tag{2.1}$$

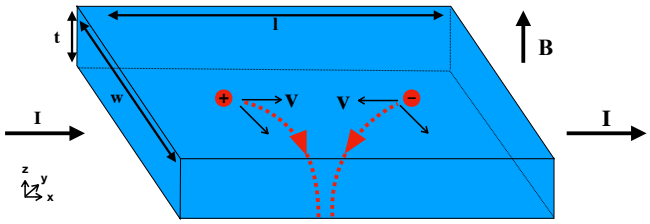

Figure 2.1 Hall effect schematics. The deviation of electrons and holes are shown in the presence of a magnetic field. The direction of electron and hole movement is denoted by ν. The current is applied along the x-axis. The sample thickness, width and length are shown by t, l and w respectively.

The definition of current density (j), is the number of electrons with charge e that move with a certain speed in a given cross-section. Here we assume that the average electron's speed is 2.1. Therefore

$$j = ne\nu = \frac{ne^2\tau}{m}E = \sigma_0 E = \frac{E}{\rho_0} \tag{2.2}$$

and the DC electrical conductivity is the inverse of ρ_0 which is the value that we measure [1].

By measuring the Hall effect, one can obtain the mobility and sign of carriers. As shown in Fig 2.1 electrons or holes with charge -e and +e are deviated by the Lorentz force, F = q$\nu\times$B, in the magnetic field that is applied upwards along the z-axis. Then with transverse contacts on the sides of the sample and along the y-axis, one can measure the voltage that is the consequence of electron or hole accumulation on one side of the sample. This voltage produces an electrical force that is in balance with the Lorentz force:

$$E_y q = q\nu \times B \tag{2.3}$$

where q could be $\pm e$. The Hall coefficient R_H is defined as

$$R_H = \frac{E_y}{j_x B_z} = \frac{\nu B_z}{ne\nu B_z} = \frac{1}{ne} \tag{2.4}$$

and experimentally we have dimensions of the sample (length, width and thickness) and we measure transverse resistance in a given magnetic field, so R_H could be calculated in

[1] In appendix (C), there is a brief discussion on AC electrical conductivity and dependence of electrical resistivity on the frequency of applied current in the samples that we measured here.

this form:

$$R_H = \frac{E_x}{j_y B_z} = \frac{V(w \cdot t)}{I \cdot w \cdot B_z} = \frac{\rho_{xy} t}{B_z} \tag{2.5}$$

We used the conventional four-point probe method for resistivity and Hall effect measurements. By applying a current to a sample along its longitudinal contacts and measuring the voltage drop, one can measure resistivity. Transverse contacts on the sample in the presence of magnetic field, allow us to measure the Hall voltage which is the result of the accumulation of electrons and holes on one side of the sample because of Lorentz force.

The first step is to make contacts on the sample through which we can apply current and measure voltage. Since the dimensions of samples that we use are tiny (between 200-20 μm in thickness, less than 500 μm in width and between 400 and 1500 μm in length), preparing the contacts should be done with caution. In Figure 2.2 one of our typical samples is shown with longitudinal and transverse contacts.

We use H20E EpoTek silver epoxy to prepare the contacts. We place a pair of longitudinal wires, a pair of transverse wires, and a pair of wires for current at the two ends of the sample (figure 2.2). Then by applying the silver epoxy on top of them, we fix them in place. To diffuse the contacts, one can put the sample in a cylinder furnace for 1 hour in 500°C while oxygen flows in the quartz tube. In contrary to Bi2212, Bi2201 and YBCO superconductors which are susceptible to lose oxygen if they were warmed up to high temperatures for a long time, the samples on which we made contacts (LSCO family samples) are not susceptible to oxygen loss at this temperature. Therefore their doping would not change. It is necessary to have oxygen flow during that process to have the contacts diffused better into the sample.

All the resistivity and Hall effect measurements have been done either with the Quantum Design PPMS with a 16T magnet or with Oxford Instruments cryogenics with 18 T or 15 T magnets. The built-in electronics in the PPMS and its resistivity option was used for the electrical transport measurements. The applied current for electrical transport measurements is usually either 2mA or 5mA. Keithley Model 6221 AC and DC Current Sources are employed to apply the current in instruments other than the PPMS (and whenever we did not use the built-in option of the PPMS).

For Hall effect experiments, we were able to improve the signal to noise ratio by applying higher currents up to 20mA (in the situations where the sample was not warmed up by such a high current). Another way to amplify the output signal is to use the pre-amplifiers. The former option is easy to do with PPMS AC Transport option, and it is feasible by using an external breakout box to access the wires on the PPMS puck which are connected to the sample. However, we could not use the built-in electronics of the PPMS in this case. The latter method (using amplifiers) proved to be more straightforward.

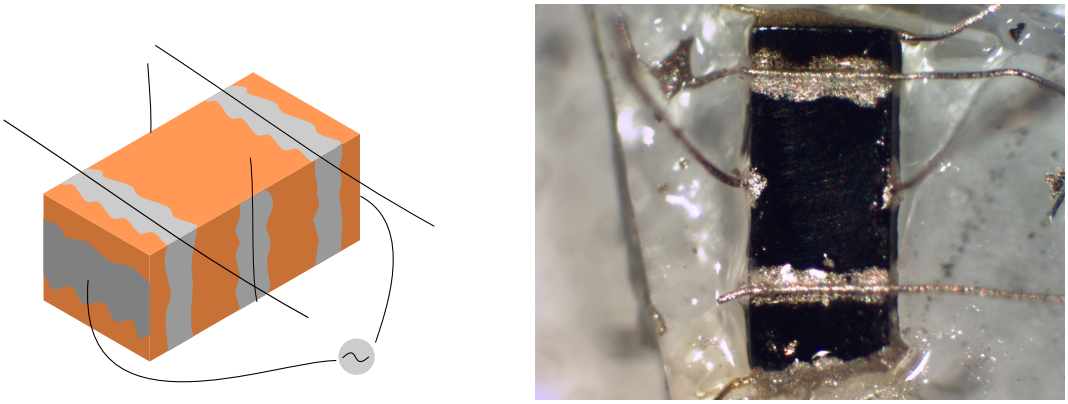

(a) (b)

Figure 2.2 Schematics of resistivity and Hall effect contacts configurations.

In general, we use silver wires with 25μm diameter. By using wires with bigger diameters, we were able to apply higher currents without breaking the wires. In pressure cell, as pressure medium surrounds the sample (and it solidifies in high pressures and low temperatures), we never observed that a wire breaks.

2.1.2 Seebeck and Nernst Effect

A conductor that does not have any electric current flowing in it can produce an electric field E by the application of a thermal gradient ∇T through it. This can be written in the form of voltage difference:

$$S\nabla T = E \;\; ; \quad S = \frac{\Delta V}{\Delta T} \tag{2.6}$$

where S is the thermopower or Seebeck coefficient. In the simplest approximation, the Seebeck coefficient can be expressed more fundamentally [78] as:

$$S = \frac{\pi^2 \cdot k_B T}{2eT_F} = 425\left(\frac{T}{T_F}\right)\mu V/K \tag{2.7}$$

where T_F is the Fermi temperature and can be on the order of 10^4K. To measure thermoelectricity, particularly the Seebeck and Nernst effects, we use the same contact configurations that is in use for measuring the resistivity and Hall effect. The difference is that we measure the potential difference that emerges due to the presence of a thermal gradient. Here, instead of a current, a thermal gradient is applied via a heater and either

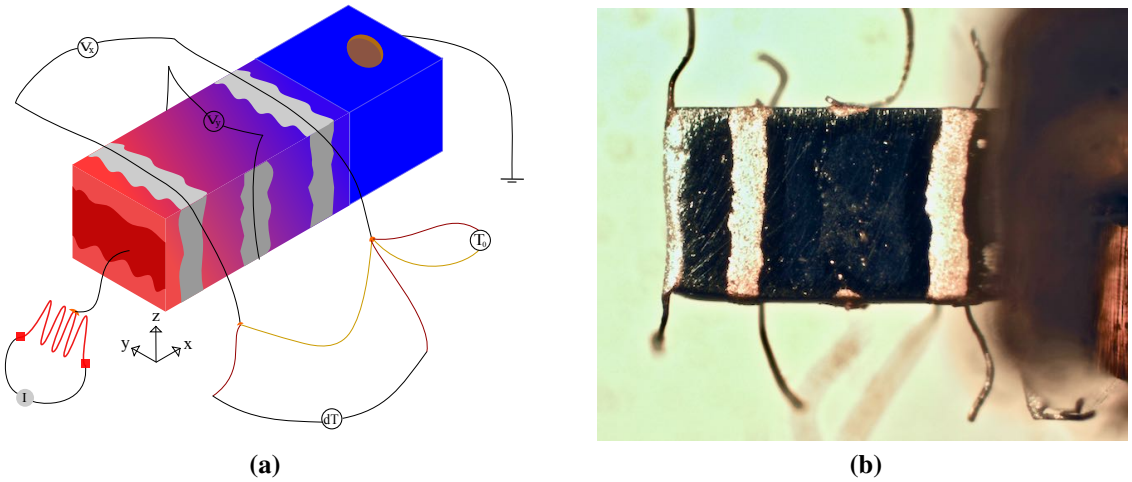

(a) **(b)**

Figure 2.3 a) Schematic of Thermoelectric experiment. b) A sample mounted on a Copper block.

thermocouples or conventional calibrated thermometers (e.g., Cernox) measure this thermal gradient. We discuss the former method of thermometry here (using thermocouples).

As depicted in Figure 2.3, a strain gauge produces thermal excitations on the left side of the sample. We use a heater with a resistance of 120Ω in the pressure cell. The other end of the sample is attached to a Copper block (blue cube) via silver paste. The Copper block is screwed to part of the probe, thus it is in good thermal contact and a thermal gradient stabilizes across the sample.

We use Constantan-Chromel-Constantan (colour-coded as Purple-Gold-Crimson wires in the Figure), also known as type E thermocouple, as a differential thermocouple. The two junctions of Constantan-Chromel are connected by spot welding. Then we use Ge-varnish (shown by orange semicircle), which is an insulating paste, to connect each junction to one end of the longitudinal contacts of the sample. One should avoid any electrical contact between thermocouples and the sample since in a closed-circuit condition as electrical current can flow and contaminate the Seebeck voltage of the thermocouples that would be used later on to calculate the temperature difference between the two contacts. Type E thermocouples are non-magnetic materials and typically used for cryogenic purposes. The only issue that we have with the thermocouple is that it loses its sensitivity as its Seebeck coefficient $S \to 0$ as $T \to 0$, but for $T > 2K$, it is precise enough.

We use an absolute thermocouple that consists of Chromel-Constantan wires, spot-welded together, with which we can measure dT_{abs}. We need T_0 to calculate the Seebeck coefficient of the thermocouples. To calculate dT we measure the thermocouple voltage both

when the heater is on and off, denoted as $V_Q(dT_{abs})$ and $V_0(dT_{abs})$ respectively.

$$dT_{abs} = \frac{V_Q(dT_{abs}) - V_0(dT_{abs})}{S(T_0)} \tag{2.8}$$

In which $S(T_0)$ is the Seebeck coefficient of Type E thermocouple at T_0. For calculating dT_x one can use the following equation:

$$dT_x = \frac{V_Q(dT_x) - V_0(dT_x)}{S(T_0 + dT_{abs})} \tag{2.9}$$

We use the other end of the longitudinal silver contacts to measure Seebeck voltage and the transverse contacts to measure the Nernst voltage of the sample. These contacts are connected to two separate Phosphor-Bronze coils. Phosphor-Bronze alloy is known to have low thermal conductivity and excellent low resistance. Moreover, Phosphor-Bronze wires produce negligible Seebeck voltage and allow for a very little contamination of the signal. The other end of the Phosphor-Bronze wires is connected to the Copper wires of the probe which bring out the signal from cryostat. Then we use DC amplifiers to amplify the voltage by 1000 times, in the end, we measure the voltage difference with Keithley nanovoltmeters.

To calculate S and N coefficients, we use the following equations:

$$S = \frac{V_S}{dT_x} \tag{2.10}$$

$$N = \frac{V_N}{dT_x \cdot (L/w)} \tag{2.11}$$

2.1.3 Thermal conductivity

A thermal conductivity experiment has a set-up similar to the thermoelectric measurements. We apply heat with a heater (Q), given by $Q = R \cdot I^2$ where R is the resistance of the heater and I is the applied current to it. A temperature difference dT_x across the sample can be obtained in the same way that was explained in the previous section of this chapter. Hence, the thermal conductivity can be measured as follows:

$$\kappa = \frac{Q}{dT_x \cdot \alpha} \tag{2.12}$$

where α is the geometric factor of the sample i.e., w·t/l.

2.2 Transport experiments under pressure

As discussed in the Chapter one, there are many physical justifications for performing high pressure experiments. However, one of the challenges that one faces is that there is a considerable constraint in the volume of sample space that is subject to high pressure. Thus, everything inside the cell and in sample space has to be optimized to occupy a smaller volume. If one wants to reach higher pressures (in different types of pressure cells), the sample space becomes even smaller.

2.2.1 Pressure cell, medium and preparation process

We used conventional clamped pressure cells made with CuBe and NiCrAl (Nonmagnetic materials), designed and manufactured by C & T company in Japan. The bore of the cells that we used are either 6 or 5 mm, and the sample space diameters are 4.5 or 4 mm. Their commercial names are CTF-HHPC60 and CTF-HHPC50 respectively. The pressure medium is Daphne oil 7373 in all of the experiments. We record applied pressure by measuring the resistance of a homemade lead (Pb) gauge inside the cell next to the sample. The ratio of resistance at a given pressure over the resistance at the beginning of the experiment yields the pressure inside the cell [79]. The highest achievable pressure is about 2.2 GPa (22Kbar) in 5mm pressure cells, and we achieved 1.7 GPa in 6mm pressure cells.

As depicted in Figure 2.4-a, the simple structure of a pressure cell is two clamps, one that is fixed under the feedthrough and cannot move and the other that is on top. By screwing down the top clamp, the pressure is increased inside the cell. Fig2.4-b shows a more detailed version of the cell. Pressure will be applied inside a Teflon cap that is filled with pressure medium and is surrounded by the pressure cell, enclosed by a piston from above and by a feed-through from the bottom. The only way to access the sample inside is via the wires that pass through the feed-through which is the most vulnerable part of the pressure cell. In a 5 mm pressure cell, we pass six pairs of twisted wires with the gauge 46 (bare dim. of 0.03983mm) through, and in a 6mm cell, we pass seven pairs of wires through that hole (same gauge). Next, we apply a strong epoxy on top of it and through the hole, to ensure that no pressure medium could leak through. By pressing the piston, the pressure inside the cell increases and by screwing the upper locknut, the pressure inside the cell remains stable. We use a ”w” shaped Pb gauge for measuring the pressure inside the cell in ambient temperatures. In that regard, we use the calibration table that is mentioned in Ref [79]. The detailed procedures are explained in [80]. One should bear in mind that the mentioned number of twisted wires is the limit for this wire gauge and this cell. If one wants to pass more wires there is a risk of either scratching the insulating part on the wires or else the Stycast may not pass through the hole properly, causing a leak. One can use wires with a bigger gauge (smaller diameter), and pass as many as 20 pairs (for 56-gauge wire

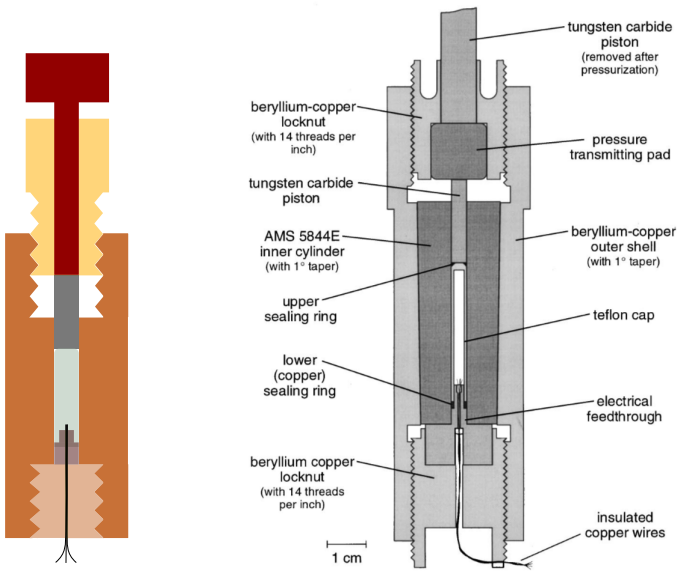

Figure 2.4 a) Schematic view of the self-clamped pressure cell that we used (simplified). b) Detailed realistic schematic of pressure cell obtained from Ref [80]

for instance), but working with those wires will require extreme cautions as they are very delicate. As we did not have significant sample space to measure more samples, we did not need more wires, so the 46-gauge wire was adequate.

To prepare the epoxy, we use Stycast 2850 FT and catalyst 11 made by Henkel Loctite (previously known as Emerson & Cuming). After applying the epoxy to the drilled hole in the feed-through next to the wires, we cure the Stycast for two hours in 100C. This Stycast has a low thermal expansion, excellent thermal conductivity, electrical insulation and thermal shock resistance. The compressive strength of this mixture is 193 N/mm^2, and Flexural strength is 117 N/mm^2. These are the highest values compared with other mixtures of this Stycast with other catalysts (namely number 23 and 9). Therefore this mixture is the best candidate for pressure applications. The uncured epoxy mixture with this catalyst has a considerable pot life giving us enough time for vacuum degassing the mixture to make sure that no air is confined there that can decrease the strength of the Stycast.

Once the feedthrough is ready, we install the sample that we want to measure on top of the feed-through accompanying with other parts that will be explained later in this chapter. Next, we put the sealing ring on top of the feed-through and put it in a Teflon cap that was previously filled with Daphne oil. Then, it is inserted into the cell as it is sketched in Fig 2.4. A locknut is screwed all the way beneath it and holds it from below. Afterward, we put a second sealing ring outside the Teflon cap and on top of it. Moreover, we put a cylindrical internal piston on top of it that is supported by a pressure transmitting pad and can be pushed

by the second external piston on top of it.

The process of the pressurization is as follows:

1- By holding down and pushing the internal piston via external one via a press, one can increase the pressure on the pressure medium.

2- As explained before, we have to sustain this pressure inside the cell, so that is why we need another locknut (yellow coloured locknut in the sketch of Fig 2.4) on top of the transmitting pad to hold it down, even after removing the applied force of the press.

3- The further one pushes down the piston, the higher the pressure will be. By screwing the higher locknut in the threads as tight as possible, we can sustain the applied pressure.

4- One should note that this process should be done in step by step procedures, i.e., we aim to increase the pressure on the ram (Force on the outer piston) by 10bar increments, then we tighten the higher locknut screws, record the resistance of the pressure gauge and aim for the next pressure point.

Quantitatively, 100-110 bar of pressure that the press applies on the pressure cell corresponds to 20Kbar of pressure inside the cell. The compressibility of Daphne oil is considered to be negligible.

Before starting all the measurements, we cooled down the pressure cell with a slow rate (about 0.5 K/min) to ensure homogeneity of the pressure medium inside the cell.

2.2.2 Electrical transport under pressure

There is no difference in the experimental setup for electrical transport under pressure and in ambient pressure. The only constraint that is present in the pressure is small sample space. Our method is based on the previous well-established methods for this kind of measurements in ambient pressure [81] and under pressure[71] and [82]. We could only pass six pairs of wires through the feed-through. We need two pairs for measuring the pressure gauge, two to measure resistivity and two for measuring resistivity in another sample. Alternatively, one can measure more properties by sharing the current wire between the two samples and pressure gauge and recover two wires. Now resistivity and Hall effect on each sample can be measured at each pressure point which results in cutting the required time for these experiments in half.

Each sample should have a length smaller than 1mm to fit in our pressure cell. The thickness and width of the samples that we measured are typically less than 500 μm and 200 μm respectively.

We prepare our pressure gauge each time by wrapping a pure lead tape in "M" shape and spot welding two silver wires with a diameter of 25 μm on its two ends.

2.2.3 Thermoelectric transport under pressure

The experimental set-up for transport under pressure is shown in Figure 2.5-a. All the experimental setup is assembled on top of a feed-through, and seven pairs of copper wires pass through it. These wires hold a cross-shaped plastic board which contains six pairs of copper holes that are soldered to those copper wires. The realistic picture is shown in Figure 2.6. The sample (denoted by s) is glued with silver paste on top of a copper block (c) that is soldered to the two copper holes and thermalized to the probe via one wire. One pair of copper wire that is connected to the copper connector at (a) measures the Seebeck voltage and the connectors next to it (b) measure the Nernst voltage. A chromel-constantan absolute thermocouple measures the low-temperature side of the sample close to the copper block. We measure the temperature of the pressure cell with a Cernox thermometer out of the pressure cell. We compared these temperatures and realized that the temperature difference is less than 1K. Consequently, one can use the temperature of the pressure cell instead of the temperature that the absolute thermocouple delivers as T-. A constantan-chromel-constantan differential thermocouple on one side thermally connects to the longitudinal contacts of the sample and on the other side connects electrically to the connector (e). When the heater (f) is on, we measure the dT between the longitudinal contacts.

To be capable of measuring electrical transport on the sample, we use two wires of the same pair for the application of current and measure resistivity and Hall effect with sample wires that were conveying Seebeck and Nernst voltage in Thermoelectric setup.

The measurement principle is explained in section 2.1.2 of this chapter. One of the differences is that the pressure medium inside the cell encloses the sample. So the heat flows both through the sample and the pressure medium. Besides, we get a temperature difference in order of a few millikelvin and the sample also thermalizes quite quickly. As shown in Figure 2.5-b, the heat current propagates in a spherical form (if we use AC current for the heater it generates spherical thermal waves) that transverse through the sample as well as the other components of the experiment that are mounted on top of a plastic board. We choose the configuration of the connector on the plastic board to be transverse with respect to this thermal wave so that each of these connectors is at the same temperature. This is especially important for the thermocouples.

In the DC technique that was discussed in the previous section, in a given temperature, the heater is on until the value of Seebeck and Nernst voltage as well as dT become stable. Then we measure for a couple of minutes and average the value. This method is extremely time-consuming, and at the end of the measurement, we have data only in discrete tempera-

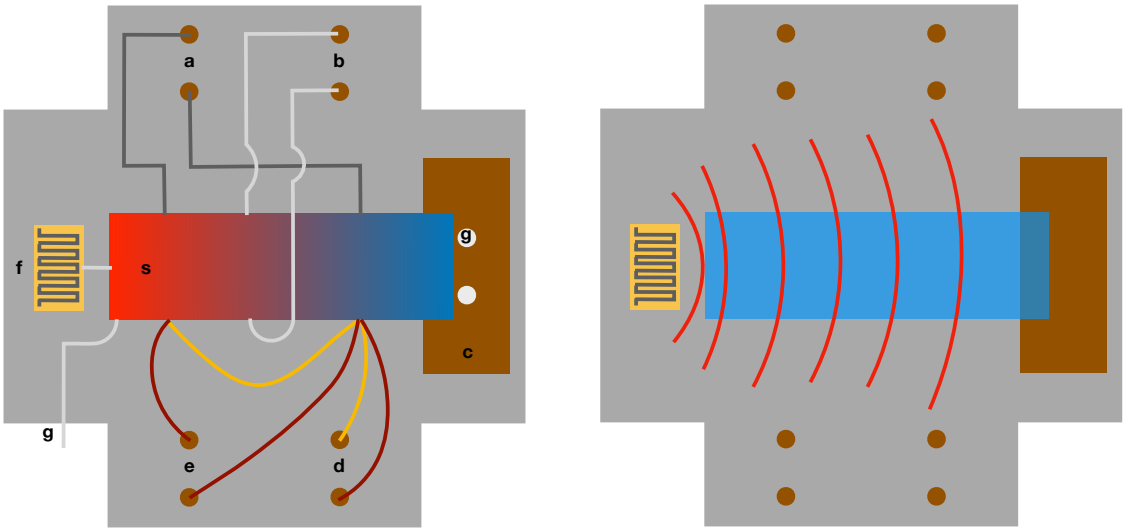

Figure 2.5 a) Full configuration of thermoelectric setup mounted on a plastic plate with copper holes; a-Seebeck voltage connector, b-Nernst voltage connector, c-copper block, d-absolute thermocouple connector, e-differential thermocouple connector, f-heater, g-two wires of the same pair for the application of current, s-Sample b) Schematic of heat propagation waves inside the cell and pressure medium.

ture. So we decided to use an AC technique to be able to do temperature sweeps and have a faster measurement.

2.3 AC technique for thermoelectricity experiment under pressure

The leading governing principle that allows us to use the AC technique is that the stability time for Seebeck and Nernst signal as well as dT is remarkably small (less than a second) inside the pressure cell (not in the vacuum), as pressure medium transfers heat. In the AC technique, it is crucial to measure the dT and the Seebeck voltage of the sample with the same phase. Therefore, placing the thermocouple and the heater very close to the sample helps to lower the stability time too (maybe by decreasing the distance between the heater and the thermocouple, one can perform the AC thermoelectricity measurements in the vacuum as well).

The design is the same as it was explained before. The only difference is that we apply square Alternative Current to the heater. Consequently, the heater generates an alternating thermal gradient in the sample which is equal to the case of heat-on and heat-off that was

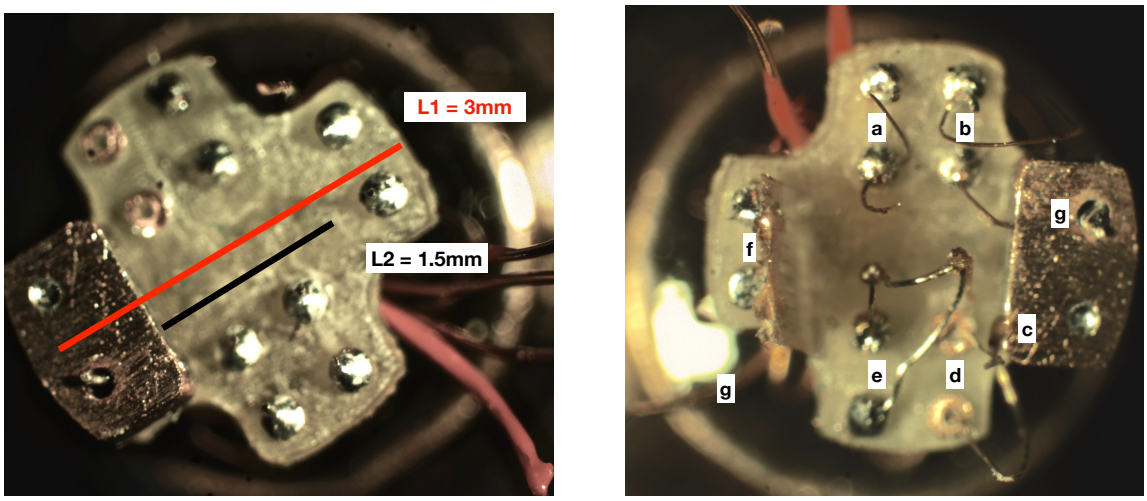

(a) (b)

Figure 2.6 a) Realistic view of cross-shaped plastic board mounted on top of a feed-through. The metallic rectangle on the left of the photo is a copper block that is soldered on top of the feed-through and one of the wires of a pair of wire passed through it. L1 is the length and width of the plastic board. L2 is the length between the copper block and the heater. L2 is the typical length of the sample. b) Plastic board with mounted parts; a and b are phosphor-bronze wires and only the two ends of them do not have insulation.

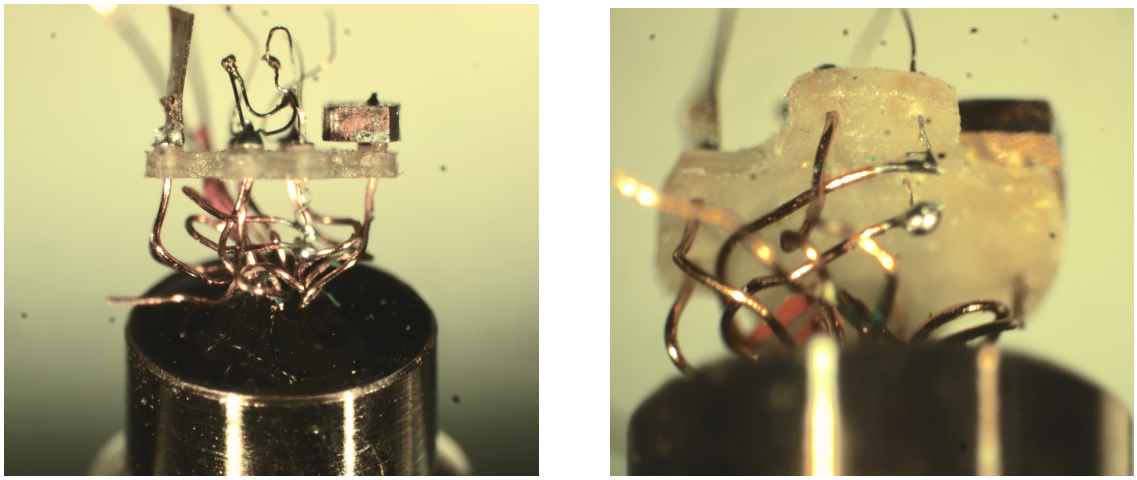

(a) (b)

Figure 2.7 a) Side view of plastic plate as shown from top view in 2.6-b. b) Under the plastic board. On the right side of the photo before the copper block, a chromel-constantan absolute thermocouple is shown. It is soldered to the copper wires of the feed-through under the plastic board.

mentioned earlier in this chapter. To measure the output signal, we first amplify the voltage signals (Seebeck and Nernst and thermocouples) 1000 times via home-made amplifiers then we use SR830 Lock-In amplifiers. When first implementing this technique, we would measure dT by locking the frequency of the lock-in amplifier at the frequency of the applied current. After further developments, we figured out that using a square excitation is preferable (as it abruptly turns the heater on and off) compared with the sinusoidal excitation.

In the beginning we applied the current of the order of 0.3 Hz with the amplitude ranging between 2-5 mA to the heater. For square excitations, we applied the current with the frequency of 0.05 Hz. But one should pay attention that at high pressure, the thermalization of the sample is faster compared to lower pressures, meaning that at higher pressure one can apply current with high frequency.

2.4 High magnetic field experiments

There is hardly any difference between the high magnetic field set-up and other set-ups, since we often bring our probe for measurements, but there are some technical constraints in different high field facilities.

In pulsed magnetic fields (Toulouse), the sample space for a 90T magnet is quite small. Fig 2.8 displays the top and side view of this sample holder. We can mount one sample on top of the sample holder which has a diameter of 4mm and one in a small window below it with a diameter of 1.5mm.

The duration of the pulse is usually of the order of milliseconds, so the measurement must be performed at high frequencies (about 40KHz or more) and this requires a high-speed acquisition card for recording the data. The ideal sample for these measurements is a sample with a small thickness which gives a higher Hall signal and residual resistivity ($\rho(0)$). The contact resistance of the sample should also be small, as low contact resistance can eliminate or decrease the out of phase signal which could be substantial in high-frequency measurements.

To avoid any movement during the pulse, we need to fix everything including the wires and samples with Ge-Varnish. Moreover, in order to have the less electromotive force exerted on the wires due to changing the magnetic field dB/dt (magnetic induction) it is important to minimize loops, as shown in Fig 2.8.

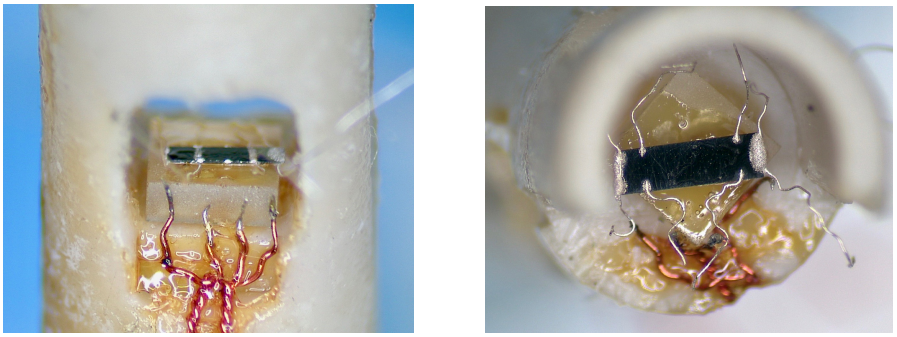

(a) **(b)**

Figure 2.8 Toulouse sample holder with mounted samples a) Top view b) Side view

Chapter 3

Results

To study the interplay between charge density wave, pseudogap, and superconductivity, we performed a series of experiments over a wide range of temperature and various tuning parameters of pressure, doping and magnetic field to understand the ground state and mechanism of the cuprates in general and in the LSCO family of superconductors specifically.

Figure 3.1 shows a cartoon of the Nd-LSCO phase diagram (similar to the Fig 1.1, but less generalized compared to that figure). It shows different parts of the phase diagram of Nd-LSCO that we studied. At the beginning of this chapter, we discuss the signatures of the CDW and pseudogap phase on the Hall effect. At the high magnetic field, we were able to measure those signatures by suppressing the superconductivity phase and reaching the normal state.

We discuss the signatures of the CDW and pseudogap phase on the temperature dependence of the Seebeck coefficient over temperature. By comparing the Seebeck coefficient of many different dopings at low temperature and in a high magnetic field, we located the end point of the CDW phase (as shown in Fig 3.1 by a blue arrow and p_{CDW}).

In the subsequent section, we discuss the evolution of the CDW phase under pressure by tracking its signatures on the Seebeck and Hall coefficients both at moderate and high magnetic fields down to low temperatures. We show how the Fermi surface can be tuned by using the hydrostatic pressure and magnetic field (it is shown in Fig 3.1 by an orange arrow).

Afterward, we presented the pressure effect on the pseudogap critical doping and temperature (p* and T*) probed by the electric and thermoelectric probes. We discuss the pressure effect on the p_{FS} and explain the necessary constraint on the topology of the Fermi surface inside the pseudogap phase. The dopings at which we applied pressure are shown by red arrows in Fig 3.1.

Finally, we show the magnetic field dependence of the resistivity isotherms in Nd-LSCO

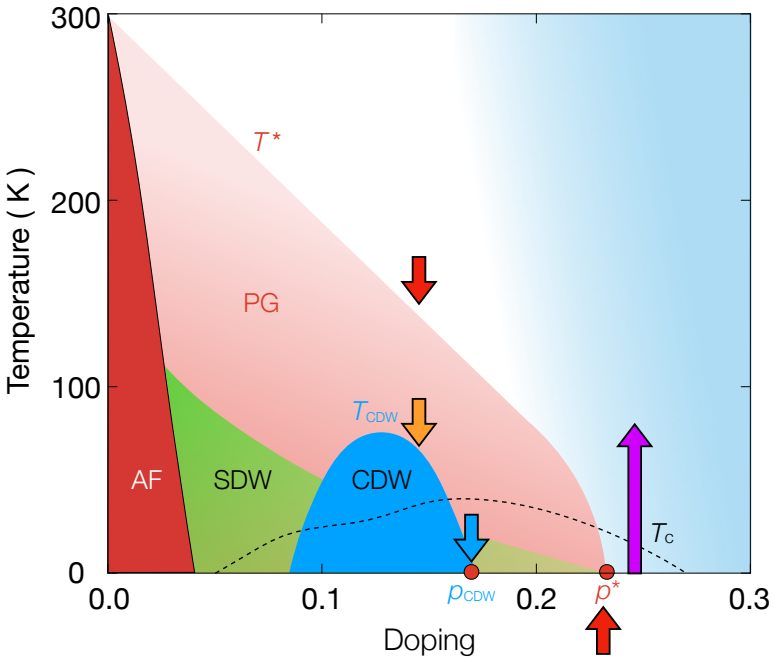

Figure 3.1 A sketch of the Nd-LSCO phase diagram. Arrows are showing different parts of the phase diagram that we studied. Red and orange arrows are showing where we applied pressure to tune the pseudogap and CDW phase respectively. Blue arrow is showing the end point of the CDW phase. We located the end point of this phase. Purple arrow is showing the strange metal part of the phase diagram where we studied the magnetoresistance at different temperatures and in high magnetic fields.

at $p = 0.24 > p* = 0.23$ and in LSCO at $p = 0.24 > p* = 0.18$ up to 84T. We discuss the quadratic and linear scaling of the magneto-resistance for dopings close to the quantum critical point and farther from it over a wide range of temperature (as shown in Fig 3.1 by a purple arrow).

3.1 Charge density wave order

As mentioned in Chapter one, the pseudogap appears at higher temperatures and dopings compared to the CDW (fig 1.1). In transport experiments, the Hall coefficient is affected by the presence of CDW and pseudogap. The signature of CDW is a downturn and the signature of the pseudogap is an upturn in the temperature dependence of Hall coefficient. Figure 3.2 shows the temperature dependence of R_H at the magnetic field of 16 T. Fig 3.2-a shows a recognizable downturn for the dopings of $p = 0.12, 0.15$. Although, for $p = 0.17$

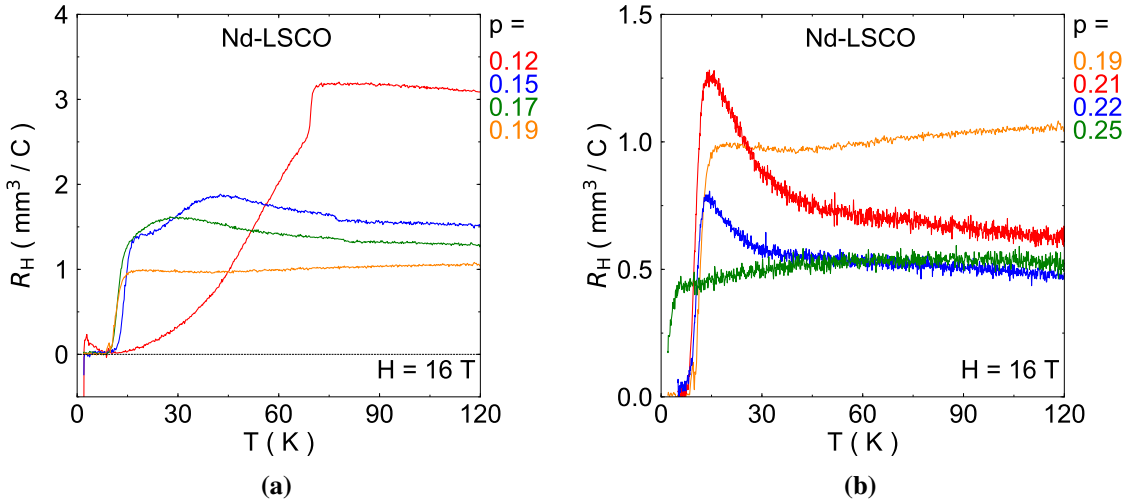

Figure 3.2 Temperature dependence of Hall effect in Nd-LSCO. a) for p = 0.12, 0.15, 0.17 and 0.19, b) and for p = 0.19, 0.21, 0.22 and 0.25. The data for p = 0.21 and 0.22 is obtained from [43]. The signal to noise ratio is different as the applied current was not the same or the thickness of the samples were different (in thinner samples the signal must be larger).

and 0.19, the downturn is located close to the onset of T_c [1]. Therefore, to check if there is a downturn corresponding to the CDW, not superconductivity, one must study the normal state by suppressing the superconductivity. If the downturn continues to drop even in the normal state, that is a genuine signature of CDW. Likewise, in the normal state, the pseudogap phase is visible and easier to trace compared with its signature at higher temperatures [2]. Fig 3.2-b shows the renowned upturn in R_H vs T associated with the pseudogap at $p = 0.21, 0.22$. At p = 0.25, where p > p*, there is no pseudogap and consequently, there is no upturn. In both of the Figures 3.2-a and b, the value of R_H at high temperatures keeps decreasing by increasing the doping. For p = 0.19, it is hard to tell if there is going to be an upturn or a downturn in the low-temperature normal state. From figure 3.2-a and b we can understand that between p = 0.15 and p = 0.21 a change has happened: the downturn at p = 0.15 disappears and an upturn emerges at p = 0.21.

To check that the Hall effect and resistivity are being measured in the normal state and to determine the H_{c2}, field sweeps of the resistivity and Hall effect are useful to verify that. We perform this kind of field sweep experiments on all of the dopings, but for the interest of brevity, we only present the data on Nd-LSCO p = 0.17 and 0.19 here. In Fig 3.3, the

[1] Hall coefficient goes to zero in the superconducting state and decreases where the superconducting fluctuations appear. As a reminder from Chapter one: the signature of CDW is a drop in Hall coefficient, and in temperatures lower than T_{CDW}, the Hall coefficient could be either positive or negative, depending on the details of the Fermi surface, even though there are small electron pockets due to the Fermi surface reconstruction by CDW.

[2] The most explicit signatures of the pseudogap phase appear on the resistivity and Nernst effect.

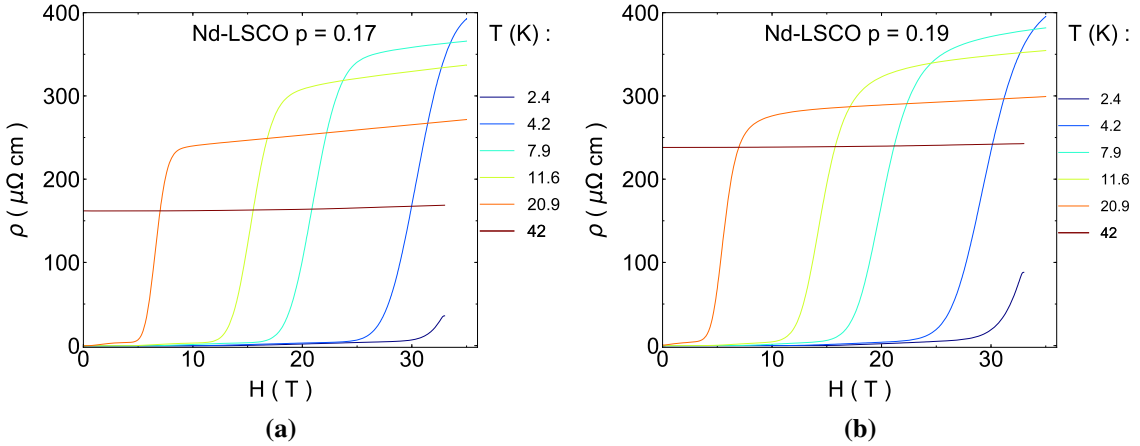

Figure 3.3 Field dependence of resistivity in Nd-LSCO, at different temperatures, for a) p = 0.17 . b) p = 0.19. The data have been taken at Nijmegen in Dec 2017.

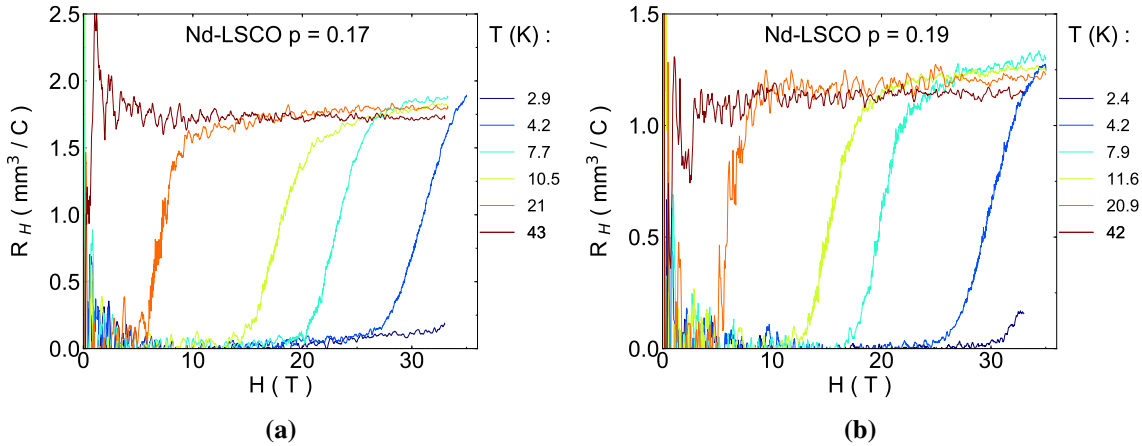

Figure 3.4 Field dependence (field sweeps) of Hall coefficient in Nd-LSCO, at different temperatures for dopings of a) p = 0.17 , b) p = 0.19. The data have been taken at Nijmegen in Dec 2017.

normal state has been reached by the application of the magnetic field (the experiment was performed at Nijmegen on Dec 2017). For instance, for the Nd-LSCO at p = 0.17 (fig 3.3-a) at T = 7.9K, we access the normal state at H $>$ 25T. At lower temperatures we need higher fields to reach the normal state as in Nd-LSCO p = 0.17 (fig 3.3-a), the normal state at T = 4.2K is inaccessible even at 33 T. Likewise, the magnetic field dependence of the Hall coefficient can provide information on H_{c2} (Figure 3.4).

Figure 3.5 shows the resistivity of Nd-LSCO p = 0.17 and 0.19 at H = 16 and 33T. The circles are the field sweep cuts obtained from Figure 3.5. The anomaly at T $\approx$ 80K is due to the LTT to LTO structural transition that is explained in Chapter one.

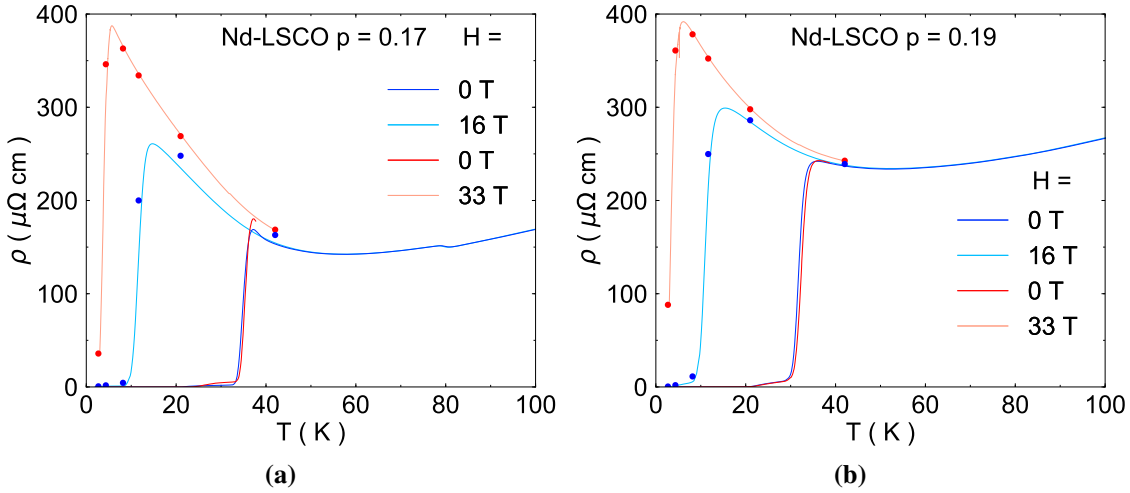

Figure 3.5 Normal state resistivity as a function of temperature for Nd-LSCO at a) p = 0.17, b) p = 0.19. Blue and red data have been taken at Sherbrooke and Nijmegen respectively. Both blue and red circles are the field dependence of the resistivity at different temperatures as shown in 3.4 for Nijmegen data. The slight difference between the data is due to the different instrumentation in different labs.

We look at the temperature dependence of the Hall coefficient of Nd-LSCO p = 0.17 and 0.19 again, but this time, in higher magnetic fields, to be able to push the drop of the superconductivity to lower temperatures Figure 3.6. Figure 3.6-a shows R_H vs T for Nd-LSCO p = 0.17 at H = 16 and 33T; dots are from the field sweep cuts at certain temperatures (obtained from Figure 3.4). In the absence of the superconductivity, the onset of the CDW downturn at p = 0.17 is clearly at T $\approx$ 30K. Albeit this downturn is less dramatic than that of Nd-LSCO p = 0.12 and 0.15 [3].

In Figure 3.6-b, it is impossible to see a downturn in R_H vs T for Nd-LSCO p = 0.19 at H = 33T down to T $\approx$ 5K, meaning that there is no CDW in this doping (at least down to T = 5K). Furthermore, at H = 33T in Nd-LSCO p = 0.19, the upturn of the pseudogap is recovered. One should notice that the CDW does not have any signature in resistivity as in Figure 3.5-a. A continuous upturn is associated with the pseudogap down to T = 5K, even though the CDW onset is located at T $\approx$ 30K, this suggests that CDW is located inside the pseudogap.

In Figure 3.6-c, only the signature of the pseudogap—an upturn in R_H vs. T— is visible

[3]One might associate the depth of the CDW downturn to the intensity of CDW and concludes that the intensity of the CDW is decreased from p = 0.12 to 0.17. But, the strength of CDW is not a well-established quantitative physical parameter and Hall effect is very sensitive to the details of the Fermi surface and contaminations from c-axis or a considerable amount of impurity and inhomogeneity. But, maybe based on the effect of CDW on superconductivity (the dip on SC dome is deepest at p = 0.12) and intensity of x-ray signal (to be determined), one can conclude that CDW is at its highest intensity at p = 0.12.

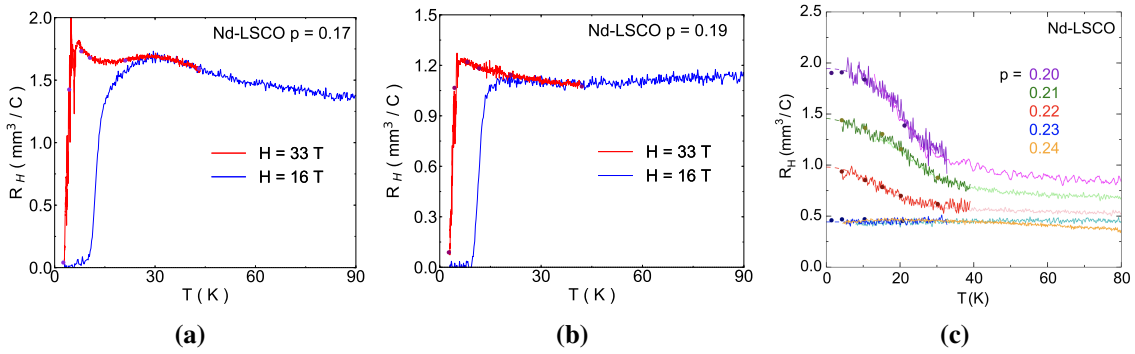

Figure 3.6 Normal state of Hall coefficient as a function of temperature in at 16T (blue) and 33T(red) in Nd-LSCO at a) p = 0.17, b) p = 0.19, c) p = 0.20 - 0.24. Circles are magnetic field cuts of field sweeps at 33T. Panel c is obtained from the Ref [43].

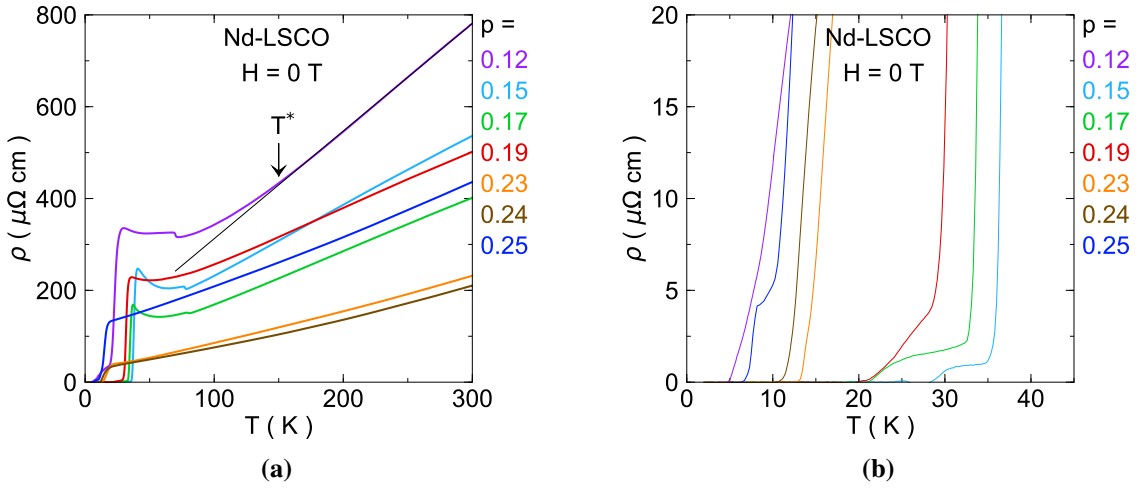

Figure 3.7 a)Temperature dependence of resistivity as in zero magnetic field for a range of doping in Nd-LSCO. Notice the upturn below p = 0.23 that is the signature of pseudogap b) An enlargement near T_c.

(no trace of any drop of R_H). At p* and above, there is no pseudogap that changes the number of carriers, so there is a constant Hall coefficient in temperature for the dopings of p $\geq$ p* = 0.23.

Figure 3.7 shows the resistivity vs temperature for several dopings at zero magnetic field. There is an upturn due to the pseudogap below T* for all the samples except for p = 0.24 and 0.25. By comparing the Figure 3.2 and 3.7-a one can infer that $T_{CDW} \leq$ T*. Figure 3.7-b shows different values of T_c for different dopings.

We now move onto a closer inspection of the temperature dependence of the Hall coefficient at low temperature. In Figure 3.6-a a local minimum is observable at T = 15K

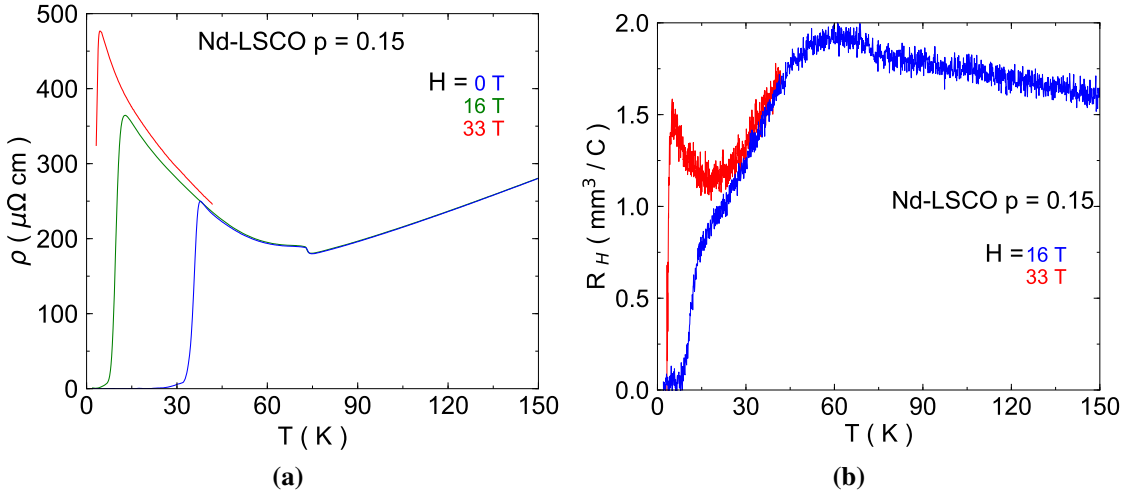

Figure 3.8 Temperature dependence of a) resistivity and b) Hall effect in Nd-LSCO p = 0.15 at H = 16T and H = 33T.

for Nd-LSCO p = 0.17 and below that a mysterious upturn appears. This upturn is not only observable at this doping, but also at p = 0.15. In Figure 3.8-a, resistivity is plotted vs temperature for Nd-LSCO p = 0.15, in which no anomaly could be observed (except one for the structural transition), while in Fig 3.8-b, a dip appears in R_H vs T below the T_{CDW} and an upturn appears below the local minimum. Three different scenarios may explain this upturn : 1) it could be due to the geometry of the Fermi surface; 2) the presence of multiple bands at Fermi level [83] and 3) a Fermi surface reconstruction by SDW. When CDW reconstructs the Fermi surface into electron-pockets [84], different curvature of this pocket can change the balance of electron or hole carriers. In the multi-band scenario, we expect to have both electron and hole-pockets and the balance between the two can affect the temperature dependence of R_H. Lastly, this upturn could be due to a second Fermi surface reconstruction caused by SDW; Figure 3.11-b shows that the onset of SDW is located close to T_{CDW}. The signature of the SDW in hole-doped cuprates is not precisely known in the transport probes, but as SDW appears at low dopings near the AFM phase (as the hole concentration—doping—increases and the AFM phase ends, the SDW phase is among one of the phases that appears), it might contain small hole-pockets that gives a positive Hall coefficient as a function of temperature. This would suggest that the origin of the SDW and the pseudogap are related.

Figure 3.9-a shows the doping dependence of the Hall coefficient. At high temperatures, above the onset of CDW order, the magnitude of R_H is decreasing by increasing the hole doping. By increasing the doping, more holes are added to the system which results in having more carriers (R_H and carrier density, n, are inversely proportional).

By tracking the evolution of the Hall coefficient at different dopings and observing a sudden change in its value we can determine the boundaries of each phase and identify

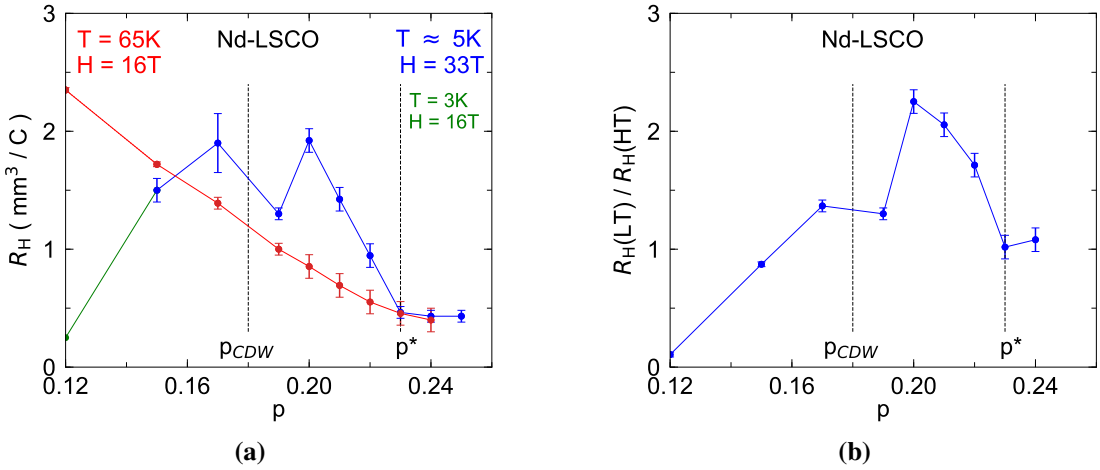

Figure 3.9 a) Doping dependence of Hall coefficient in Nd-LSCO at temperatures and fields as indicated. b) Ratio of low and high temperature Hall coefficient are denoted by R_H(LT) and R_H(HT) respectively. R_H(LT) are the same data of blue and green curve on the left and R_H(HT) are the same data as the red curve. The data at 16T are obtained from Fig3.2. For dopings above 0.19, both the low and high temperature data are obtained from Ref[43].

the parts of the phase diagram where a phase competition happens. At low temperatures and in high magnetic fields three regimes are observable. 1) At p $>$ 0.23, R_H is small (an indication of high carrier density). 2) By decreasing the doping below p* = 0.23, R_H increases abruptly. 3) At dopings below p_{CDW}, R_H drops to lower values. The same three regimes are observable in Figure 3.9-b, where it plots R_H at low temperatures over R_H at high temperatures. The same behaviour for doping dependence of S/T was also observed in Nd-LSCO (Figure 3.11-a).

3.1.1 End point of the CDW phase

Signature of CDW is also recognizable by the Seebeck effect as discussed in Chapter one (Fig 1.8-b), namely: a drop in S/T vs T.

We measured the Seebeck coefficient, S, in multiple dopings of Nd-LSCO in magnetic fields of 16 and 33T and plot S/T vs T in Figure 3.10-a. For doping of p = 0.12, 0.15 and 0.17, S/T vs T shows a downturn that goes towards negative values which means that a Fermi surface reconstruction happens that makes the electron-pockets and they contribute to a negative S/T signal which decreases the positive signal. The onset of this drop is associated with the onset of CDW (T_{CDW}) [51]. We observe that the T_{CDW} is decreasing by increasing the doping. It should be mentioned that at p = 0.12, there is a structural transition that happens right at the T_{CDW}, which is why there is an abrupt drop at 70K in this sample and below this drop, the S/T keeps decreasing by decreasing the temperature like the other

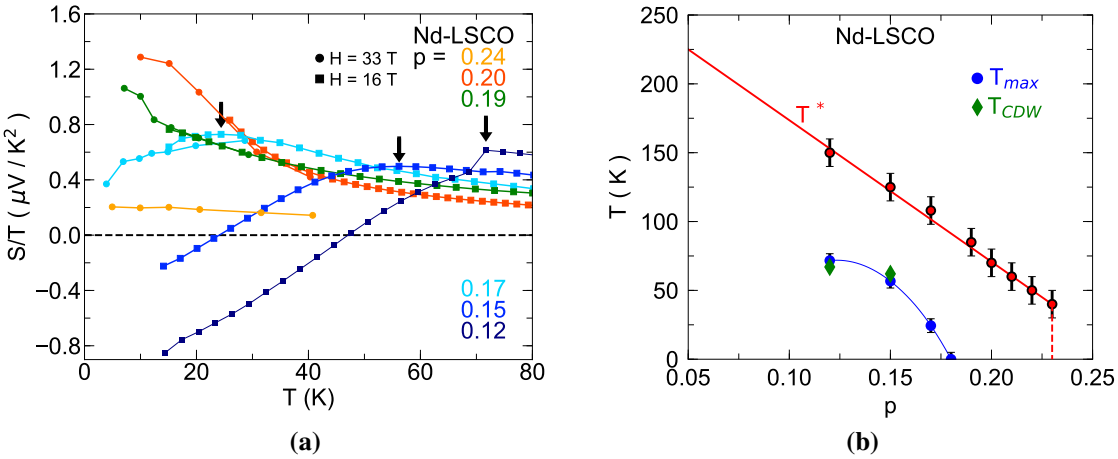

Figure 3.10 a)Temperature dependence of Seebeck coefficient over temperature for a range of Nd-LSCO dopings. Arrows are showing the T_{max}. The high field data on Nd-LSCO p = 0.17 and 0.19 were taken at Grenoble on Oct 2017 and for p = 0.20 and 0.24, the experiment was performed at Nijmegen on Dec 2016. b) T_{max} (blue) is plotted for different dopings. T_{max} is the maximum of S/T vs T in part a. Diamonds (green) are the T_{CDW} measured by XRD [13].

dopings of 0.15 and 0.17. At p = 0.19 and high magnetic fields no downturn is observed, which means that the CDW order is not present at this doping anymore. Instead, at p = 0.19 and 0.20, S/T vs T shows an upturn that appears because of the pseudogap. Finally at p $>$ p*, no upturn or downturn is visible.

In Fig 3.10-b, the blue circles are the T_{max} in Fig 3.10-a (error bars are standard deviations of field sweeps) and the green diamonds are the T_{CDW} that is measured by XRD[13], which are close to one another. At p = 0.17, no XRD data are available, but if we continue to track the T_{max}, we realize that the CDW phase ends somewhere between p = 0.17 and 0.19. This result implies that the CDW and the pseudogap phases, do not have the same endpoint, as concluded earlier for YBCO (from R_H(T) [85]) and LSCO (from S(T) [52]). This challenges some theories which claim that the presence of the pseudogap phase in cuprates is due to the CDW [35].

In Fig 3.11-b, the full phase diagram of Nd-LSCO is shown. The region with the blue shading is where the CDW phase is located. The blue circles are T_{max} in S/T vs T, which are in good agreement with T_{CDW} that is obtained by XRD and Hall effect (as shown by green diamonds in Fig 3.10). The green and red shaded region are where SDW (the data were obtained by the neutron spectroscopy experiments [11]) and superconductivity (the data come from the VSM measurements and the T_c is where the bulk magnetic moment starts to go to negative values) are located respectively. The pseudogap is located below the red line and red circles on that line come from the resistivity measurements and are located where the resistivity deviates from linearity.

3.1.2 Doping dependence of Seebeck Effect: Pseudogap and CDW signatures

In Fig 3.10-a it is shown that the pseudogap manifests itself in an upturn in S/T vs T, e.g., at p = 0.20. In order to trace it more clearly, we plot S/T as a function of doping for several samples in Fig 3.11-a. Here we take the value of S/T at the lowest accessible temperatures in the normal state and plot them as a function of doping (some of the data are obtained from the Ph.D. thesis of Clement Collignon [86]).

Three different regimes can be observed in Fig 3.10-a. 1) At p = 0.24 and 0.25, S/T is low and positive. 2) By increasing the doping and entering the pseudogap, S/T $>$ 0 and it starts to increase abruptly (this is another signature of pseudogap's critical point). 3) At p $<$ p_{CDW}, S/T decreases by decreasing the doping and it becomes negative eventually.

It is observed before that close to the quantum critical point (QCP), S/T has a logarithmic behaviour [87, 51]. Fig 3.12-a shows the S/T vs T for various dopings. In low temperatures at p = 0.12, 0.15 and 0.17 there is no logarithmic behaviour, but at p = 0.19, there seems to be a logarithmic behaviour down to low temperatures. In order to check that, we compare it to Nd-LSCO and Eu-LSCO at p = 0.24, where the logarithmic regime is seen. Fig 3.12-b shows that S/T for p = 0.24 does not have a full logarithmic regime compared to p = 0.24 dopings. At p = 0.20 the logarithmic behaviour is not visible either. In low and high dopings, one can distinguish two separate non-logarithmic and logarithmic regimes respectively. In the intermediate doping region i.e. 0.19, the temperature dependence of S/T shows a logarithmic behaviour. That is maybe because there is a crossover between these two regimes (the pseudogap and CDW phases), but in reality, this does not do much with the quantum critical point (even though p = 0.19 is located right after the p_{CDW} critical point). In any case, at p = 0.24—which is much closer to the QCP of pseudogap p* = 0.23— the signatures of the QCP on S/T vs p and vs T are clear.

3.1.3 Effect of pressure on CDW in Nd-LSCO probed by electrical transport

Our approach to tune the CDW order is to apply pressure. After all, the CDW phase is related to the distribution of charge in the lattice. So, pressure could reshape the distribution of charges to some extent by affecting the lattice constants. But the relation between the CDW phase and a crystal lattice is not well understood yet (certain pressures may or may not have considerable effects on CDW).

In YBCO, with 2GPa of pressure, one can suppress CDW partially and recover the superconducting dome—that is reshaped with by a dip caused by CDW— to some extent [32]; however, to fully recover the superconducting dome, pressures on the order of 15GPa

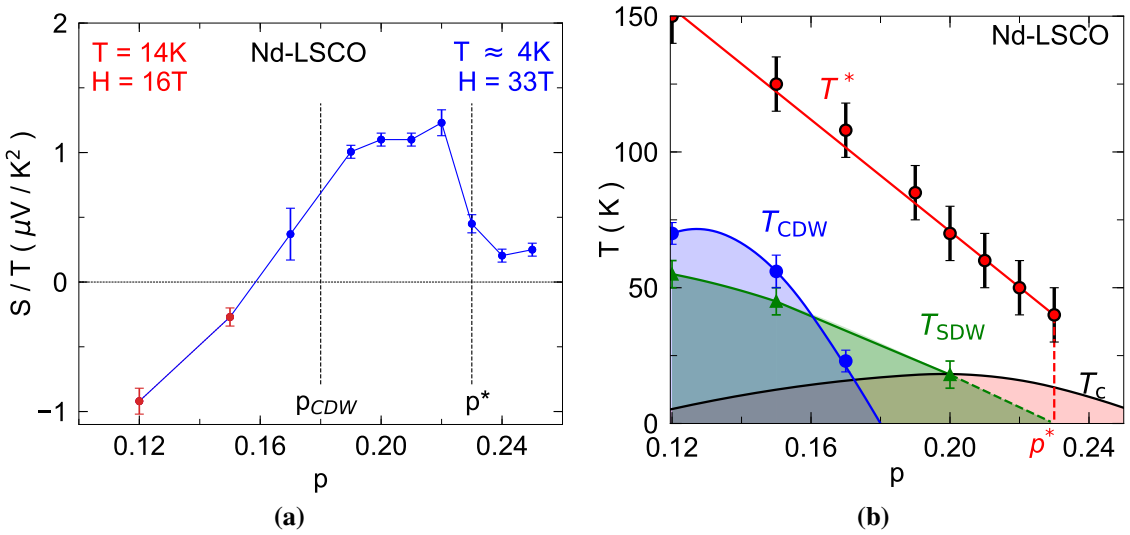

Figure 3.11 a)Seebeck coefficient over temperature as a function of doping at low temperature and high fields. The data at dopings above 0.19 are obtained from the Ph.D. thesis of Clement Collignon [86]. b) Full phase diagram of Nd-LSCO. The points for T_{SDW} are from [11].

are needed [88]. In YBCO, there is also the effect of pressure-induced doping to consider and on the other hand, there are oxygen chains in YBCO which makes it complicated to have a clear picture of the suppression mechanism of CDW. For these reasons, we turned to Nd-LSCO for the study of the suppression of CDW with hydrostatic pressure.

First, we apply pressure on Nd-LSCO at the dopings of 0.12 and 0.15. As it was mentioned before, the signature of CDW is a downturn in the Hall effect, and thus, if CDW could be suppressed by pressure, this downturn should disappear.

Fig 3.13 shows the evolution of the Hall effect vs temperature for Nd-LSCO at p = 0.12 and 0.15 at different pressures normalized at 120K. In Fig 3.13-a there is an abrupt drop due to the structural transition ,T_{str}, and T_{CDW} is located right below that temperature. By increasing the pressure, the R_H becomes more negative at low temperatures. This implies that the curvature of the Fermi surface is changed and the balance between the electron and hole carriers is changed in favor of the electrons. The other effect of pressure is to move the T_{str} to higher temperatures. Pressure makes the drop less steep and in p = 0.12, it smooths the structural transition which is around 70K [65]. Thus, we do see a small effect of pressure in the Hall effect. Moreover, the onset of the structural transition temperature (T_{str}) in this sample is intertwined with the T_{CDW}, so it is difficult to classify the effect of pressure on CDW and T_{str}.

In Fig 3.13-b, we show the data for p = 0.15. The difference is that we need higher magnetic fields to fully suppress the superconductivity and at low temperatures, R_H(T) does not become negative. Plus, the structural transition does not show an abrupt drop in R_H(T)

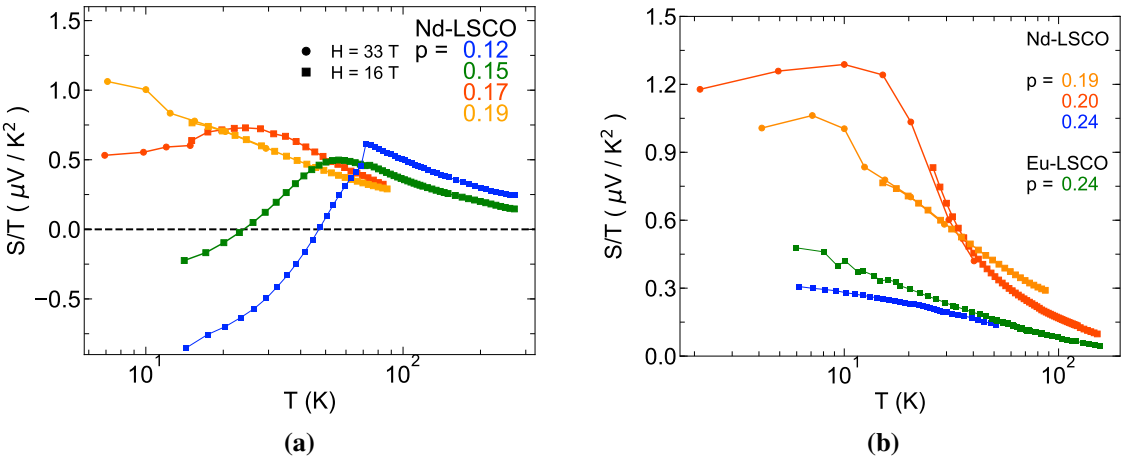

Figure 3.12 a) S over T vs log(T) for Several dopings Nd-LSCO. b) S/T vs log(T) for Eu-LSCO at p =0.24 and Nd-LSCO at p = 0.19,0.20 and 0.24. Circles and squares are the data that obtained at 33 and 16T respectively and for Eu-LSCO and Nd-LSCO at p = 0.24 the data are obtained at 15T and taken from [51] and [87] respectively.

and it is located at higher temperatures. The onset of the drop in R_H(T) is moving slightly to lower temperatures as for p = 0.12, it seems to move slightly towards higher dopings (due to the effect of the structural transition) [4].

Pressure does not entirely suppress CDW in neither of these dopings as the drop of Hall coefficient vs T is still present (the effect is small and is within the error bars). It seems that the applied pressure is not enough to suppress the CDW order [5].

The temperature dependence of the Hall effect is also studied in another Nd-LSCO p = 0.12 sample under pressure. We have a higher signal to noise ratio as we could apply higher currents under pressure [6]. There is also a difference between this new sample and the other one (Fig 3.13-a). The new sample has less than 0.1% contamination from c-axis (it was cut more precisely) and the value of R_H at high temperatures (100K) is higher compared with the other sample.

Fig 3.14, shows the temperature dependence of the Hall coefficient in different magnetic fields and applied pressures, consistent with Fig3.13. This field dependency of the Hall coefficient might suggest that the magnetic field can tune a phase that makes the electron or

[4] One hypothesis is that by further increasing the pressure for p = 0.12, eventually the structural transition disappears and by increasing the pressure even more, the onset of the drop in Hall effect moves to lower temperatures finally, but this hypothesis must be tested first.

[5] Based on the evolution of the Hall effect towards suppression of its downturn at 2GPa, one can guess that maybe we require 4-5 times of this pressure to fully suppress this downturn.

[6] We were not aware of that in our previous experiments and we were afraid that high current might break the wires on the samples, which is the case in vacuum not under pressure.

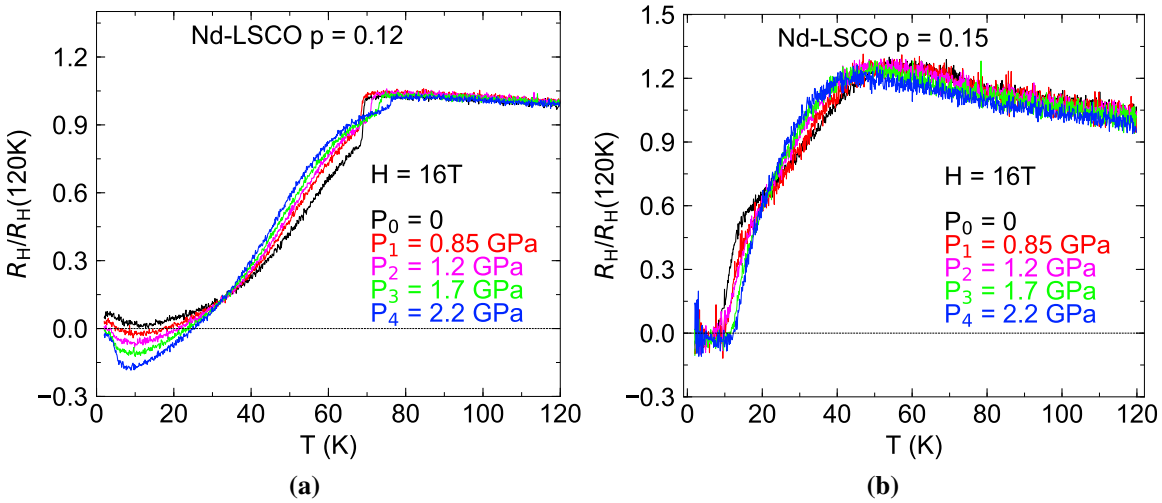

Figure 3.13 Temperature dependence of Hall effect normalized at 120K a) p = 0.12 b)p = 0.15. The structural transition from LTT-LTO is more pronounced in p = 0.12. And it is getting faded as pressure increases.

hole pockets in the Fermi surface. Further studies must be carried out to reveal the nature of the phase that is being tuned by the field.

In summary, pressure has two effects in R_H(T). At p = 0.15, as the signal does not go to negative values at low temperatures, we cannot judge about the CDW strength there. By looking at the T_{max}, one can see that the onset of CDW moves to lower temperatures by about 5K. But this change in T_{max} is small (this change in T_{max} is within the error bars and a bit larger than the noise level on this experiment). So, one might argue that pressure weakens CDW at 0.15. At p = 0.12, the opposite happens at T_{max}, and it moves to higher temperatures (but this could be the artifact of the structural transition which is located at T_{CDW}). More importantly, at low temperatures, R_H(T) becomes more negative at higher pressures. So, this suggests that pressure strengthens CDW at this doping.

Fig 3.16 shows the resistivity as a function of temperature in Nd-LSCO p = 0.12 (same sample as in Fig 3.14). It shows that 2.2GPa of pressure moves T_c from 4.1K to 15K. It should be noted that the signature of the structural transition in resistivity becomes smoother and moves to higher temperatures.

We also used the Seebeck effect to assess the effect of pressure on the CDW phase. Fig 3.17 shows Seebeck coefficient over temperature as a function of temperature in Nd-LSCO p = 0.12 at ambient pressure, 0.8GPa and 2.2GPa. Pressure moves the onset of structural transition to higher temperatures (as seen in Hall effect), which happens to be the T_{max} here. So, it conceals the onset of the CDW too. Therefore, it is hard to conclude that the onset of the CDW itself is displaced. However, unlike the Hall coefficient for this sample, the

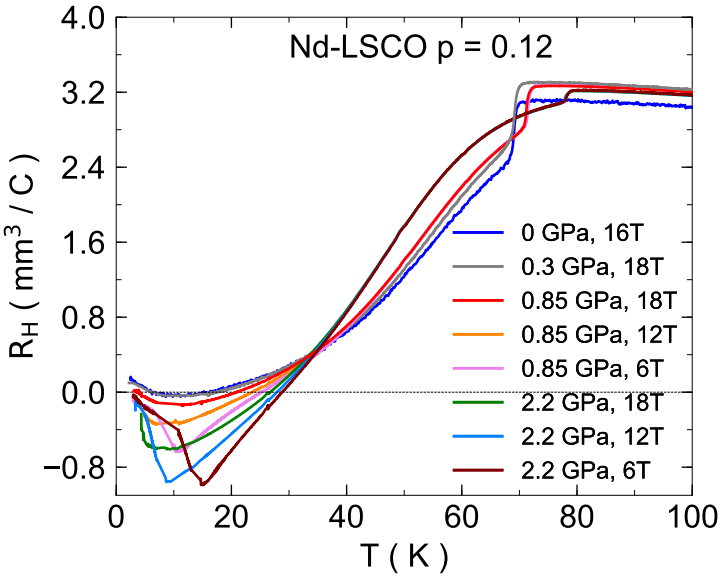

Figure 3.14 Temperature dependence of Hall coefficient in Nd-LSCO p = 0.12. The applied magnetic field and pressure are different.

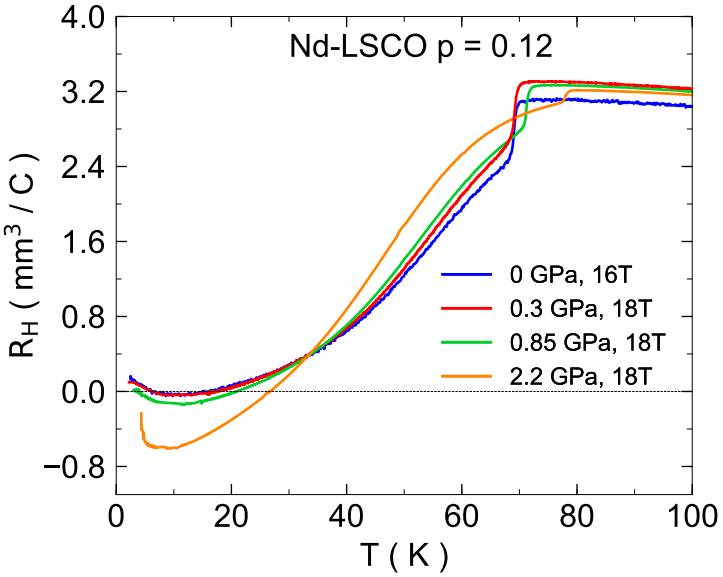

Figure 3.15 Temperature dependence of Hall coefficient in Nd-LSCO p = 0.12 at several pressures and 16 and 18T.

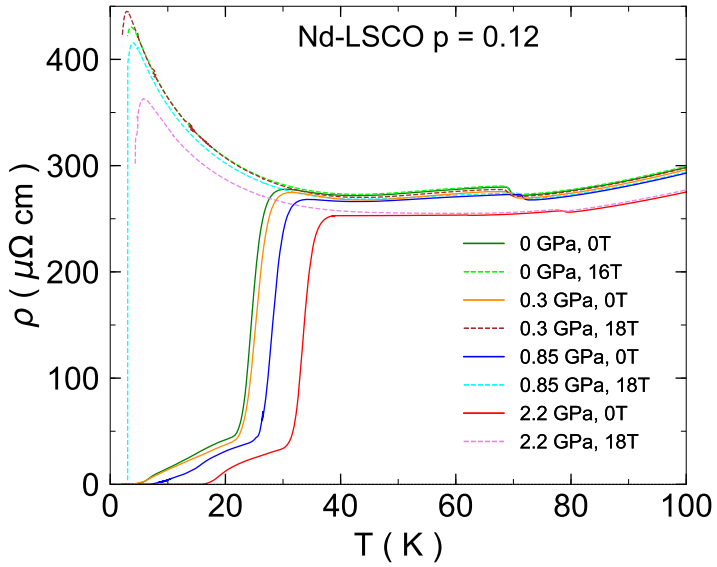

Figure 3.16 Temperature dependence of Hall coefficient in Nd-LSCO at p = 0.12. The applied magnetic fields and pressures are different.

Seebeck coefficient over T vs T goes to negative values. At P = 0.85 GPa, the S/T becomes negative below 46K, while at P = 2.2 GPa it becomes negative below 41K. This is in a good quantitative agreement with the change in the onset of the T_{max} in the Nd-LSCO p = 0.15 at 1.7GPa which is also 5K [7]. Fig 3.19-a shows the effect of pressure on T_{str} obtained by both Seebeck and Hall effect and also compared it with T_0 (where S/T vs T changes sign). Fig 3.19-b shows the effect of pressure on T_c in the same sample at the same pressure points. We conclude the pressure effect on different characteristic temperatures as follow:

$$\frac{dT_{str}}{dP} = 5[\frac{K}{GPa}] \quad , \frac{dT_0}{dP} = -4[\frac{K}{GPa}] \quad , \quad \frac{dT_c}{dP} = 4[\frac{K}{GPa}] \tag{3.1}$$

In summary, by increasing pressure: S/T becomes less negative and it goes to negative values at lower temperatures. This suggests that the CDW is weakened by pressure. This is opposite to the Hall effect results at this doping (R_H was more negative in higher pressures at low temperatures). The fact that T_0 moves down by the same amount of magnitude that T_c increases, suggests that the superconductivity and CDW are in direct competition.

It is difficult to say what really happens to the Fermi surface at this doping. Therefore, we revisited the Hall effect again (on another sample) by improving the signal to noise ratio. There might be hole pockets at this doping as a result of the Fermi surface reconstruction as stated before. Fig 3.20-b shows R_H vs temperature for Nd-LSCO, LSCO (single crystal) and LSCO thin film at p = 0.12 in different magnetic fields. All of these systems have

[7] We have ±0.2GPa of imprecision for the pressure inside the cell and its nominal value

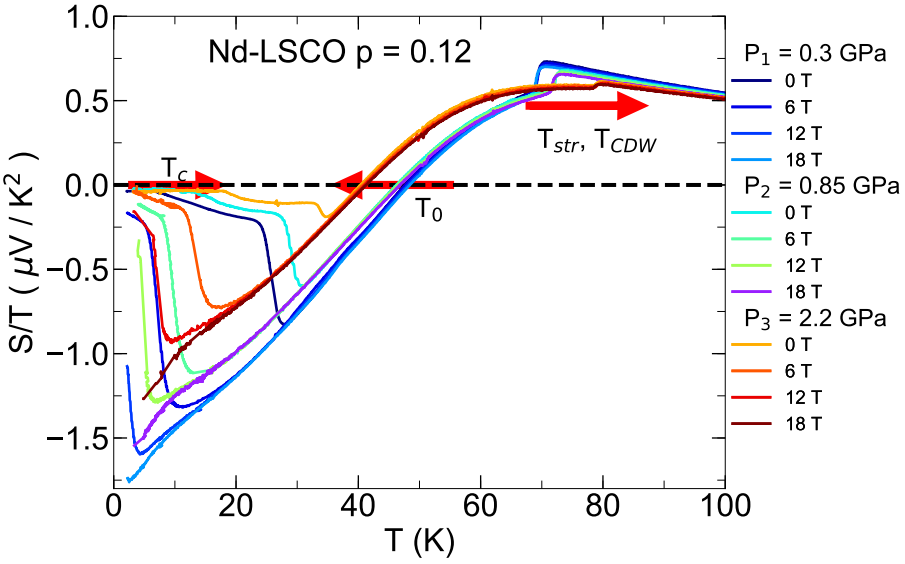

Figure 3.17 Temperature dependence of Seebeck coefficient over temperature in Nd-LSCO at p = 0.12. The applied magnetic field and pressure are different.

relatively similar Fermi surfaces, but the difference between their R_H(T) at low temperatures is significant. A way to explain this difference is by assuming that there might be hole and electron pockets at the Fermi surface that change the balance of Hall coefficient. These hole pockets are still present in YBCO, but as the mobility of the electrons ($\mu \propto \tau/m^*$) is bigger at the electron pockets or the parts of the Fermi surface with a negative curvature, the hole pockets (or the parts of the Fermi surface with a positive curvature) cannot affect the R_H signal significantly, thus R_H becomes much more negative compared with LSCO for instance. The mobility effect can also be studied in a very similar system. In Fig 3.20-a, one LSCO single crystal is compared with an LSCO thin film that has the same doping. As the crystal structure of the single crystal has a higher quality, the electrons have higher mobility thus R_H is higher in the single crystal (it should be mentioned that the quality of the crystal can also affect the scattering rate as well, but we merely focus on the mobility here.)

We also measured higher dopings of Nd-LSCO where CDW is less strong (the onset of T_{CDW} at this doping is in lower temperatures compared with p = 0.12 and 0.15 which means lower energy scale). Fig 3.21 shows the effect of pressure on the resistivity at H = 0T for Nd-LSCO p = 0.17. It is clear that pressure increases the T_c as it is the case for all the dopings of Nd-LSCO. But it does not change the doping. In order to check if the pseudogap is suppressed or not, we need to have access to the normal state. In Fig 3.22-a, temperature dependence of resistivity is shown at H = 18T. One can see that there is a clear upturn down to 1.2 GPa, but we need higher magnetic fields to check if the pseudogap is suppressed at higher pressures or not.

We measured the very same sample at higher magnetic fields and under pressure. We

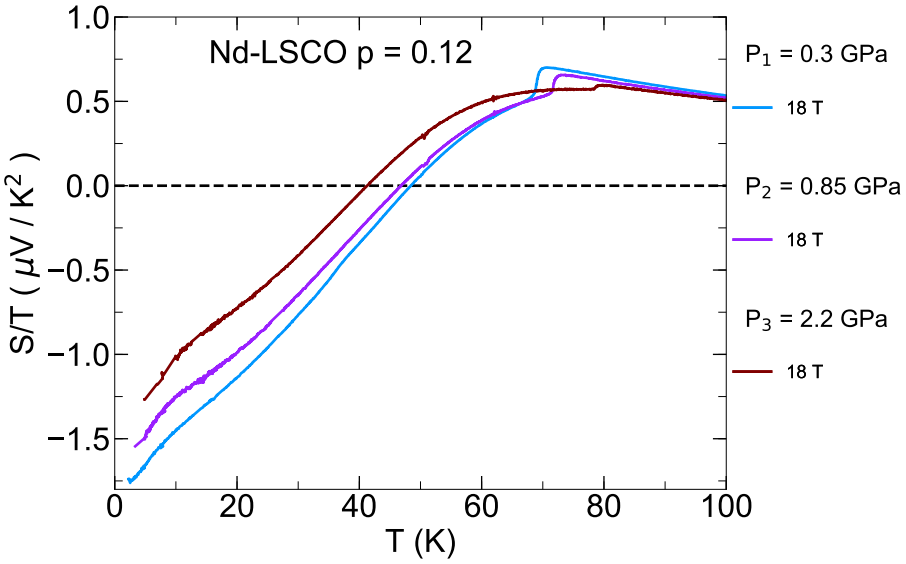

Figure 3.18 Temperature dependence of Seebeck coefficient over temperature in Nd-LSCO at p = 0.12 and H = 18T. The pressures are different as indicated. The curves at the other magnetic fields in Fig 3.17 are removed for clarity.

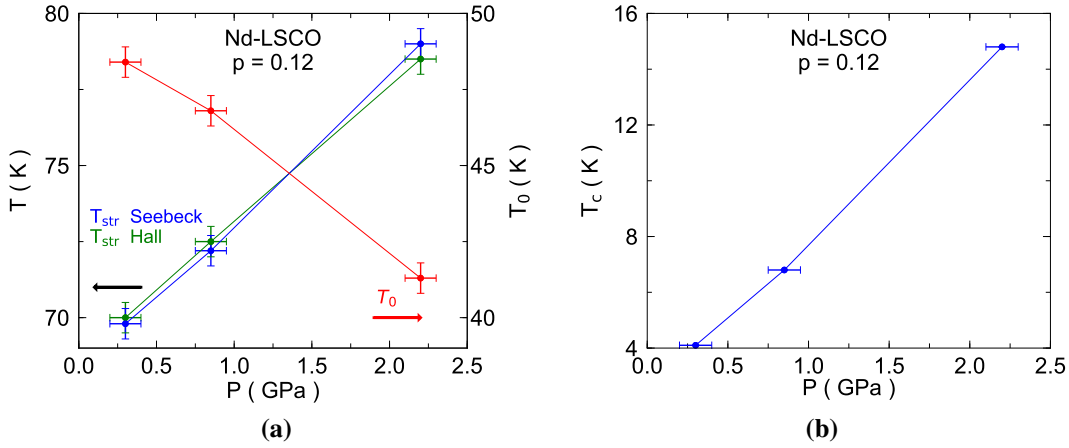

Figure 3.19 Pressure dependence of different characteristic temperatures in Nd-LSCO at p = 0.12. a) Pressure dependence of T_{str} from Seebeck (blue) and Hall effect (green) on the left axis and T_0 on the right axis. The error bars are showing the imprecision in pressure (because of the solidification of the pressure medium at low temperatures) and temperature (T_{str} has slightly different values at different magnetic fields). b) Pressure dependence of T_c.

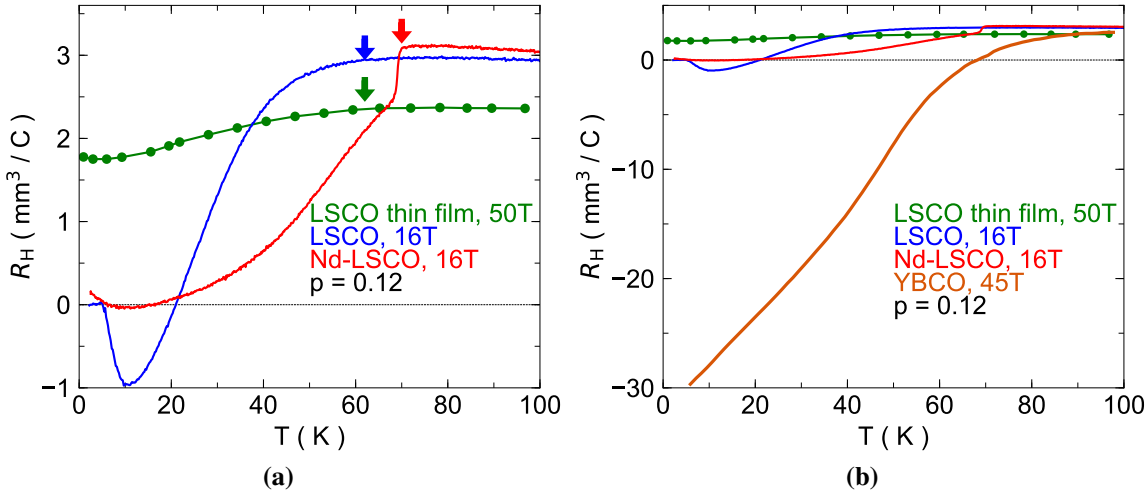

Figure 3.20 a) The temperature dependence of the R_H in single crystals of the Nd-LSCO, LSCO and the thin film of LSCO at p = 0.12. The data for the thin film were obtained from Ref [89]. Arrows mark the onset of the drop in R_H. b) Comparison of the left panel data with the R_H(T) of YBCO at p = 0.12. The YBCO data were obtained from Ref [90].

observed that the upturn recovers in the field. Fig 3.23 shows the temperature dependence of the resistivity in the high magnetic fields and compares it with the data in Fig 3.22-a.

However, we can look into the temperature dependence of Seebeck vs temperature. Fig 3.22-b shows S/T vs T for the same Nd-LSCO sample at p = 0.17. The Seebeck coefficient upturn suggests that there must be a pseudogap phase at this doping and in the highest pressure in contrast to resistivity, one can still see the upturn. However, T_{max} —local maximum in S/T vs T— is only visible in low pressures in the temperature range, where we had access to the normal state. So, we need to have access to higher magnetic fields to verify if T_{max} is fully suppressed under pressure or not. We can nonetheless look at the signature of the CDW in the Hall coefficient at this doping and investigate the pressure effect on it.

In Fig 3.24, the Hall effect measurements in temperature at three different pressures are shown and are compared to the ambient pressure data in a low and high magnetic field data. The zero pressure curves are shifted for easier comparison and clarity and because of the fact that there is an offset in our pressure data coming from the instrumentation that we use in high field facilities. In the violet curve that was obtained at H = 33T and ambient pressure, one can see the T_{CDW} and the dip in the R_H vs T. But, the other curves that are obtained in 18T and at higher pressure are very similar to the one in ambient pressure that was obtained in 16T. Again we have the same problem for detecting the T_{CDW} that was mentioned earlier in the first section of this chapter.

To delineate the pressure effect on CDW at p = 0.17, we measured the Hall effect in higher magnetic fields and under pressure. Fig 3.25 shows temperature dependence of R_H

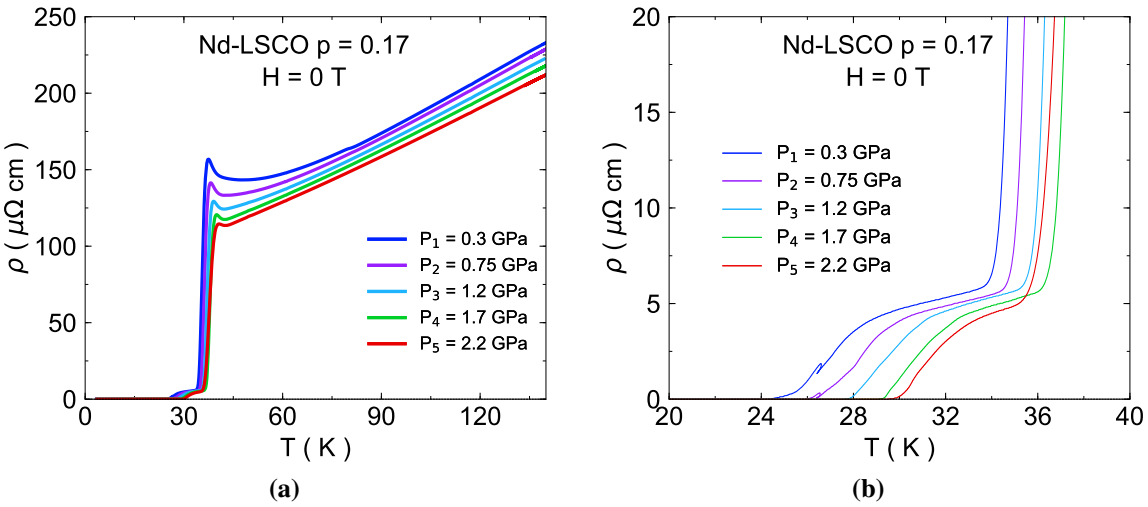

Figure 3.21 a)Temperature dependence of resistivity in Nd-LSCO p = 0.17 at H = 0T. b) An enlargement on T_c for the same figure.

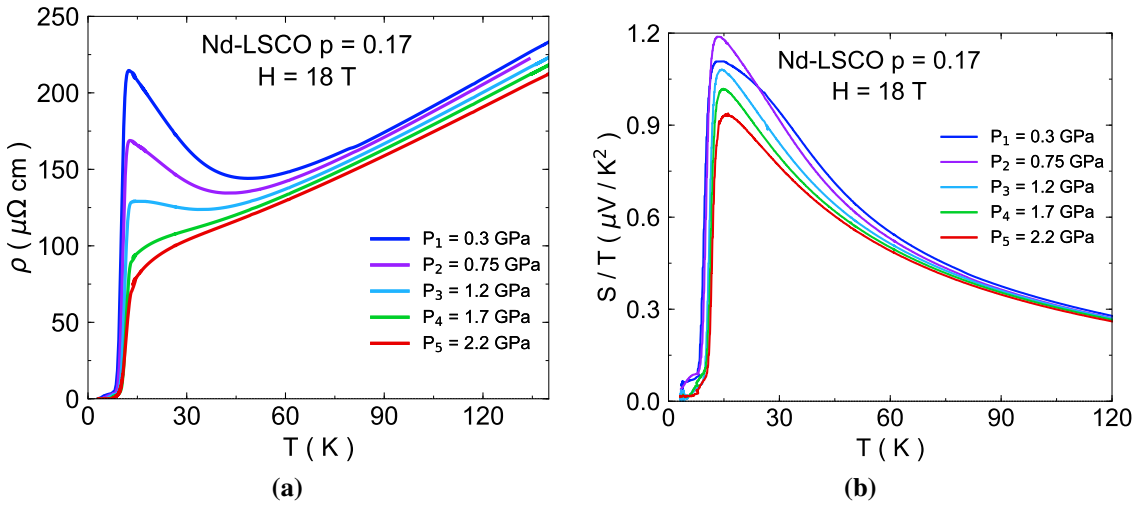

Figure 3.22 a)Temperature dependence of resistivity in Nd-LSCO p = 0.17 at H = 18T. b) S/T as a function of temperature at H = 18T in different pressures.

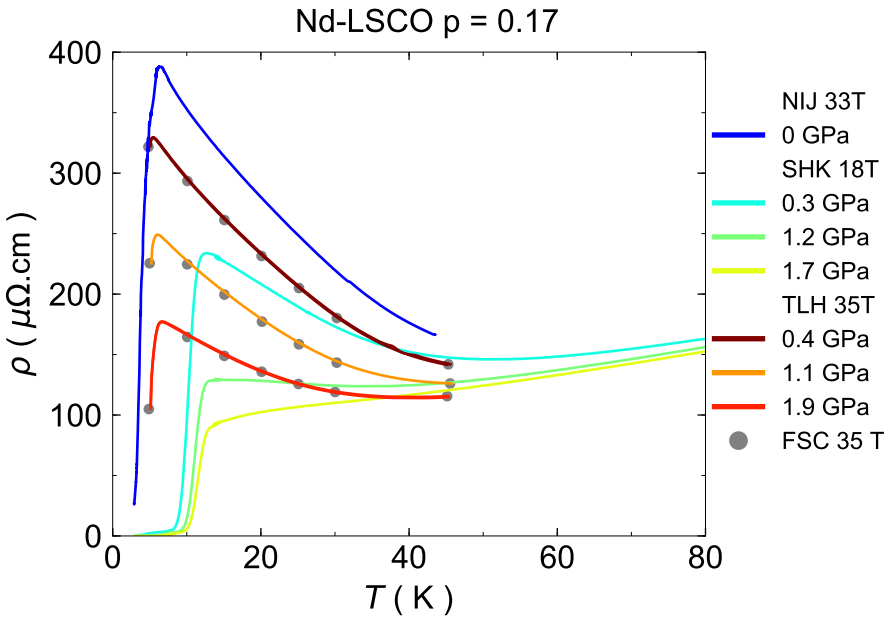

Figure 3.23 Temperature dependence of resistivity in Nd-LSCO p = 0.17. The data at 33T in Nijmegen (P = 0 GPa) is compared with Sherbrooke data at 18T and Tallahassee data at 35T at 3 similar pressures. Circles are the field sweep cuts at 35T..

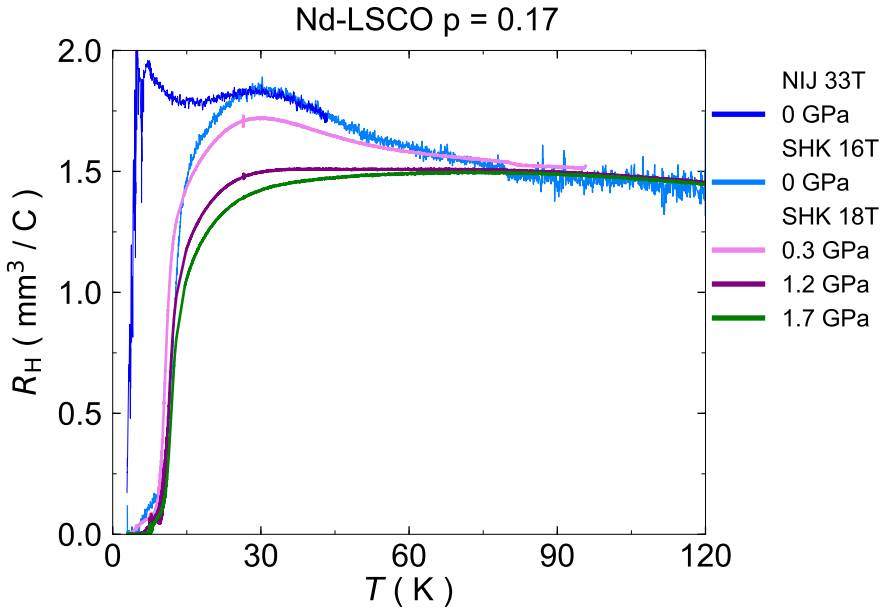

Figure 3.24 Temperature dependence of Hall coefficient in Nd-LSCO p = 0.17 at H = 16,18 and 33T in different pressures as indicated.

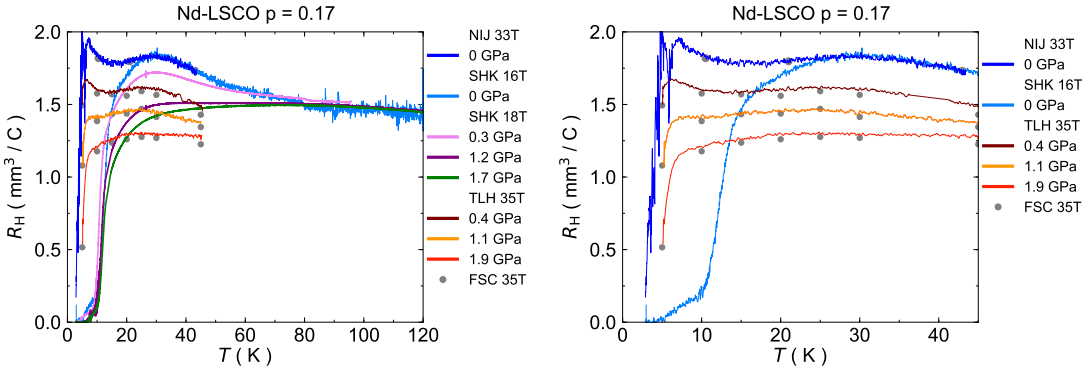

Figure 3.25 Temperature dependence of R_H vs temperature in different pressures as indicated. 33T at Nijmegen, 18T at Sherbrooke and 35T at Tallahassee were applied during the experiments. Circles are the field sweep cuts at 35T. b) A zoom in a smaller temperature range and the data at 18T are removed for simplicity.

for Nd-LSCO at p = 0.17. In low temperatures, we observe two behaviours. First, at 35T by increasing the pressure, T_{max} —the onset of drop— becomes less dramatic and at highest pressure it is suppressed. This could suggest that the CDW onset displaces below 20K or that it just disappears between 1.1 and 1.9GPa.

Secondly, the low-temperature upturn that appears at high magnetic fields shows the same behaviour as the T_{max}. It may be moved to temperatures lower than 8K, or it is fully suppressed. This has important implications for our understanding of the Fermi surface behaviour due to the different possible scenarios (that mentioned in the end point of the CDW phase Section). The main scenario is that both of the SDW and CDW are suppressed by 2GPa of pressure or they have been moved to very low temperatures. However, it we cannot be certain about the ultimate geometry of the Fermi surface.

3.2 Pseudogap

3.2.1 Pseudogap and the Fermi Surface topology

Even though the pseudogap onset (T*) of LSCO, Nd and Eu doped LSCO are the same, their critical points (p*) are different. Fig 3.26-a, shows the T vs doping phase diagram of these three different materials (most of the data comes from Ref [8]). Circles and squares mark the onset of the pseudogap in temperature with resistivity and Nernst effect measurements respectively (the two red circles at p = 0.17 and 0.19 are added from this work). The red,

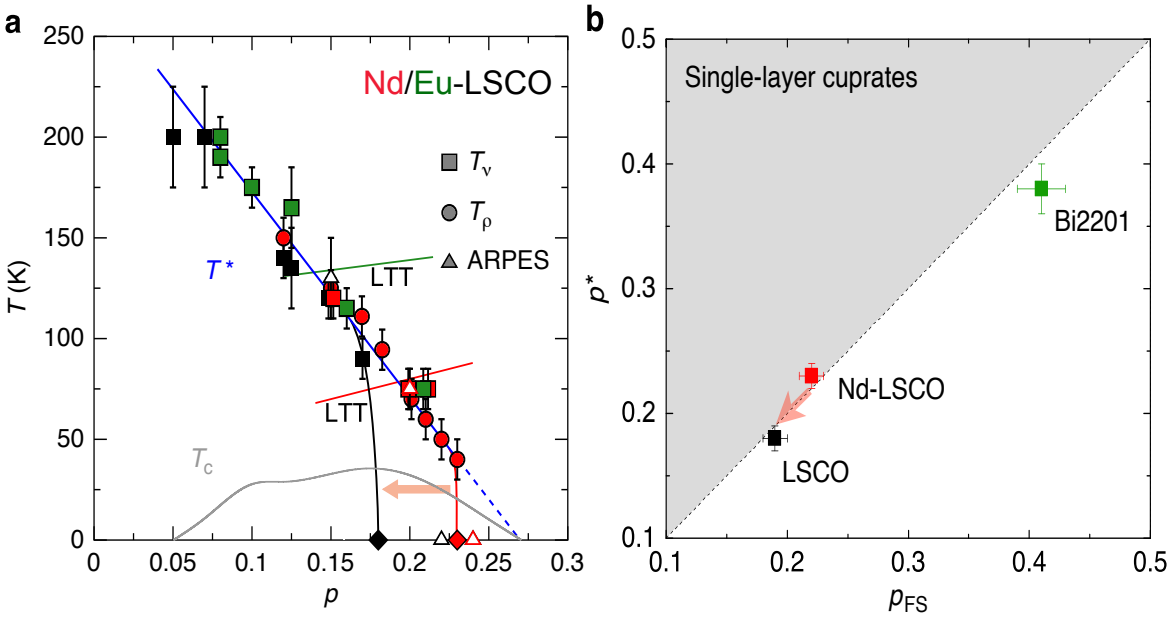

Figure 3.26 a) Phase diagram of LSCO (black), Nd-LSCO (red) and Eu-LSCO (greed) adapted from Ref [8, 91] and see the references therein. Only new red points at p = 0.17 and 0.19 are added from this study that mark the onset of the upturn in resistivity or T* in these dopings (as shown in Fig3.7-a). The oblique lines mark the low temperature tetragonal (LTT) structure of Nd-LSCO (red) [92] and Eu-LSCO (green) [93]. b) p* is plotted vs p_{FS} and shows the condition of p* $\leq$ p_{FS} is being satisfied by Nd-LSCO, LSCO and Bi 2201. The arrow in both plots shows the effect of pressure.

green and black colours correspond to Nd-LSCO, Eu-LSCO, and LSCO respectively. ARPES measurements (denoted by triangles) measure the pseudogap directly, and at p = 0.24 no gap is observed, and the gap that is observed for LSCO p = 0.15, is in good agreement with the rest of our data that are showing T*. Below the green line, the structure of Eu-LSCO is LTT and below the red one, Nd-LSCO has that structure [8]. It suggests that there is no relation between the T* and the structure of the superconductor.

Moreover, as there are disorders of Nd and Eu in the Nd-LSCO and Eu-LSCO, it implies that disorder does not affect the T* either [94]. For Nd-LSCO p*=0.23 $\pm$ 0.01 and for LSCO p*=0.18 $\pm$ 0.01[46, 95]. In these two materials p* is located on top of the p_{FS} which is the doping at which the Fermi surface undergoes a change from hole-like to electron-like as shown by ARPES in Nd-LSCO [9] or in other words, it is the doping at which the van Hove singularity in the density of states crosses the Fermi level.

Fig3.26-b shows the constraint of p* which is p* $\leq$ p_{FS} p_{FS} for three single layered cuprates (Bi-2201, Nd-LSCO and LSCO). By applying pressure below and above p*, we study its effect on these two points individually and with respect to one another. The pink arrow in Fig3.26-a and b shows the pressure effect on Nd-LSCO that is explained in details

[8] Low temperature tetragonal (LTT) to low temperature orthorhombic (LTO) transition line is displayed in Fig 3.26-a via that lines that are mentioned in the main text

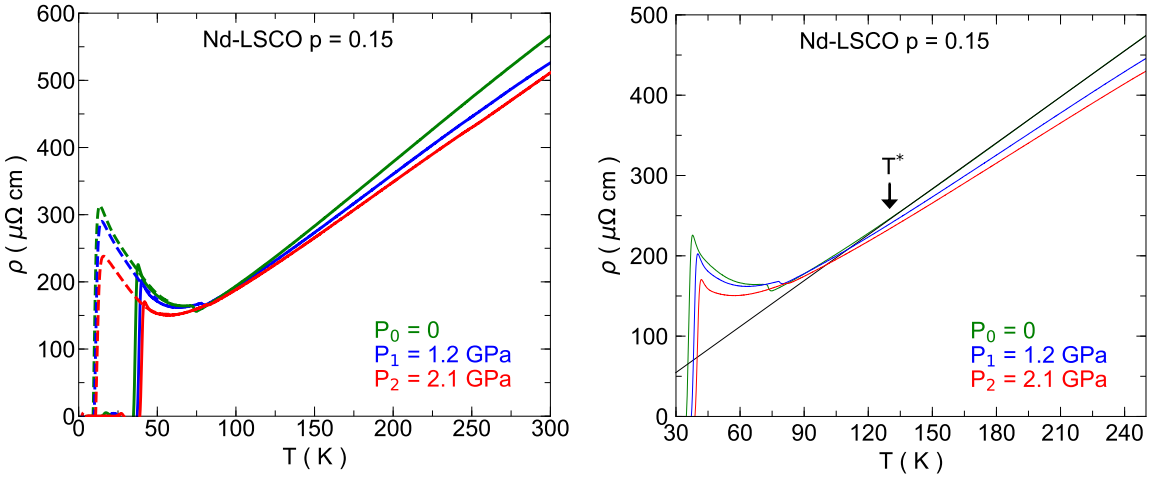

Figure 3.27 Pressure effect on T*. a) The temperature dependence of resistivity in zero magnetic field, note the structural transition is getting smoother by increasing pressure. Solid lines are at 0T and dashed lines are at 16T. b) Linear fit is shown for resistivity at zero pressure. The temperature at which resistivity deviates from linearity is shown by an arrow and it is robust and does not move with pressure (other fits are not shown for simplicity).

below [9].

As mentioned in Chapter one, it is known that pressure can change the crystal structure of Nd-LSCO from LTT to LTO and eventually to HTT (high temperature tetragonal) in pressures higher than 4.2 GPA. Band structure calculations by Minjae Kim at École Polytechnique in France, based on a standard tight-binding model, show that this structural transition from LTT to HTT under pressure causes a decrease in the ratio $|t'/t|$, where t and t' are nearest and next nearest neighbor hopping parameters. In constant doping, it is a property of this model that the Fermi surface goes from hole-like to electron-like with decreasing $|t'/t|$. In contrary to YBCO, doping in Nd-LSCO remains the same under pressure [10]. Pressure applied on Nd-LSCO is therefore expected to reduce p_{FS}.

As mentioned before, the signature of pseudogap is an upturn both in resistivity and Hall effect and for $p > p*$ there is largely a constant R_H and linear resistivity vs T in the normal state down to low temperatures.

[9] Nd is a disorder that is added to LSCO, so by applying pressure we decrease the effect of this disorder by squeezing the crystal to obtain its primary geometry.

[10] Strontium content in Nd-LSCO is much heavier than oxygen in YBCO. So the oxygen atoms require less energy to move in YBCO compared to Sr atoms in LSCO or Nd-LSCO. As pressure is an energy scale too, we need much more pressures to have pressure induced doping effect in LSCO family superconductors. This is a straightforward picture but other parameters are also important for having a pressure induced effect such as Coulomb interactions in a crystal.

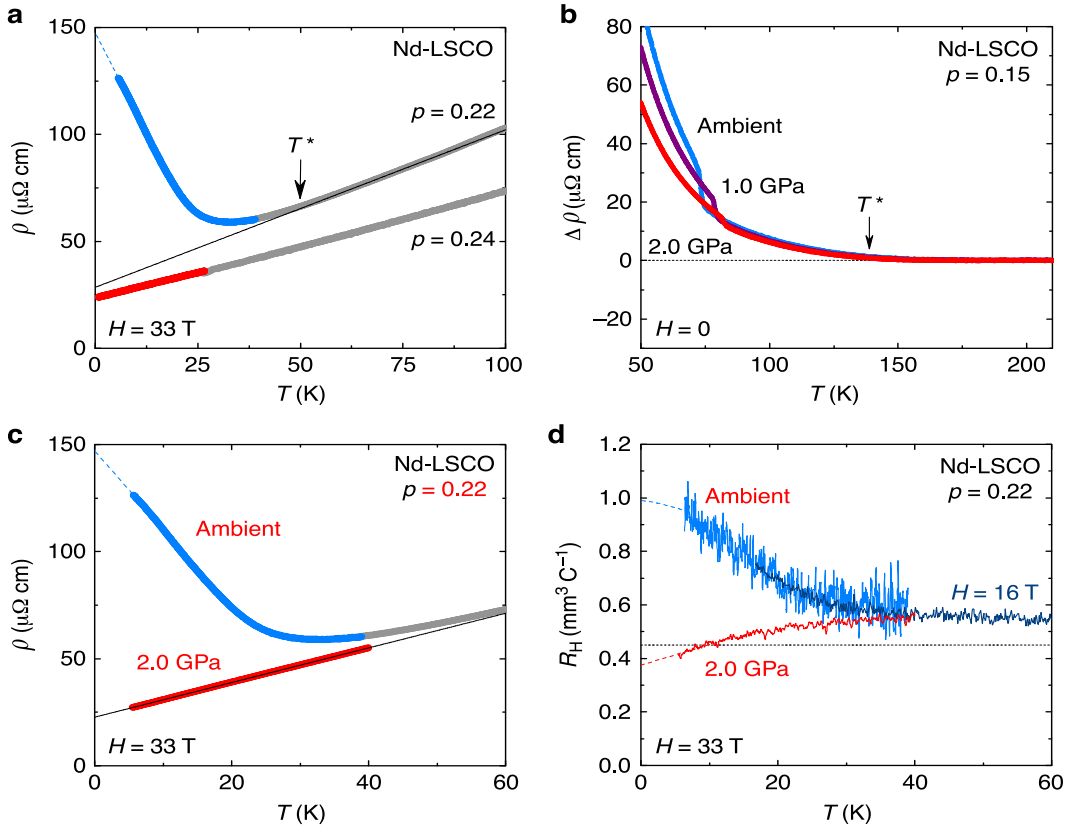

Figure 3.28 Effect of pressure on Nd-LSCO. a) Temperature dependence of the normal state of resistivity in the magnetic field of 33T, below (0.22) and above p* (0.24). b) Difference between the resistivity and its linear fit as displayed in Fig 3.27-b, showing that T* does not move under pressure. c) Application of pressure and suppression of resistivity upturn. d) Application of resistivity and suppression of Hall coefficient upturn. Obtained from [91].

Fig 3.27-a shows the temperature dependence of resistivity for Nd-LSCO p = 0.15 at different pressures up to 250K. In Fig 3.27-b, high-temperature linear fits indicate the onset of the pseudogap. The effect of pressure here is simply to move the structural transition and T_c to higher temperatures. The magnitude of the upturn is decreased to some extent, but it is not a significant change. Thus, the position of T* is not moved.

Fig 3.28-a shows the temperature dependence of resistivity in Nd-LSCO at p = 0.22 and 0.24 which are below and above pseudogap critical point respectively. It is observed that the pseudogap temperature T* falls abruptly to zero at p*[96]. Fig 3.28-b shows the subtraction of the linear fit from resistivity in Fig 3.27-b. It is easier to see that pressure does not move the T*, which shows that T* is robust in the range of 2GPa of pressure at this doping. Accordingly, pressure does not tune T* directly as it was seen in YBCO before [32].

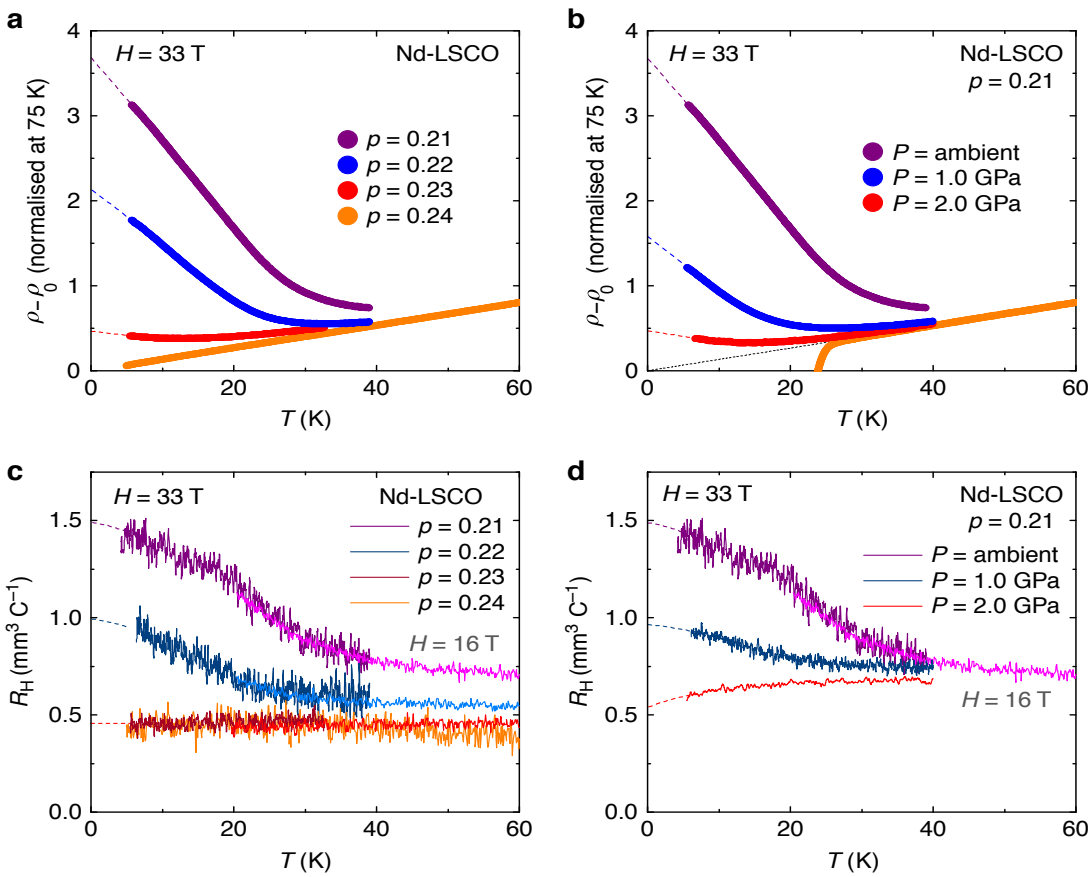

Figure 3.29 Effect of doping and pressure on Nd-LSCO. a) Temperature dependence of resistivity normalized at 75K for various doping of Nd-LSCO at ambient pressure and b) for single doping of p = 0.21 at various pressures. c) Temperature dependence of Hall coefficient at various doping in ambient pressure and d) at p = 0.21 and in ambient pressure, 1 and 2 GPA. Obtained from [91].

Fig 3.28-c shows resistivity vs temperature for Nd-LSCO at p = 0.22 $<$ p* = 0.23$\pm$0.01. The blue curve is at ambient pressure and the red one is at 2GPa. By the application of 2GPa of pressure, the resistivity upturn is suppressed. Fig 3.28-d shows the R_H vs T that is obtained at H = 16T in high temperatures and H = 33T in low temperatures for the same doping. Again pressure suppresses the pseudogap upturn which is located right before .

Fig 3.29-a shows the resistivity vs T of Nd-LSCO for several dopings around p*. By increasing the doping, the upturn becomes less dramatic and it fades out at p = 0.24 $>$ p*. This suggests that the effect of pressure for suppression of CDW is similar to the effect of doping.

Fig 3.29-b shows ρ vs T for Nd-LSCO p = 0.21. The effect of pressure is to decrease the upturn as for p = 0.22. But, here the upturn does not get fully suppressed as it is farther from

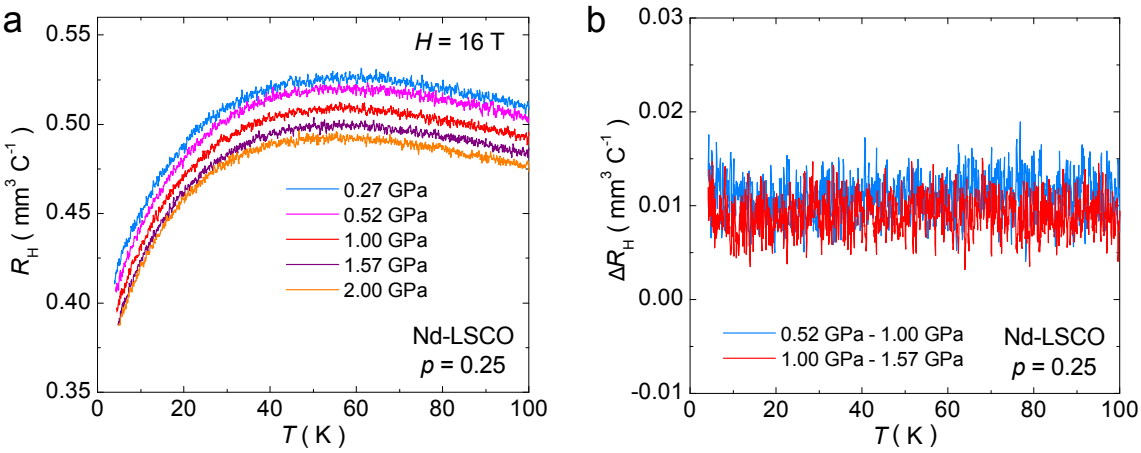

Figure 3.30 Effect of pressure on the Hall coefficient of Nd-LSCO at p > p*. a) Hall coefficient is decreasing monotonically towards zero and negative values. b) Difference between two adjacent isobars in (a), for the indicated pairs. R_H(T) decreases rigidly, at a rate of - 6 % GPa^{-1}, relative to R_H(0) = 0.4 mm^3 C^{-1}. Obtained from [91].

p* and as the pseudogap is stronger, the same amount of pressure (2GPa) is insufficient for suppressing the upturn.

Fig 3.29-c shows R_H vs T. For p = 0.21 and 0.22 the pseudogap upturn is apparent. For p = 0.23 and 0.24 there is no upturn as they are located at p $\geq$ p*.

Fig 3.29-d shows the effect of pressure on the Hall coefficient as a function temperature. 2GPa of pressure completely suppresses the pseudogap upturn, while in the corresponding ρ vs T in Fig 3.29-b, the upturn is partially suppressed. It is because the resistivity is sensitive to all the carrier densities including electrons and holes, while Hall effect is fine-tuned by the balance between them (the exact shape of the Fermi surface is still in question at this doping). Thus, the pressure effect in Nd-LSCO is to move p* to lower dopings.

In overdoped LSCO well-above p* = $p_{FS} \approx 0.18 \pm 0.01$, where the Fermi surface gets reconstructed into a large electron-like cylinder and maintains its shape in higher dopings beyond that doping, the low-temperature normal state of R_H decreases with doping as the system moves sufficiently away from p_{FS}, to eventually become negative at p $\geq$ 0.35 [58, 97]. Nevertheless, R_H does not become negative simultaneously by this Fermi surface reconstruction at p_{FS} (a sketch of the Fermi surface is shown in Fig 1.3-d). R_H is sensitive to the curvature of the Fermi surface. Nodal regions —where the mobility is higher compared to the other parts of the electron-pocket— have more significant effects on the ultimate sign of R_H. If the curvature of the electron-pocket is negative at the nodal directions, the ultimate sign of the Hall coefficient is negative. Likewise, if the curvature is positive in these critical regions (the ones that have high mobility), the Hall coefficient becomes positive at the end (but the whole Fermi surface is still closed and electron-like). We assume that p* = p_{FS}

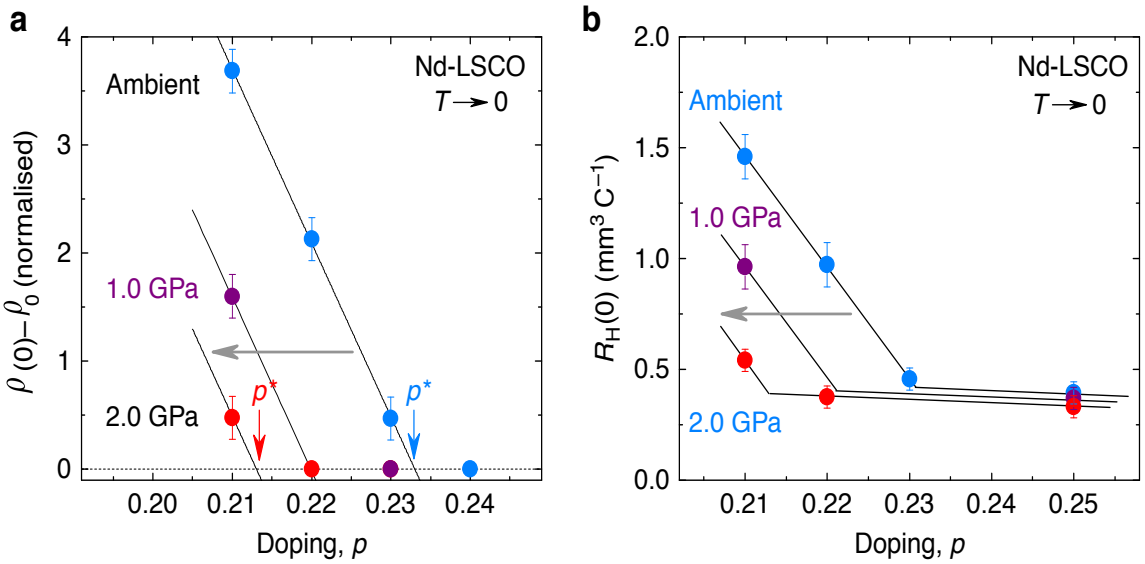

Figure 3.31 Quantitative effect of pressure on p*. a) Magnitude of upturn in resistivity at low temperatures (T→0) for H = 33T. Different colours indicate different pressure as shown in the figure. b) Doping dependence of Hall coefficient at T→0, at H = 16T in p = 0.25 and H=33T for the rest of the dopings. Obtained from [91].

in Nd-LSCO as in LSCO. So, applying pressure at p $>$ p_{FS} (where the Fermi surface is electron-like) could have a different effect compared to the application of pressure at p $<$ p* (where the topology of the Fermi surface is unknown, but it is not electron-like either).

Fig 3.30-a shows the effect of pressure on R_H vs T in overdoped Nd-LSCO at p = 0.25. By increasing the pressure, the magnitude of Hall coefficient keeps decreasing systematically towards negative values: in Fig 3.30-b the difference of Hall coefficient between 0.52 and 1 GPa and also between 1 and 1.57 GPa is shown. ΔR_H is about 0.01 ^{3} C^{-1} for about 0.5 GPa of pressure increment, which corresponds to 6 % GPa^{-1} decrease of R_H with respect to $R_H(0)$ = 0.4 mm^3 C^{-1}. Subsequently, we see that R_H in Nd-LSCO at p = 0.25 decreases by 12 % under 2 GPa, which implies that p_{FS} in Nd-LSCO shifts down by δp_{FS} 0.02 under 2 GPa, which is consistent with the doping impact in LSCO [58, 97].

Fig3.31 sums up all of our findings in this section by showing the temperature dependence of normalized resistivity and extrapolated R_H to zero temperatures. In the limit of T→0, the effect of pressure is to move p* down to lower dopings. Moreover, the magnitude of the Hall coefficient decreases as pressure increases. This is corresponding to getting farther from p_{FS} and Van Hove singularity as indicated in Fig 3.31-b by the gray arrow.

So, p_{FS} is also moving down in pressure like p*. For this specific material, there is a tandem decrease of p_{FS} and p* under pressure. Besides, one can conclude that the required condition for the existence of pseudogap is the presence of a hole-like Fermi surface.

In our recent study of the effect of pressure on pseudogap [91], we realized that pressure could have a considerable effect on the pseudogap's critical point , p*, in Nd-LSCO superconductor. Pseudogap is highly sensitive to the topology of the Fermi surface that a tiny change in its topology with a small amount of pressure: turns it off; despite having a large energy scale of 20 meV [9]. Based on our intuitive understanding, we think that the presence of hot spots —the intersection of the Fermi surface and the AFM zone boundary— on the Fermi surface are necessary for the pseudogap to appear. Moreover, we showed that T* does not move by the application of pressure. One must notice that in ambient pressure, pseudogap ends abruptly before the Van Hove singularity point (p_{FS}) and T* goes to zero at p*, which is located below the p_{FS}. So, by the application of pressure p* move, but T* is not affected.

3.2.2 Thermoelectricity under pressure

Following our results on the pressure effect on the pseudogap probed with electrical transport; we decided to measure thermoelectric power under pressure, namely Seebeck and Nernst effect to prove that the suppression of the pseudogap under pressure is definite and could be seen with other transport probes.

Seebeck coefficient is a result of compensation between thermal gradient applied to the sample and Coulomb force due to the charge of carriers, but the Hall coefficient is a result of the balance between Coulomb and Lorentz force. While both of them unveil the sign of the carriers, they have different sensitivities to the impurities in a crystal.

Nernst effect can reveal the onset of the pseudogap easier compared with the other transport probes as it deviates from the linear regime precipitously allowing us to detect T* more easily [8]. But one should note that the Nernst effect is susceptible to the superconducting fluctuations and mobile vortices which can affect the Nernst signal. To eliminate those contaminations, we apply a high magnetic field. Otherwise, the other contributions may mask the real signal and we may not be able to observe the effect of pressure on the Nernst signal.

Suppressing superconductivity and accessing the normal state in Seebeck effect measurements requires a high magnetic field. Fig 3.32-a,b shows the magnetic field dependence of S/T in Nd-LSCO p = 0.22 at 0.15 GPa (1.5 Kbar) and 2.1 GPa for several isotherms as indicated in the figure. In Fig 3.32-c a comparison between the two pressures is shown. By increasing the pressure, the normal state value of Seebeck effect is decreased more than two times and accessing the normal state requires increased magnetic field (H_{c2} and H_{c1} increase when T_c increases under pressure.)

Fig 3.32-d shows S/T vs H for two pressures of 0.15 GPa and 1.6 GPa at different isotherms as indicated. For technical reasons the second pressure point is not the same as

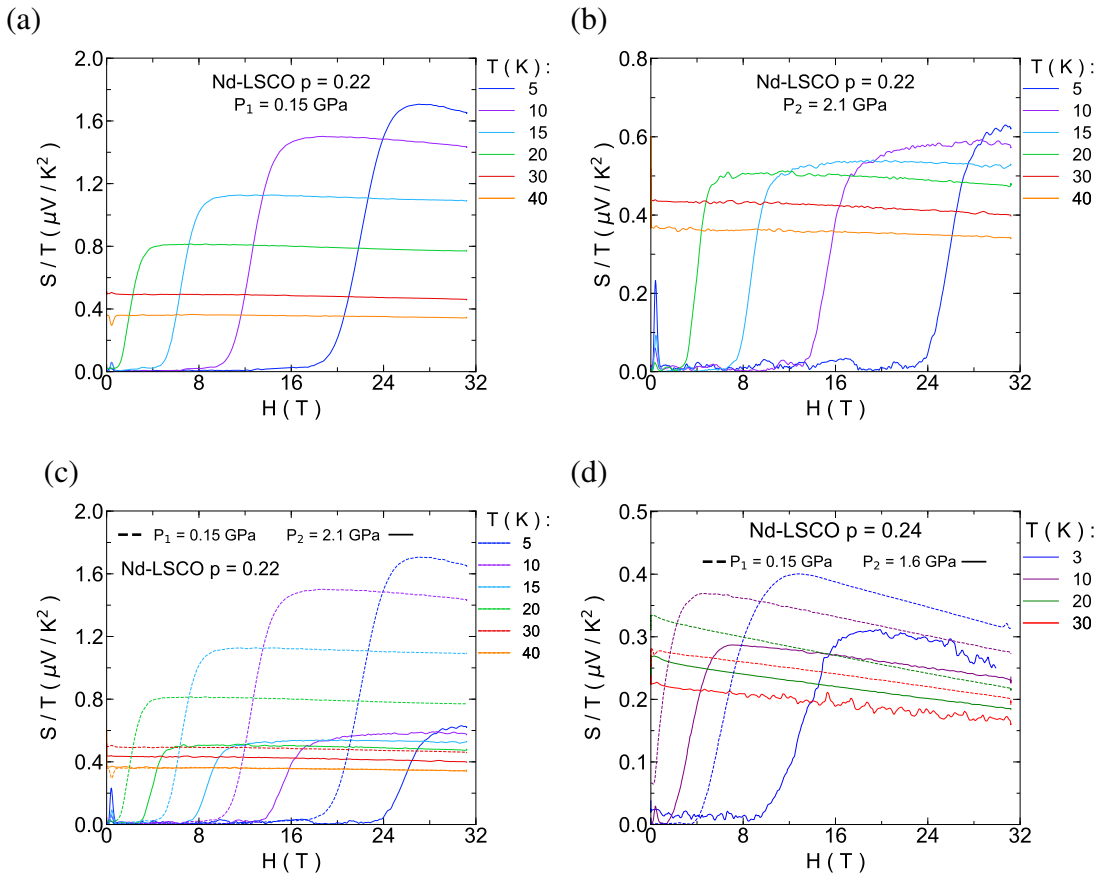

Figure 3.32 Field dependence of Seebeck coefficient over temperature for different temperature isotherms at a) P_1 = 0.15 GPa and p = 0.22 b) P_2 = 2.1 GPa and p = 0.22. c) Comparison between (a) and (b), notice 4 fold decrease of Seebeck signal under 2GPa of pressure. d) Comparison of Seebeck coefficient in p = 0.24, at P_1 = 0.15 GPa (dashed lines) and P_2 = 1.6GPa (solid lines).

the one in p = 0.22, but the pressure effect is still smaller on a normalized scale. As T_c is lower in this doping, superconducting fluctuations could be suppressed much more easily compared to p = 0.22.

To access the normal state of Nernst effect, we need even more magnetic field compared to the Seebeck effect (because of the signal contamination by the superconducting fluctuations and mobile vortices). In Fig 3.33-a,b, ν/T as a function of magnetic field is shown at one pressure close to zero (P_1 = 0.15 GPa) and P_2 = 2.1 GPa. In P_1 the normal state is out of reach for 5, 10 K isotherms. The nature of the double transition at 5 and 10K (fig 3.33-a) could be due to the inhomogeneities in the sample, but in high enough magnetic fields, temperatures and pressures this effect is not present anymore. At P_2 the double transition is not present at low temperatures anymore. Moreover, reaching the normal state is even harder at P_2.

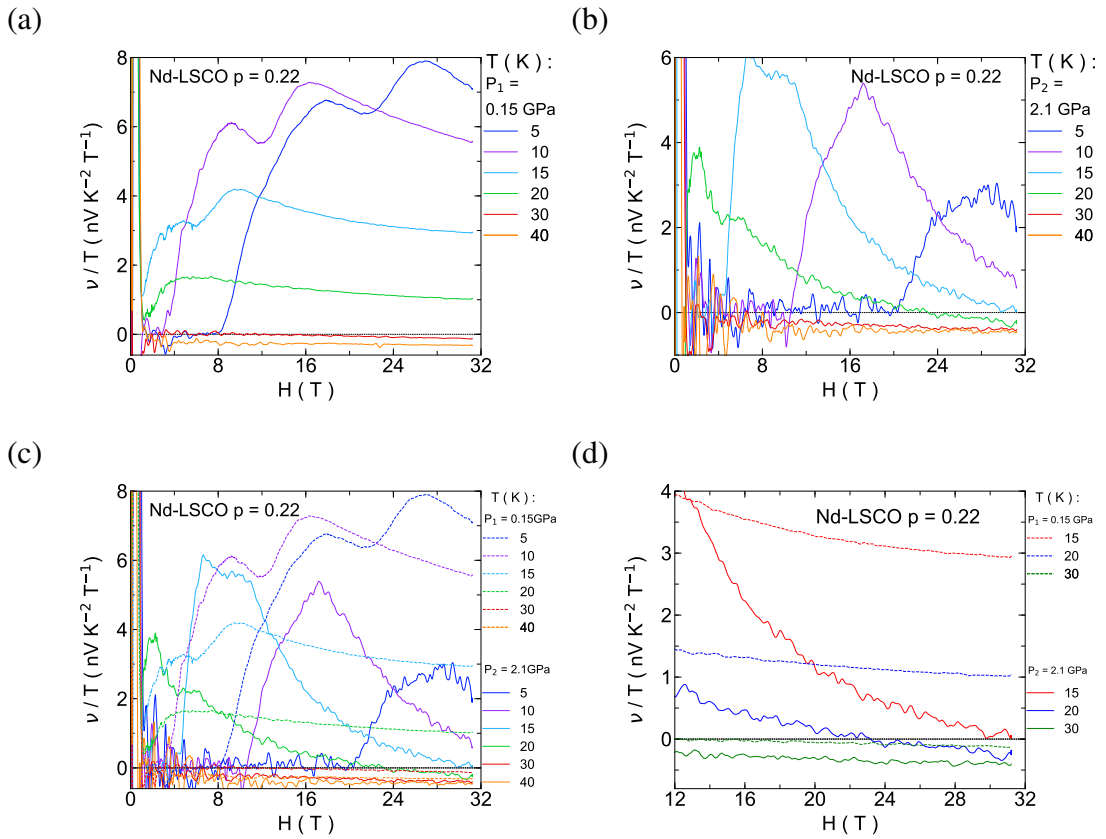

Figure 3.33 Field dependence of Nernst coefficient over temperature for different temperature isotherms at a) P_1 = 0.15 GPa b) P_2 = 2.1 GPa. c) Comparison between (a) and (b). d) Same comparison in (c) but with zoom at high temperature isotherms that become negative eventually in high magnetic fields, less isotherms are shown for more clarity. At low magnetic fields the Nernst signal is not considerable yet that's why the data at lower magnetic fields are noisier compared to the higher fields.

Figure 3.34-c shows a comparison between the two pressure points. We observed that the magnitude of ν has decreased by increasing the pressure. Meanwhile, it becomes more difficult to suppress the superconductivity as the superconducting fluctuations appear at higher temperatures when T_c rises. For instance, at T = 15 K, about 30 T of the magnetic field is required to suppress the superconductivity at P_2 = 2.1 GPa. And it is not possible to have access to higher magnetic fields under pressure in thermoelectric measurements. However, as $T^* \approx 40$ K in Nd-LSCO p = 0.22, suppression of superconductivity even down to 15K is enough to decide if the pseudogap is suppressed or not (by tracking the signature of the pseudogap in ν/T vs T). Fig 3.32-d shows a zoom for high-temperature isotherms. It is noticeable that at P_2, at T = 15 and 20 K, the ν/T signal goes to zero and negative values faster. This might suggest that there is no pseudogap anymore at this doping.

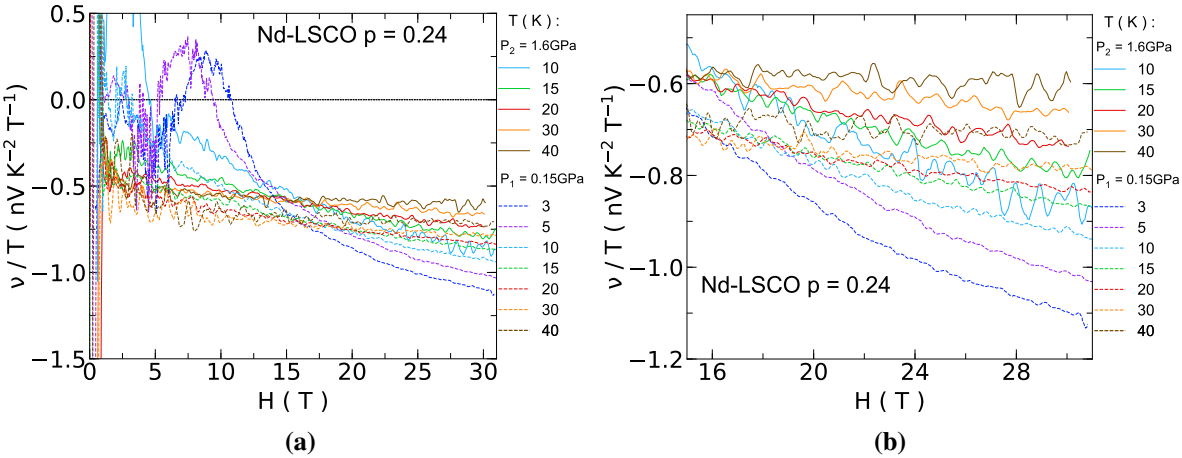

Figure 3.34 a) Field dependence of Nernst coefficient over T under pressure at p = 0.24 for different temperatures at P_1 = 0.15 GPa (dashed line) and P_2 = 1.6 GPa (solid line). b) The data have been enlarged in (a) for more clarity.

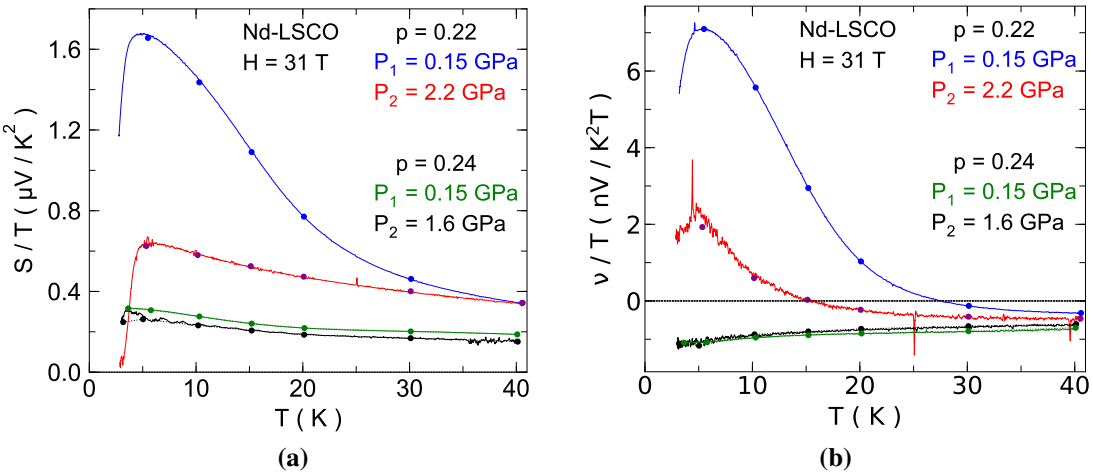

Figure 3.35 a) Temperature dependence of Seebeck coefficient over temperature for Nd-LSCO p = 0.22 at P_1 = 0.15 GPa and P_2 = 2.2 GPa and for Nd-LSCO p = 0.24 at P_1 = 0.15 GPa and P_2 = 1.6 GPa. Circles are field sweep cuts at 31T for different isotherms. b) Temperature dependence of Nernst effect over temperature with the same colour coding as (a).

Fig 3.34 shows the field dependence of ν/T for Nd-LSCO p = 0.24 $>$ p*. As the pseudogap is not present in this sample, at high magnetic fields it shows negative ν/T for all of its isotherms. By increasing the pressure, the high temperature value of ν/T increases slightly.

Fig 3.35-a shows the temperature dependence of Seebeck coefficient over temperature for p = 0.22,0.24 at two different pressures. Circles are the field sweep cuts of Fig 3.32 at

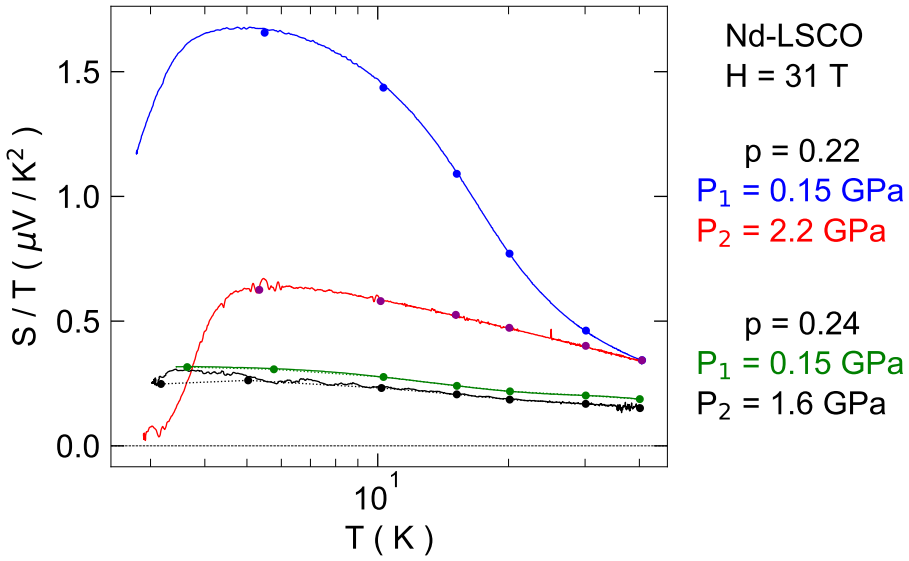

Figure 3.36 Logarithmic temperature dependence of Seebeck coefficient over temperature for Nd-LSCO p = 0.22 at P_1 = 0.15 GPa and P_2 = 2.2 GPa and for p = 0.24 at P_1 = 0.15 GPa and P_2 = 1.6 GPa. Circles are field sweep cuts at 31T for different isotherms.

different temperatures. The Seebeck coefficient upturn is fully suppressed at p = 0.22 which is the consequence of the suppression of pseudogap. Consequently, p* moves down. After the suppression of pseudogap in p = 0.22, at P_2 the curve is comparable to the one at p = 0.24 which is located above p*.

In Fig 3.36, at p = 0.22 at 0.15 GPa, S/T does not have logarithmic temperature dependence. While at 2.2 GPa it represents a more logarithmic T dependence, comparable to the fully logarithmic behaviour of S/T vs T at p = 0.24 at different pressures.

At p = 0.24, the effect of pressure is to slightly decrease the magnitude of the Seebeck coefficient towards lower values.

The temperature dependence of Nernst signal over temperature (ν/T) is depicted in Fig 3.35-b, for p = 0.22 and 0.24. Circles are the field sweep cuts of different isotherms in Fig 3.33 and Fig 3.34. For p = 0.22, as it is shown in field sweeps (fig 3.33), a magnetic field of 31 T could not fully suppress the superconductivity below 15K. Consequently, an upturn is still present at lower temperatures although, the magnitude of its maximum is decreased about three times.

We have measured resistivity and Hall effect on this sample and it reproduced the same result as in [91]. ν/T vs T for Nd-LSCO p = 0.24 (fig 3.35-b) is not affected significantly with pressure: as p $>$p*, there is no pseudogap and no major upturn to suppress with pressure. Moreover, the noise level is higher in higher pressures for all of our thermopower measurements. It is because the pressure medium's heat conductivity increases by the

increase of pressure which makes the applied thermal gradient smaller for the same applied power.

By improving our experimental setup, we were able to measure thermoelectricity under pressure in high magnetic fields in cuprates for the first time. By suppressing the superconducting fluctuations we accessed the normal state of Seebeck and Nernst coefficient and we proved that pressure suppresses the pseudogap in Nd-LSCO and p* is moving down in doping.

3.3 T-linear resistivity above p* in high magnetic fields

As discussed in Chapter one, different parts of the phase diagram may have different scattering mechanisms and the Fermi liquid state is reflected in the quadratic temperature dependence of resistivity.

In the heavily overdoped samples and at low temperatures we expect to have a Fermi-liquid ground state which should be manifested by the quadratic temperature dependence of resistivity, as observed in pnictides [98] and cuprates [46, 99]. T-linear resistivity which is the hallmark of the strange metal phase has been the subject of many different debates [46].

Linear and quadratic magneto-resistance (MR) should not necessarily have the same behaviour as T-linear resistivity [100]. However, in pnictides, and recently in cuprates, a scaling relation between T and H has been reported [101] and [48]. Another important aspect of linear-in-field magneto-resistance and linear-in-temperature resistivity is that they might be pointing to quantum criticality. Furthermore, it has recently been discovered that the T-linear resistivity in the hole and electron-doped cuprates could be because of reaching the Planckian limit [45], which has attracted more attention to this part of the phase diagram.

Here we study two different cuprates at the same dopings: Nd-LSCO at p = 0.24 $>$ p* = 0.23 and LSCO at p = 0.24 $>$ p* = 0.18 to study their normal state and high field magneto-resistance regimes above p*.

The central questions that we try to address in this study are: What is the field dependence of MR? Does it have linear or quadratic behaviour? In order to check if the MR is linear or quadratic in-field, we need to fit the data with the following fitting functions respectively:

$$\rho(T,H) = a + b \cdot H \tag{3.2}$$

$$\rho(T,H) = a + c \cdot H^2 \tag{3.3}$$

The fitting range of the resistivity vs H is of great importance. With a broader fitting range, a more reliable fit can be achieved. That is why one must have access to very high magnetic fields. In lower temperatures, the magnetic field provides access to the normal state, which results in having a smaller fitting range. In high temperature superconductors such as YBCO for instance, the H_{c2} is very high [102]. So, in the first place, one requires a very high magnetic field to access the normal state to have access to a reasonable fitting range. However, just accessing the normal state in YBCO requires a magnetic field of over 100T. In Nd-LSCO, as H_{c2} is lower ($H_{c2} \approx 20$T), we do not need such magnetic fields to suppress superconductivity. Consequently, we can obtain a relatively large fitting range.

3.3.1 Nd-LSCO p = 0.24

Fig 3.37 shows the resistivity of Nd-LSCO at p = 0.24 vs magnetic field for different isotherms with different fitting functions. In this figure, the fitting range is between 50T to 84T. Fig 3.37-Top shows that the low-temperature isotherms fit better (in a bigger range) with the linear fitting function 3.2, while in 3.37-Bottom, the high-temperature isotherms fit better with the quadratic function 3.3 (by increasing the temperature, the quadratic fitting becomes better and better).

Fig 3.38 shows the subtraction of resistivity vs H (fig 3.37) with linear and quadratic fits. It is showing again that the quadratic fitting range can fit a bigger magnetic field range by increasing the temperature and at T = 100 K, the quadratic MR is visible in the whole range of the data as it is not the case for the linear fit.

In order to have a quantitative measure for the goodness of the fit, we use a statistical parameter called coefficient of determination, R^2. It calculates the square of the distance of each point of our data which is not located on the fitting line, then normalizes it. The value of this parameter should be between 0 and 1. When it is equal to one, it means that all of the points in our data are located on top of the fitting function. The caveat of this statistical parameter is that it reflects the noise in its value, but, here we used exactly the same data (with the same noise level) with different fitting functions. So, because of that, it is impossible to get $R^2 = 1$, but we can compare R^2 of linear and quadratic fits for the same isotherms together.

It is evident that R^2 is defined within the fitting range. Thus we increased our fitting range to 20-84T so that R^2 reflects the goodness of the fit in a bigger range of our data. Fig 3.39 shows linear and quadratic fits for ρ vs H and on the right side of each figure R^2 is printed for each isotherm. At T = 100K, $R^2 = 0.9728$ for the linear fit and $R^2 = 0.9973$ for the quadratic fit. This suggests that the quadratic fit at T = 100 K is better than the linear fit.

Fig 3.40 shows the temperature dependence of resistivity. Intercepts of linear 3.2 and quadratic 3.3 functions (coefficient a) and the value of resistivity at H = 80T are shown

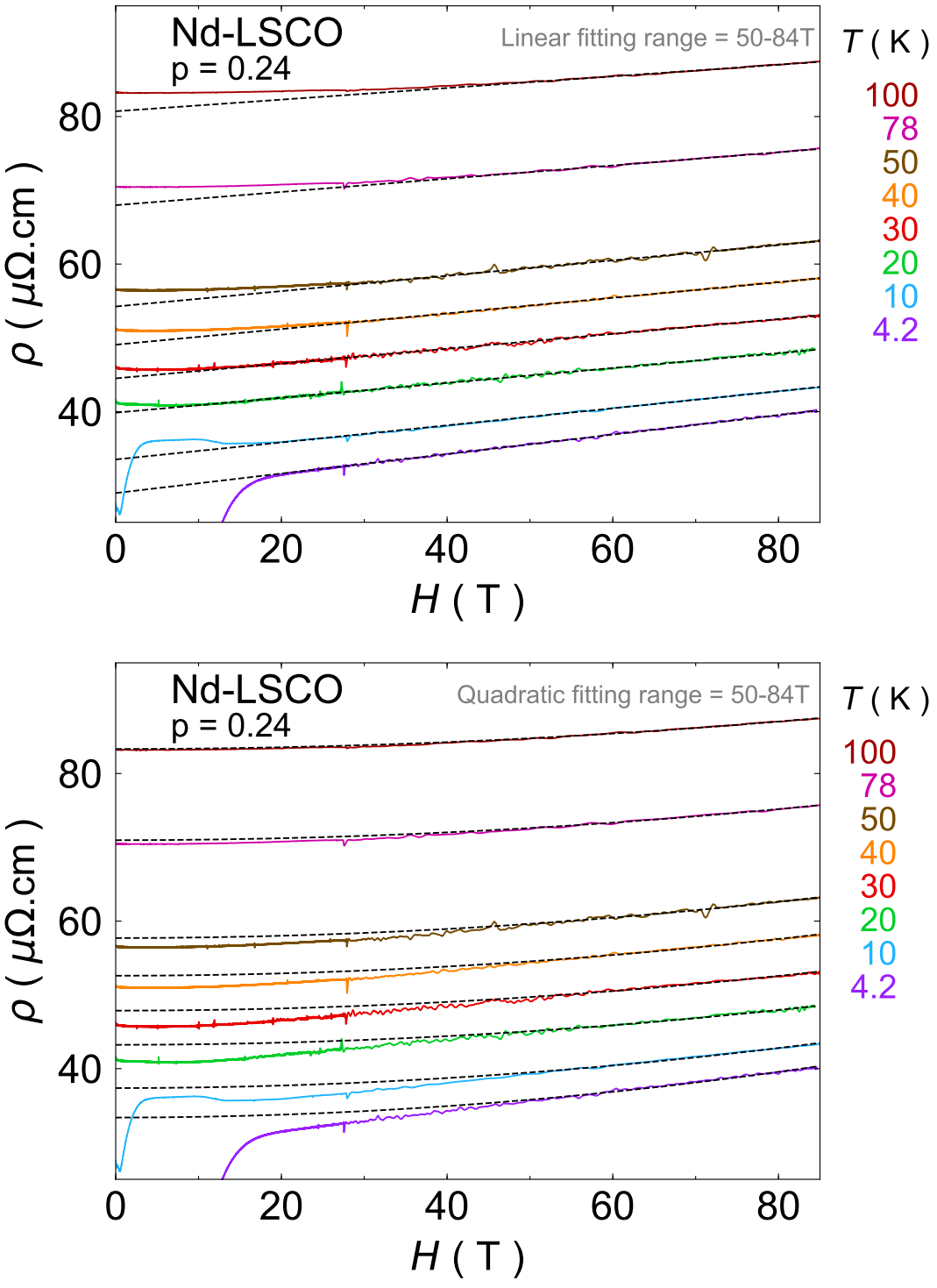

Figure 3.37 Resistivity vs magnetic field for Nd-LSCO p = 0.24 in different isotherms as indicated. Top: Linear fit with 3.2 function. Bottom: Quadratic fit with 3.3 function. The fitting range for the two figures is between 50 T and 84 T.

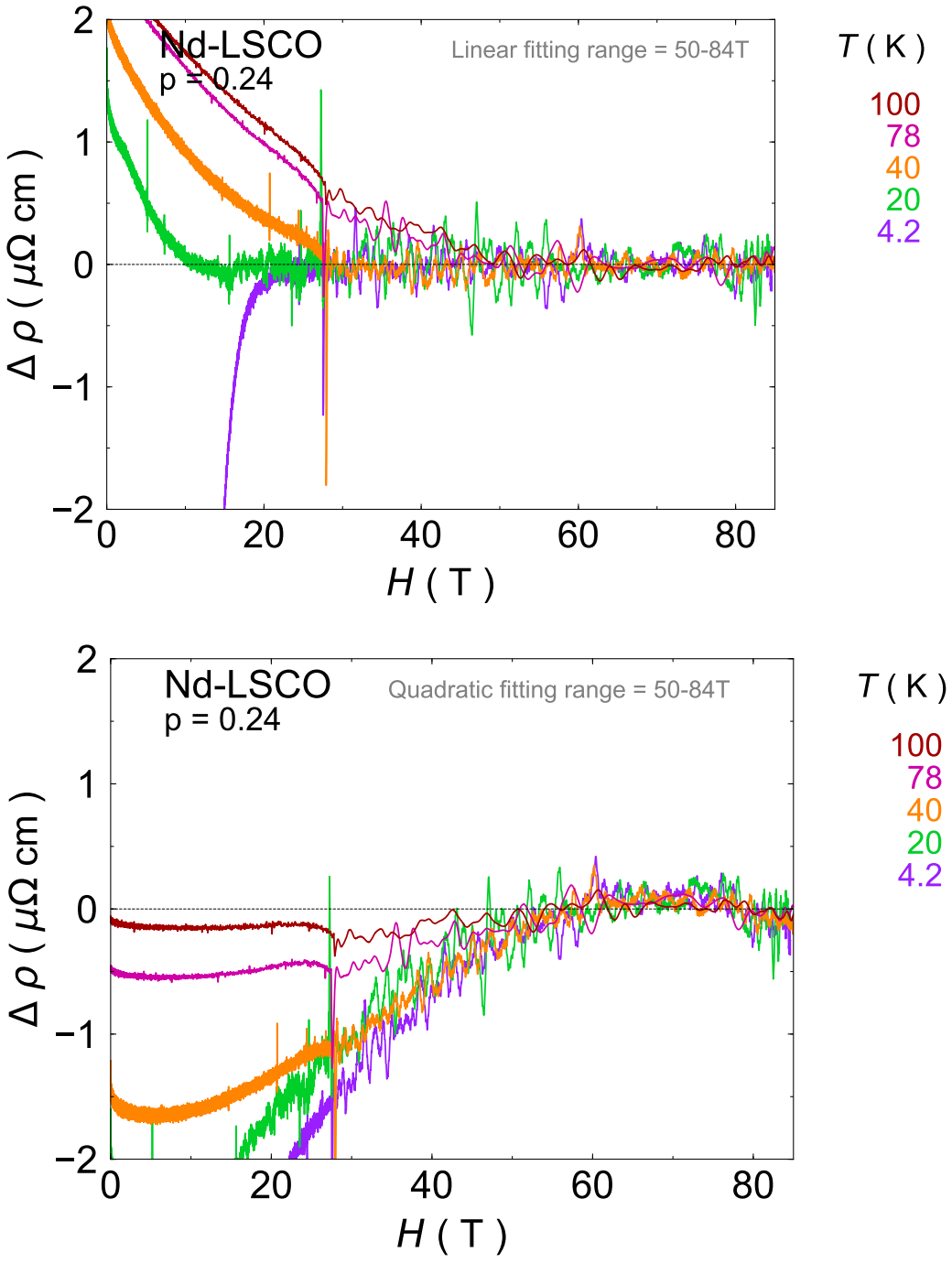

Figure 3.38 Top) Subtraction of resistivity and linear fit and Bottom) subtraction of resistivity and quadratic fit for Nd-LSCO p = 0.24. The fitting range is the same as Fig 3.37. A few isotherms are shown for clarity.

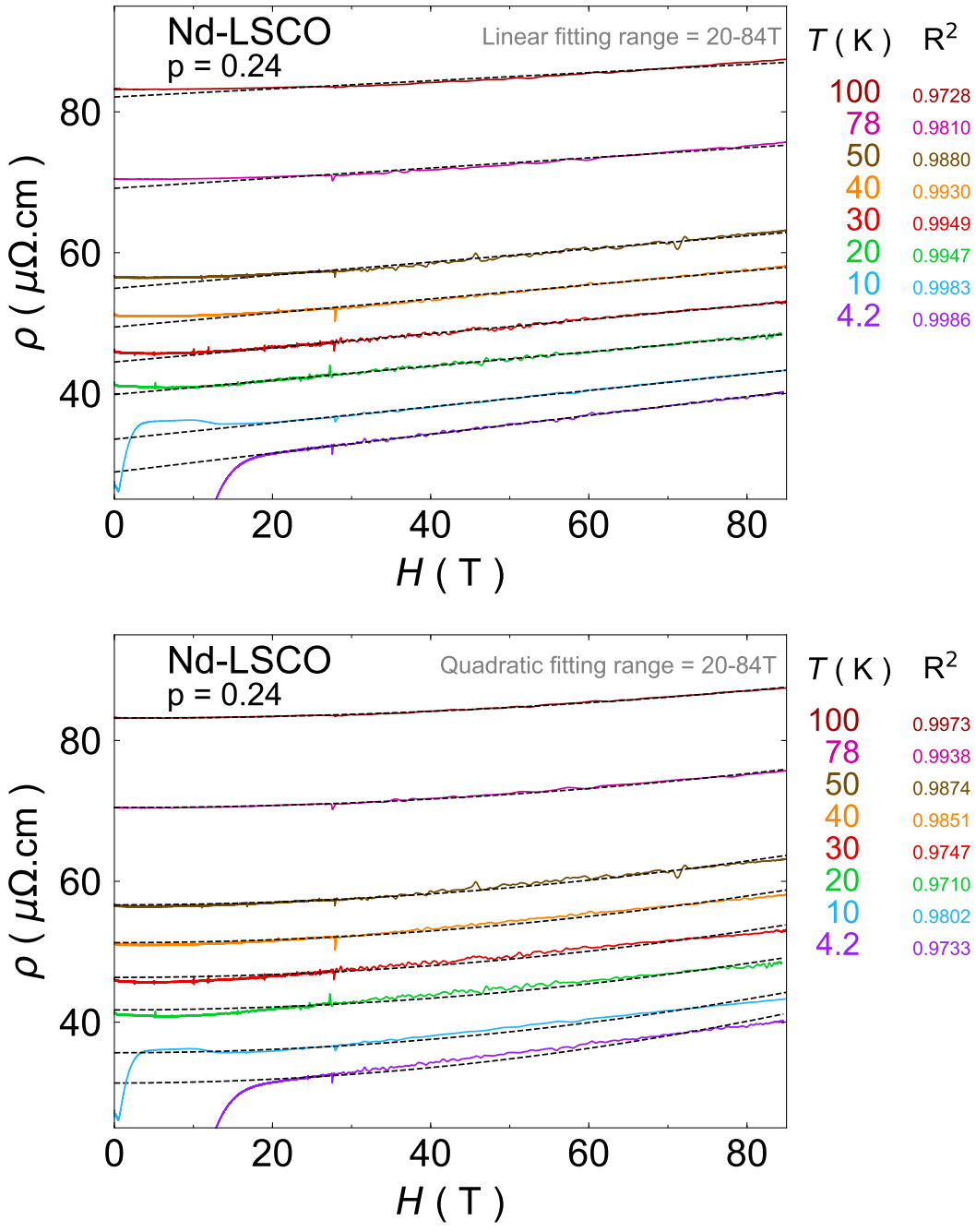

Figure 3.39 Resistivity vs magnetic field for Nd-LSCO p = 0.24 fit with Top: Linear fitting function; Bottom: quadratic fitting function. R^2 is the coefficient of determination that is plotted next to each isotherm temperatures. The fitting range is 20-84 T for all the isotherms.

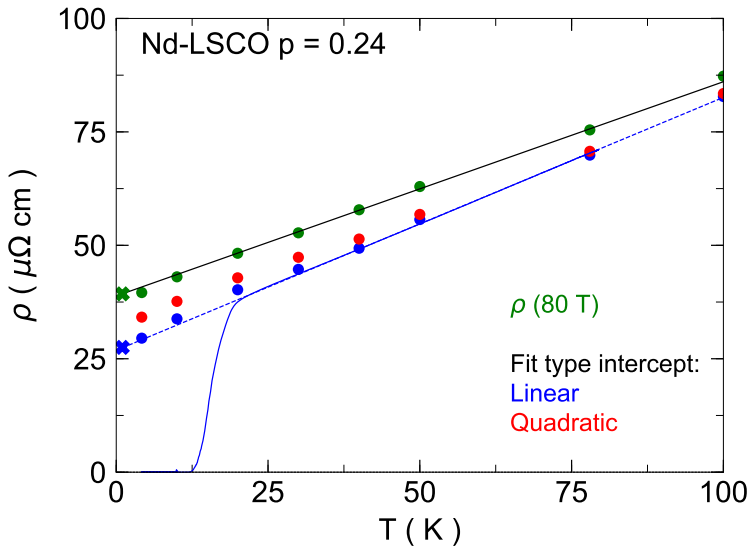

Figure 3.40 Temperature dependence of resistivity in Nd-LSCO p = 0.24. Blue line is the resistivity at 0 T. Blue and red circles are the intercept of the linear and quadratic fits of resistivity vs H (coefficient a in 3.2 and 3.3). Green circles are the value of resistivity at H = 80 T. Blue and green crosses are showing ρ_0 for 0 and 80T back extrapolation to 0K.

and compared with the resistivity at H = 0 T. The circles are obtained with the fitting range of 20-84 T and in this fitting range, the error bars are within the diameter of the symbols. However, the convoluted errors for different fitting ranges are much bigger but for the interest of clarity they are not shown. The distance between ρ (80 T) and ρ (0 T) shows the MR, which is increasing by decreasing the temperature. The value of linear intercepts is in better agreement with ρ (0 T) curve compared with the quadratic intercept values. However, at higher temperatures (T = 78 and 100 K) the value of quadratic intercepts are having a better agreement with ρ (0 T) compared with the linear intercept coefficient. It should be mentioned that the temperature dependence of resistivity which is linear at H = 0 (above T_c), remains T-linear at 80T, down to lowest temperatures, even in the presence of magnetoresistance.

3.3.2 LSCO p = 0.24

We have performed the same experiments on LSCO with the same doping of p = 0.24. However, in LSCO T_c = 16K, while in Nd-LSCO T_c = 9.4K (here T_c is where resistivity goes to zero), we need a higher field to suppress the superconductivity (40T vs 20T) and the fitting range is slightly smaller.

Fig 3.41 shows the resistivity vs magnetic field for LSCO p = 0.24 at different temperatures. Fig 3.41-Top shows the linear fit using 3.2 function and Fig 3.41-Bottom shows the

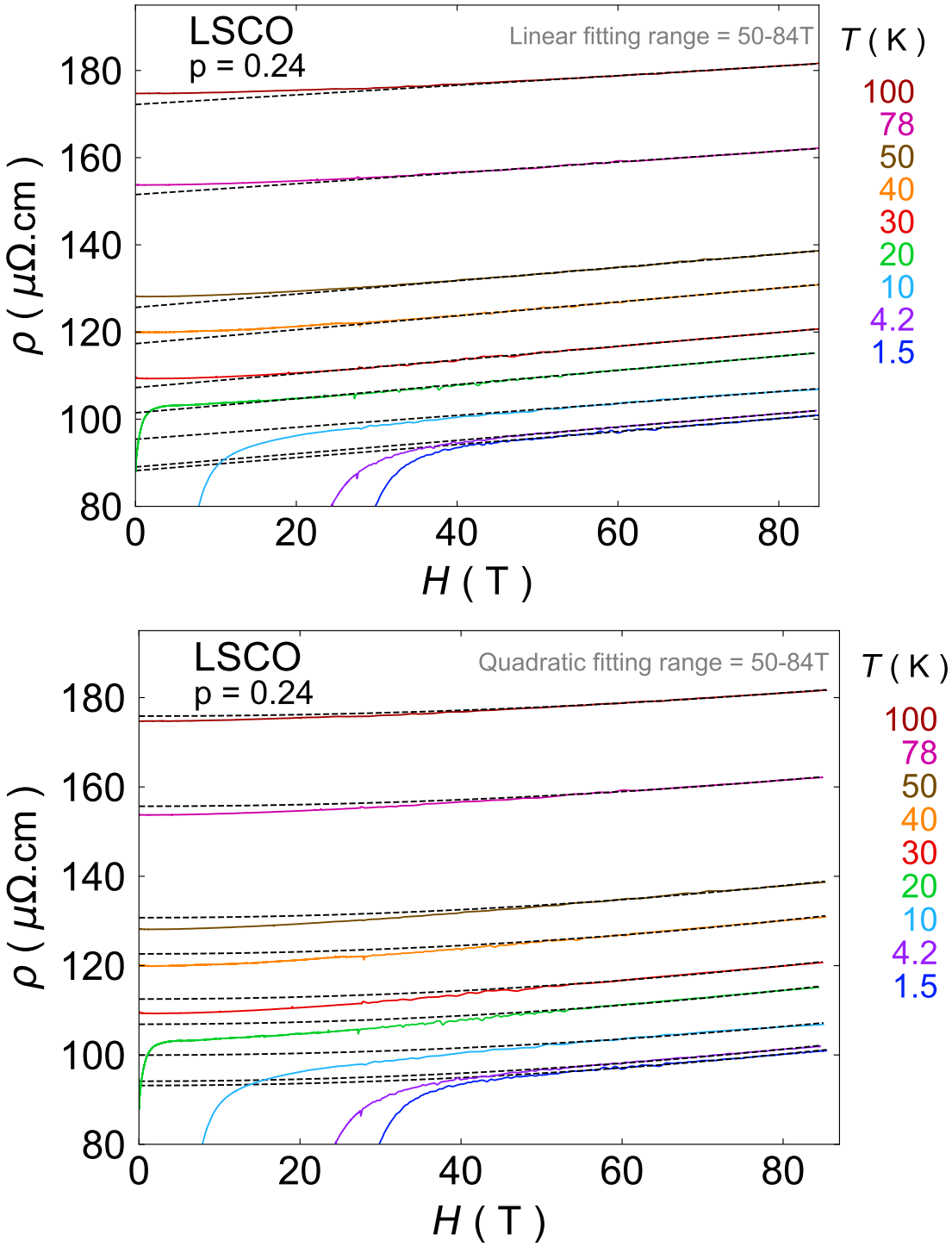

Figure 3.41 Field dependence of resistivity LSCO p = 0.24 in different temperatures as indicated. In top) Linear and bottom) Quadratic fits are shown for the fitting range of 50-84 T.

quadratic fit using 3.3 function.

To observe the deviation of resistivity from linear and quadratic fits, in Fig 3.42we plot $\Delta\rho$ vs H which is the subtraction of ρ and different fits. It shows that at the highest temperature (T = 100K), the resistivity shows a quadratic behaviour. However, it is not as linear as 100 K isotherm for Nd-LSCO and there is a bigger deviation from the quadratic fit at lower magnetic fields. This suggests that LSCO p = 0.24, shows a quadratic MR at higher temperatures compared with the corresponding doping of Nd-LSCO.

Fig 3.43 shows the temperature dependence of resistivity. The difference between ρ (80 T) and ρ (0 T) is smaller compared with Nd-LSCO, meaning that the magneto-resistance is smaller compared with Nd-LSCO. However, at low temperatures, MR is higher compared with higher temperatures. The ρ (0 T) vs T at low temperatures is in better agreement with the linear intercept while at higher temperatures it is the case for quadratic fit.

Unfortunately, we did not have access to higher temperatures for our high field measurements on LSCO p = 0.24. By increasing the temperature, it is clear that the MR becomes more quadratic (it is not fully quadratic at T = 100 K though). Hence, we compared our MR data on LSCO p = 0.24 with LSCO p = 0.19 from Ref [48] at which the higher temperature data were available.

Fig 3.44 shows the published MR data and high temperature isotherms of resistivity vs H for LSCO p = 0.19 compared with our data on LSCO at p = 0.24. At 180 K, the resistivity of LSCO p = 0.19 becomes fully quadratic. It is also shown by plotting the residues of linear and quadratic fit vs H in Fig 3.45.

3.3.3 Scaling between temperature and magnetic field

We also checked the scaling of resistivity and magnetic field: the ansatz that has been observed in pnictides earlier [101]. It is claimed that resistivity has the following T and H dependence:

$$\rho(H,T) - \rho(0,0) \propto \sqrt{(\alpha K_B T)^2 + (\gamma \mu_B \mu_0 H)^2} \equiv \Gamma \tag{3.4}$$

Where k_B is the Boltzmann constant, μ_B is the Bohr magneton and the γ and α are dimensionless parameters.

We realized that Γ is highly dependent on the residual resistivity values. Having 10-20 % of uncertainty in the value of ρ_0 was inevitable in our high field measurements. ρ_0 is the resistivity at 0K and it is defined by the back extrapolation of ρ vs T to zero Kelvin. We used the value of ρ_0 at 0T, and it is the same as in field ρ_0 if the magnetoresistance of material is

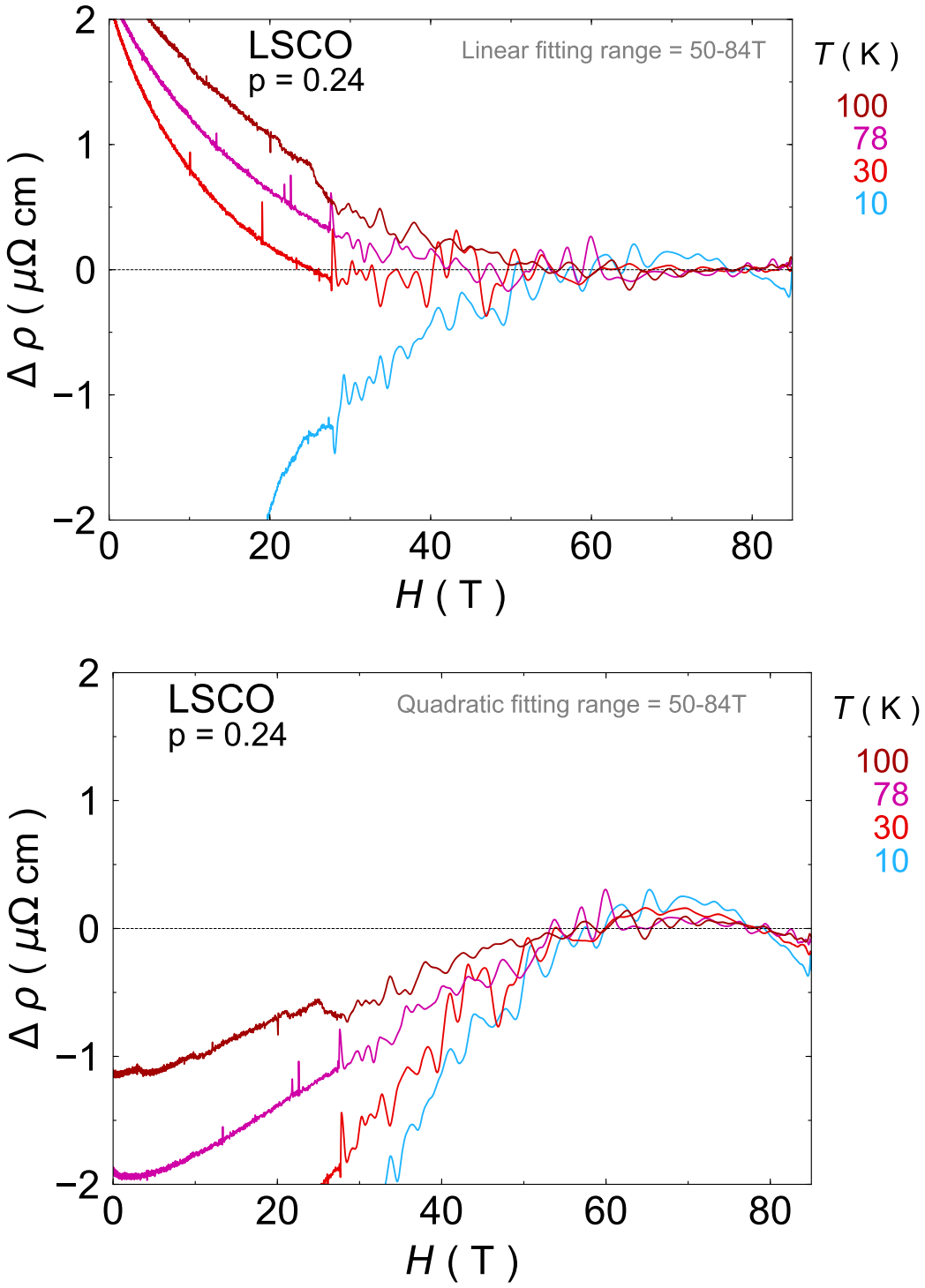

Figure 3.42 Subtraction of resistivity and top) linear bottom) quadratic fit of LSCO p = 0.24 in different temperatures for the fitting range of 50-84 T.

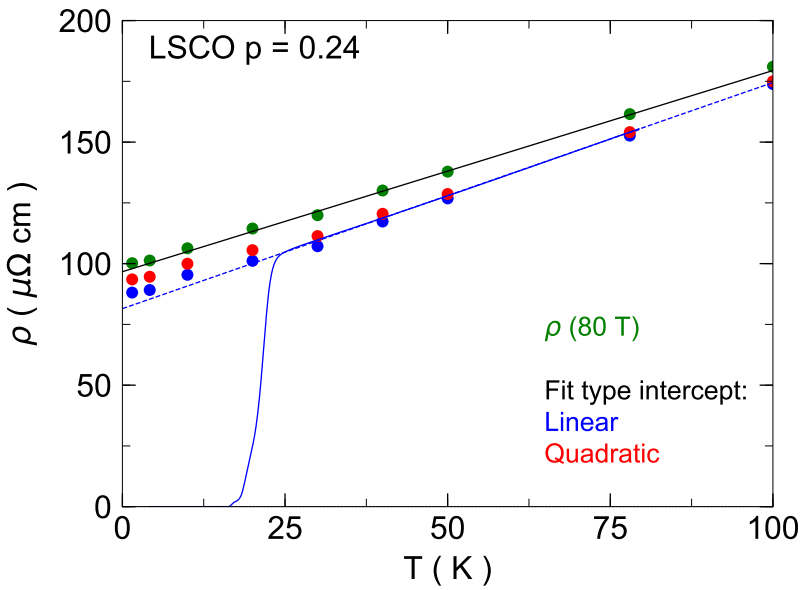

Figure 3.43 Temperature dependence of resistivity in LSCO p = 0.24. Blue line is the resistivity at 0 T. Blue and red circles are the intercept of the linear and quadratic fits of resistivity vs H (coefficient a in 3.2 and 3.3). Green circles are the value of resistivity at H = 80 T.

close to zero. But, it is not zero in our case. Fig3.40 shows the zero and in-field ρ_0 by blue and green crosses respectively. [11].

Fig 3.46 shows the scaling between resistivity and magnetic field in Nd-LSCO and LSCO. For Nd-LSCO p = 0.24, this scaling behaviour works better compared with the corresponding doping of LSCO as each isotherm of ρ (T,H) has a similar slope to one another. But, visually it is not as good as the scaling in pnictides themselves [101]. There is no definitive quantitative criterion for the precision of T-H scaling.

As it is suggested in Ref [101], for the cuprates, T−H scaling works similar to pnictides, but this is still subject of some debates. Fig 3.47 shows ρ vs Γ. Here we show that for one case of cuprates this mechanism works to some extent (Nd-LSCO) while for another one it does not (LSCO).

Thus, further experiments are needed to confirm this phenomenological theory in cuprates, and if this behaviour is not universal, it is important to understand why it is not.

[11] We had to use samples with small thickness for having an acceptable high signal to noise ratio. Our samples were about 30 μm thin, and small imprecision in measuring it can affect ρ_0 considerably. For instance, by having 2μm of uncertainty in measuring the thickness, the value of ρ_0 can change about 10%.

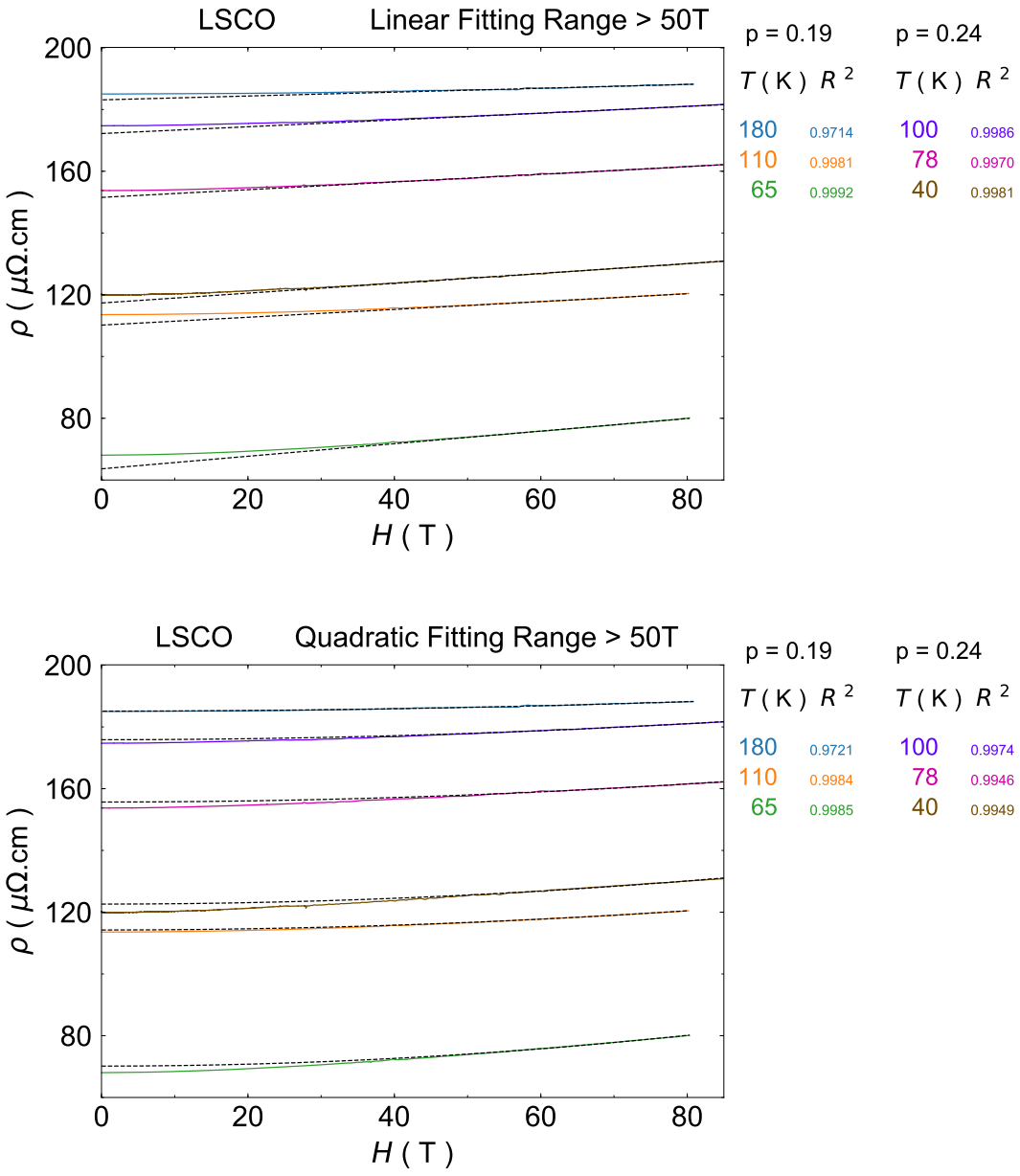

Figure 3.44 Resistivity vs magnetic field for LSCO p = 0.19 and 0.24. Top: Linear fitting range of 50T - maximum field. Bottom: Quadratic fitting in the same range. The data at p = 0.19 is obtained from [48].

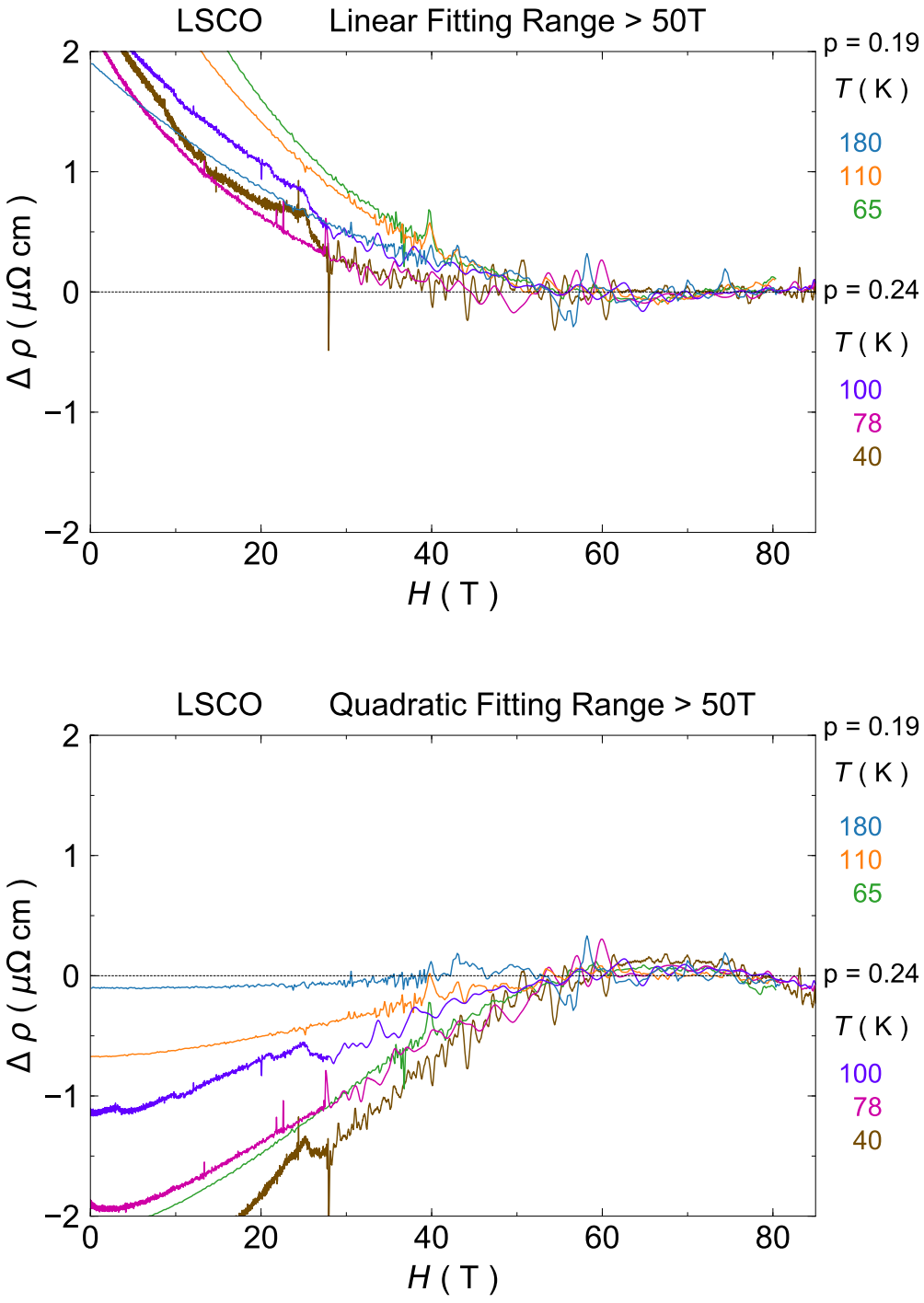

Figure 3.45 Resistivity vs magnetic field for LSCO at p = 0.19 and 0.24. Top: Linear and Bottom: Quadratic fit. With the fitting range of 50T - maximum field. The data at p = 0.19 is obtained from [48].

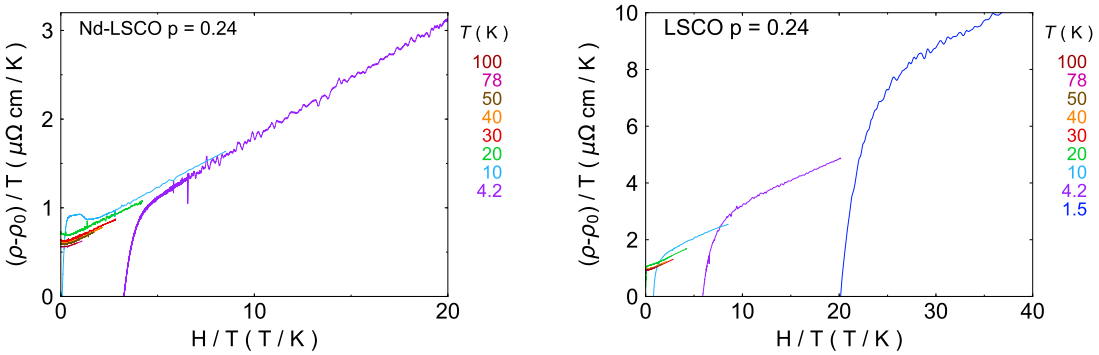

Figure 3.46 Plot of $(\rho - \rho_0)$ / T vs H / T for Left: Nd-LSCO; Right: LSCO at p = 0.24. Isotherm temperatures are shown on the right side of each plot.

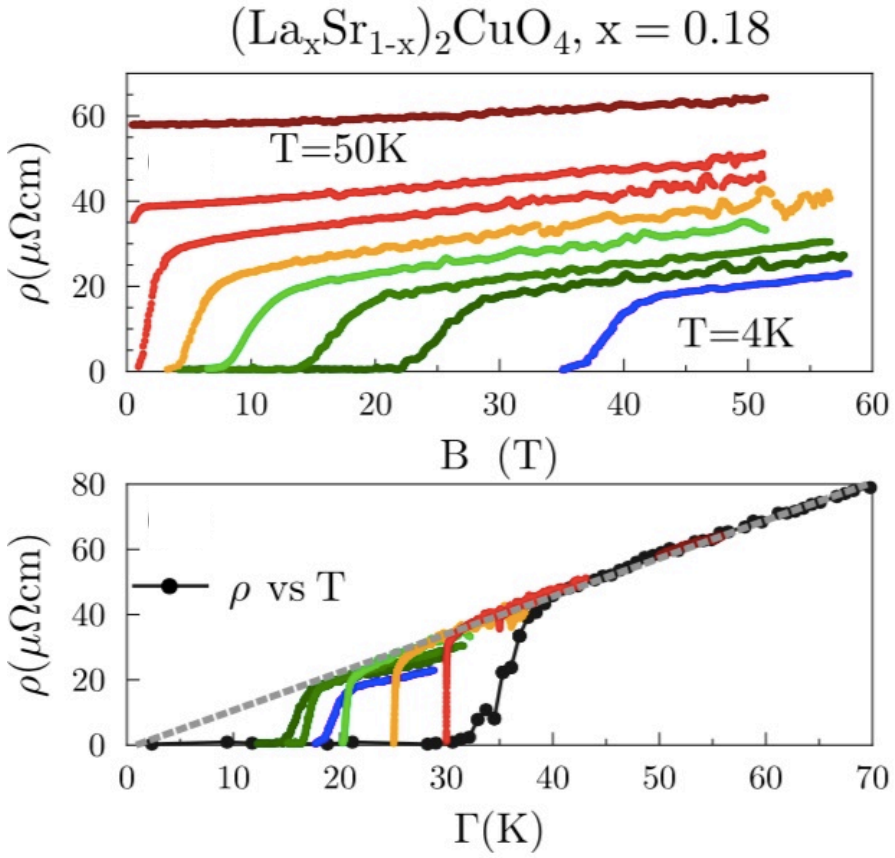

Figure 3.47 Top: resistivity vs magnetic field for LSCO p = 0.18 at different temperatures as indicated. Bottom: Plot of ρ vs Γ. The black circles are temperature dependence of resistivity at zero magnetic field. The figures are obtained from Ref [101].

Conclusion and prospects

This thesis has been focused on the study of the pseudogap phase and charge order in Nd-LSCO with thermoelectric and electric transport measurements under pressure. We have also studied the magnetoresistance and linear- and quadratic-in-field resistivity in Nd-LSCO and LSCO at p = 0.24 and in high magnetic fields.

First, we studied the pressure effect on the charge density wave (CDW) phase. By looking at the downturn in Hall coefficient vs. temperature —which is the signature of CDW— at p = 0.12 and 0.15, we find that 2GPa of pressure does not suppress this order as this downturn is still present. However, at higher doping (p = 0.17)—where CDW is weaker—the downturn of Hall coefficient has moved more effectively by 2 GPa of pressure (we need to have access to higher magnetic fields to observe this clearly).

In the second part of this thesis, we measured the electrical transport in Nd-LSCO under pressure and suppression of resistivity and Hall effect upturn, which are the well-known signatures of pseudogap. We concluded that the pseudogap's critical point, p*, can be tuned (lowered) with pressure. Moreover, p* and p_{FS}, the dopings where the Fermi surface changes topology (from hole-like to electron-like), satisfies the condition of $p^* \leq p_{FS}$ which implies that the pseudogap cannot exist in an electron-like Fermi surface. The pressure effect on higher dopings above p* is to make the Fermi surface more electron-like which could be detected by a systematic decrease in the low-temperature normal state value of Hall coefficient. We confirmed these results using thermoelectricity where the strong low-temperature upturn in the Seebeck and Nernst coefficients gets much weaker with pressure.

In non-pressure part of this thesis, by tracking the T_{max} in the temperature dependence of Seebeck coefficient over temperature, we pinpointed the endpoint of CDW in Nd-LSCO at doping between p = 0.17 and p = 0.19. Knowing that the p* is at p = 0.23, this suggests that the pseudogap and CDW phase are separate phases, as proposed earlier for YBCO and LSCO.

Lastly, by measuring the resistivity of Nd-LSCO at p = 0.24 and LSCO at p = 0.24 in extremely high magnetic fields (in excess of 80T), we studied the field dependence of the

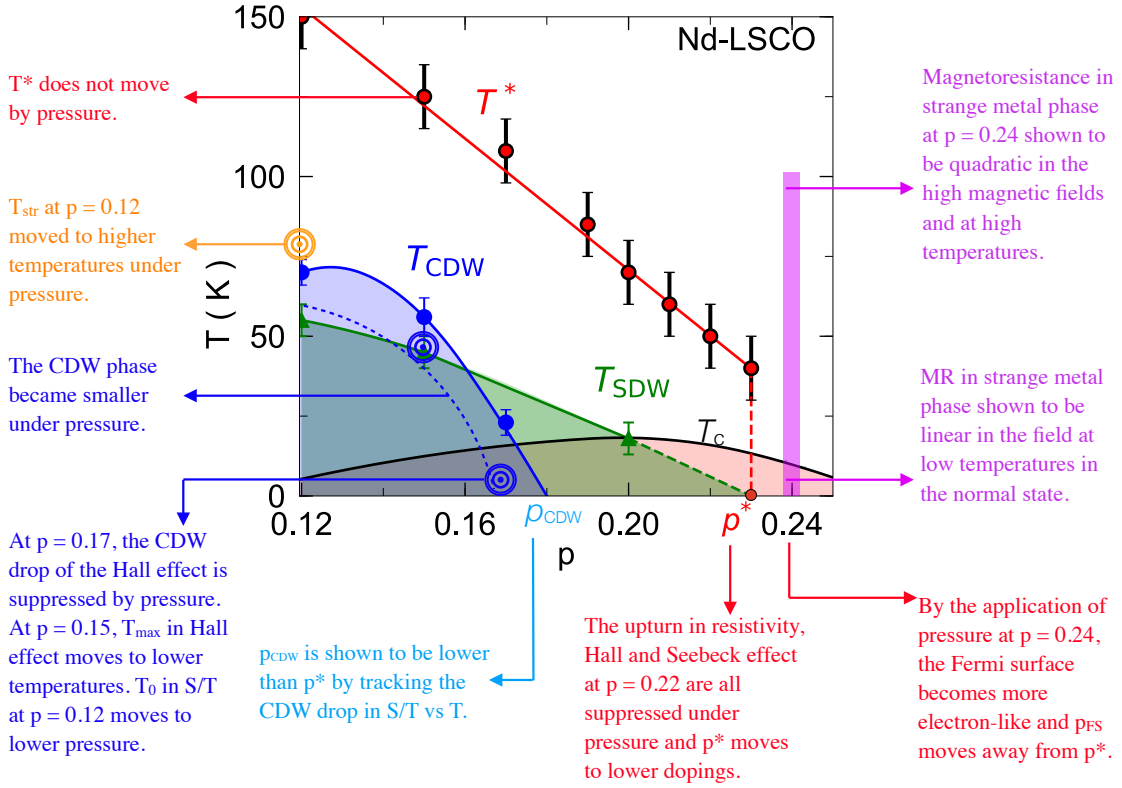

Figure 3.48 An overview of my results in the phase diagram of Nd-LSCO.

resistivity. Our results show that the resistivity has a quadratic field dependence, at high temperatures and a linear field dependence at low temperatures.

For an overview of my findings, see Figure 3.48.

To solve the puzzle of the cuprate superconductors and check the existing theories, plenty of necessary experiments left to be done in different forefronts of the condensed matter physics. However, a few interesting transport experiments that follow the research line of this thesis are:

1- Pressure effect at the two ends of the superconducting dome, to understand what controls T_c.
2- Study of the thermoelectric effect in Nd-LSCO near the doping of 0.12 in high magnetic fields and under pressure, to check the pressure effect on SDW and CDW phases.
3- Application of uniaxial strain along a-b plane in Nd-LSCO and study the anisotropic effect of pressure on Fermi surface both near p* and the doping of 0.12.
4- Application of higher pressures (up to 20GPa and more) at p = 0.12 to fully suppress

CDW, and see what happens to the Fermi surface in the pure pseudogap phase.
5- Application of higher pressure on Nd-LSCO at doping near p* and check how far p* can move down. To see if that p* of Nd-LSCO can go below the p* in LSCO, for example.

Appendix A

Pressure effect on Nd-LSCO p = 0.15

We are also interested in studying the pressure effect on the Hall effect upturn that appears in high magnetic fields at temperatures lower than the onset of the CDW downturn in Nd-LSCO p = 0.15 fig 3.8–b. So, we applied pressure on another Nd-LSCO p = 0.15 (called S2) and measured its Hall effect in high magnetic fields comparable to the field that was applied on another sample (S1) in ambient pressures. Figure A.1 shows this comparison. The upturn at 1.7 GPa and in 35T is not as dramatic as it used to be (at least down to 5K). One of the possible scenarios is that pressure moves the onset of SDW to lower temperatures. However, as the two samples are not identical (even though they came from the same batch), maybe there is a slight mismatch in the original onset of the upturn in the Hall effect. However, even if there is a mismatch, it is insignificant compared with the normal state temperature range that is accessible in 35T.

Furthermore, figA.1 shows that at 0GPa and in 16T, T_{max}—the onset of the temperature dependence of Hall coefficient drop— is located at 42K. Then at 35T and in 1.7 GPa, T_{max} moves to 35K. This suggests that pressure can move the CDW onset.

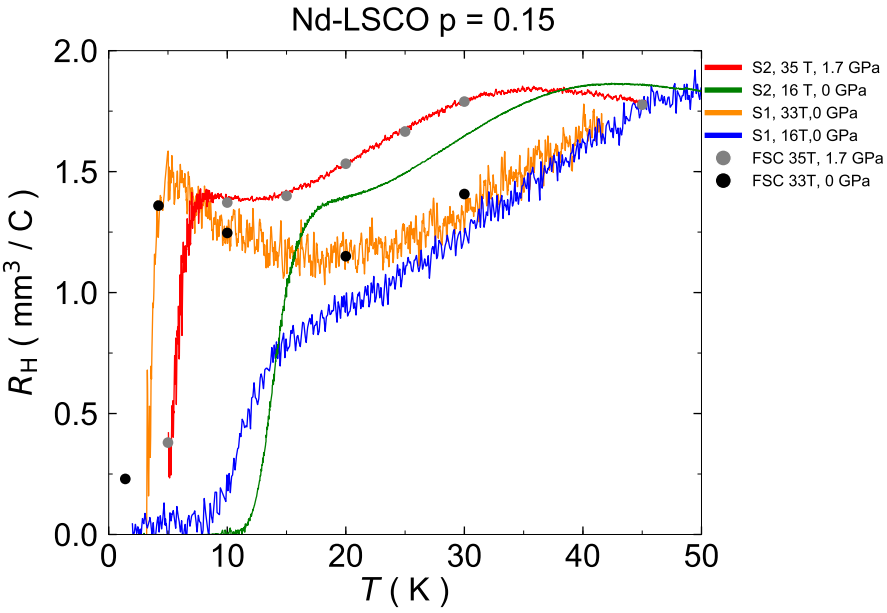

Figure A.1 Temperature dependence of Hall coefficient in two samples of Nd-LSCO p = 0.15 S1 (sample 1) which is the same data in fig3.8–b) and S2 (a new sample with the same doping) at the magnetic fields as indicated. Gray and black circles are the field sweep cuts (FSC) at different fields and pressures for S2 and S1 respectively.

Appendix B

Pressure effect on superconducting dome

To pursue the evolution of the superconducting dome under pressure, one can look at the very beginning of the T_c dome in the lightly doped Mott insulators and also at the very end of the dome in the heavily overdoped region. So far we applied pressure on the under-doped side of superconducting dome on Eu-LSCO at p = 0.08 with T_c = 2K and LSCO at p = 0.06 with T_c = 2.9K the T_c was measured with resistivity. Pressure effect is the same as in higher dopings dT_c/dP = 4 K/GPa.

Fig B.1 shows the temperature dependence of resistivity in Eu-LSCO at p = 0.08 at five different pressure points. The effect of pressure besides increasing the T_c, is to suppress the upturn. This upturn is both due to the pseudogap and some source of scattering that could be some sort of order due to the proximity with the AFM phase. Pressure increased either the mobility or the number of carriers and that caused the suppression of this upturn. However, the effect of pressure on the upturn of pseudogap at this doping must be studied by using another probe to see how the pseudogap is affected. Nevertheless, if one follows the same scenario that was discussed in chapter 3 for the suppression of pseudogap near p* and the shift in p*, without considering any other source of order that can affect the resistivity, one can conclude that p* is shifted upwards this time and goes farther from the endpoint of AFM.

Fig B.3 shows the temperature dependence of resistivity in LSCO at p = 0.06. The effect of pressure is the same as that of Eu-LSCO p = 0.08 for pressures higher than 6Kbar, but something must have happened to the sample after pressurization as the data at low temperature is not reproducible. This sample had old contacts at the time of this measurement, despite that, the contact resistance looked fine and it was less than 5 Ω, but maybe after pressurization, something has happened. Anyhow the effect of pressure seems to follow the same regime as in Eu-LSCO at p = 0.08, but at higher pressures, it might not be reliable.

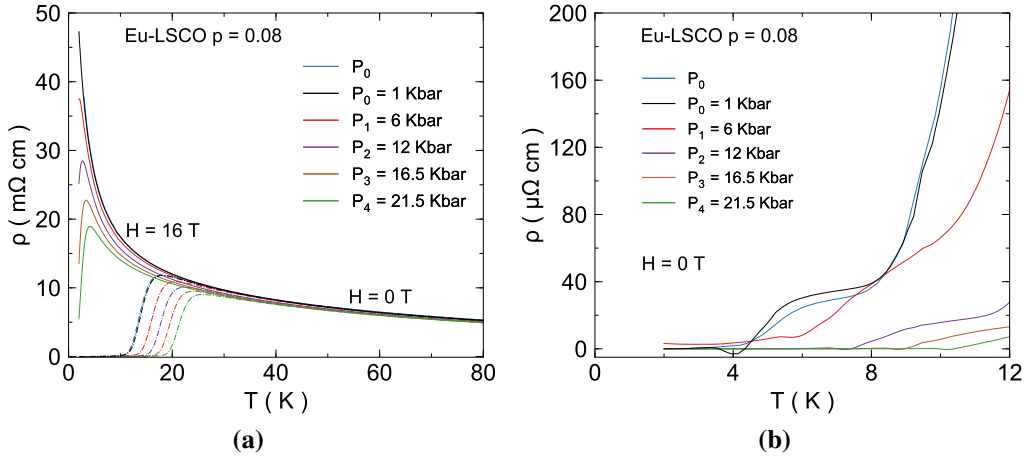

Figure B.1 a) Temperature dependence of resistivity in Eu-LSCO p = 0.08 at different pressures in 0 (dotted dashed lines) and 16 T (solid lines). Different colors are corresponding to different pressures. b) Enlargement of the same plot of (a).

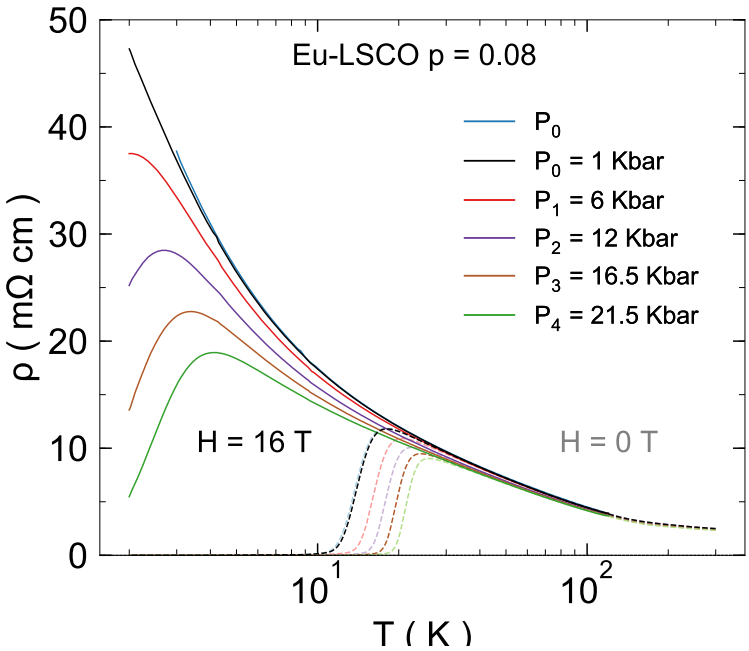

Figure B.2 Resistivity as a function of logarithm of resistivity in Eu-LSCO p = 0.08 at different pressures in 0 (dashed lines) and 16 T (solid lines).

We conclude that pressure suppresses the upturn of resistivity in LSCO which is a much stronger material compared to Nd or Eu-doped LSCO.

These results imply that the T_c increases with the same rate for a variety of dopings and one should apply pressure in lower dopings to check if the dome also enlarges in doping

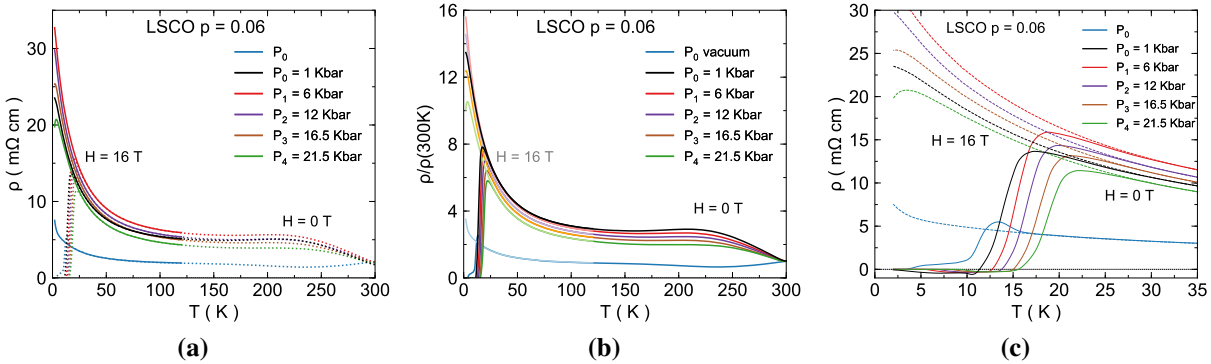

Figure B.3 a) Temperature dependence of resistivity in LSCO p = 0.06 at different pressures in 0 (dotted dashed lines) and 16 T (solid lines). Different colors are corresponding to different pressures. b) Same plot as (a) that the resistivity is normalized in $\rho(300)$ c) Enlargement of the same plot of (a).

or not. This research has fundamental importance in the boundary of phases near the AFM phase and the superconductivity. One of the main questions is: does superconductivity appear in the AFM phase by the application of pressure?

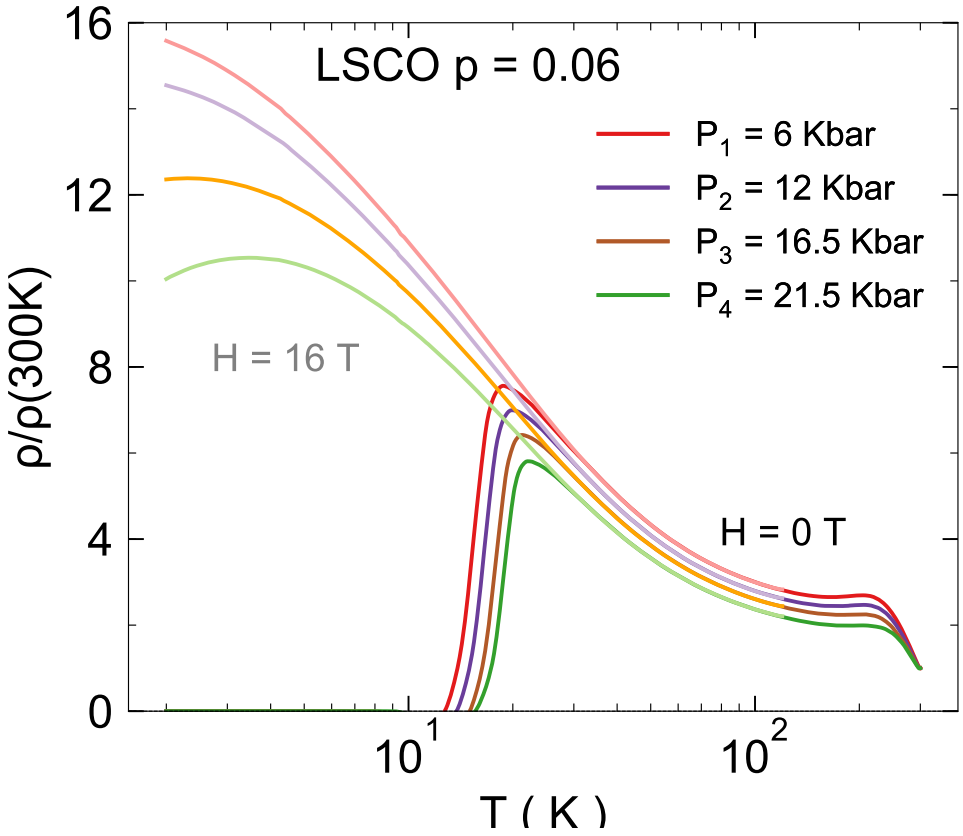

Figure B.4 Resistivity as a function of logarithm of resistivity in Eu-LSCO p = 0.06 at different pressures in 0 and 16 T.

Appendix C

Thermal conductivity on Nd-LSCO p=0.17 and 0.19

A comprehensive study on thermal conductivity of Nd-LSCO superconductors and verification of the Wiedemann-Franz law has been done recently [103]. We confirmed the findings of that paper in two different dopings of Nd-LSCO at p = 0.17 and 0.19 and concluded that in the low-temperature limit, the non-superconducting ground state of the pseudogap is a conventional metal.

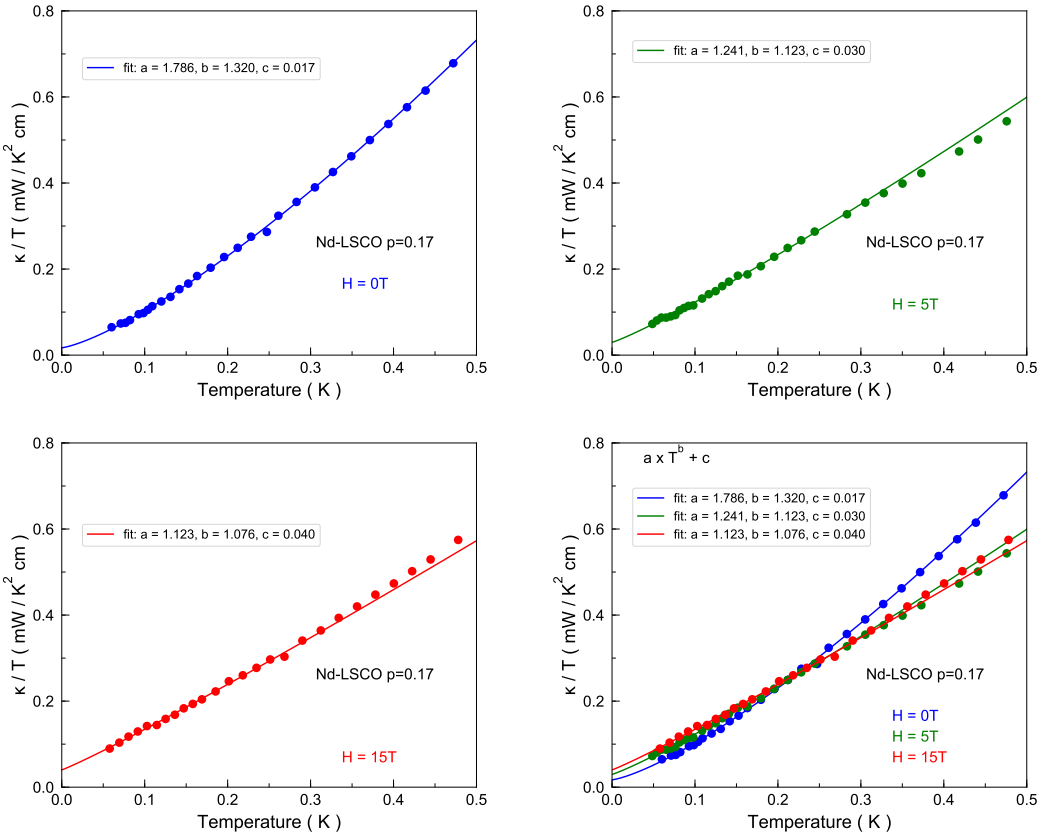

Figure C.1 Temperature dependence of thermal conductivity over temperature in Nd-LSCO at p = 0.17 in different magnetic fields as indicated. The data has been fitted with a power law function and the fitting function and parameters are shown. The fitting range is 50-300 mK

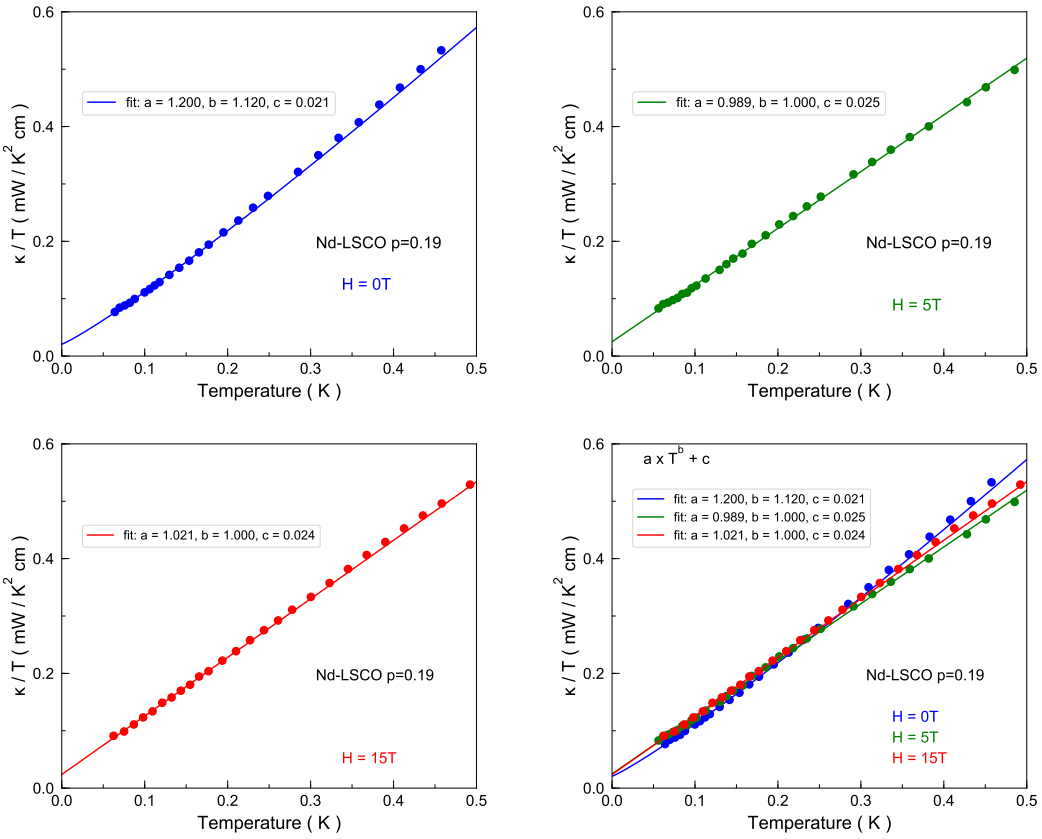

Figure C.2 Temperature dependence of thermal conductivity over temperature in Nd-LSCO at p = 0.19 in different magnetic fields as indicated. The data has been fitted with a power law function and the fitting function and parameters are shown. The value of b is set to 1 for all the curves and the fitting range is between 50-200 mK.

Appendix D

Electrical AC transport technique

By applying an AC current on a sample, an electric field of the form E = E_0 $e^{-i\omega t}$ is created. As the direction of the current changes, then the electrons accelerate back and forth within each cycle and they go trough random collisions with the average time of τ. Then a damping term adds to the $-e$E = m (dv/dt) (that is discussed in chapter 1) and it changes to the following form:

$$-eE = \frac{dp}{dt} + \frac{p}{\tau} \tag{D.1}$$

where p is the momentum and has the form p = mν_0 $e^{-i\omega t}$. By substituting it in equation D.1 ν_0 has the form:

$$\nu_0 = \frac{-eE_0}{m} \cdot \frac{\tau}{1 - i\omega\tau} \tag{D.2}$$

by using ν_0 of D.1 in 2.2 one can calculate the AC conductivity as:

$$\sigma = \frac{\sigma_0}{1 - i\omega\tau} \tag{D.3}$$

where σ_0 is DC conductivity. If ω = 0, it is the same as DC conductivity. When $\omega\tau$«1 eq keeps its periodic and oscillatory form meaning that the number of collisions is considerable and oscillatory. When $\omega\tau$»1 it means that excitation alternates faster than collision frequency which results in the dominance of imaginary part of conductance and appearance of capacitive impedance (reactive impedance) that is inversely proportional to the signal frequency.

We measured the resistivity with alternative excitations and there was no difference at all between temperature dependence of resistivity at different frequencies between 0 and 1000 Hz. As the plasma frequency of metals is of the order of 10 rad/fs [104] it means that in frequencies in the order of 100 terahertz we are approaching plasma gas limit above which the scattering rate becomes unimportant but if one applies lower frequencies with the period of the order of scattering rate, one could expect to observe the effect of that teraHertz AC current on periodic phases in cuprates such as CDW and SDW. Unfortunately, we did not have access to such a high-frequency current, but that could be interesting to investigate.

Another interesting item to investigate with AC current is the critical current of superconductors. As it was mentioned in chapter one, one of the ways for suppressing superconductivity is the application of high currents above the critical current. As there is finite resistance in the contacts that are connected to the superconductor sample and the critical current for cuprates is very high, one should be aware that they could simply warm up and induce significant uncertainty in the sample temperature. In order to minimize that effect, one should consider decreasing the time of measurement significantly which is possible in AC transport measurement option of Quantum Design PPMS, and it does not necessarily mean that one should necessarily apply AC current to measure critical current, it is also possible with DC current in a very short interval of time. The other thing that can help to decrease the magnitude of the applied current is to use a thin film as I_c should decrease by decreasing the thickness of the sample (much more effectively compared to changing other dimension's parameters) and J_c is independent of the geometry of the sample.

This could have another application other than just measuring the critical current itself. We can treat it as just a method for suppressing superconductivity just like when we suppress it in high magnetic fields. If one applies another current with the lower magnitude and in a different frequency, by locking a lock-in amplifier at this frequency, different electrical transport properties could be measured in the normal state.

If one still doubts that the sample temperature might not be exact, one could calibrate the resistivity data with normal state high field resistivity at given temperatures to make sure that the temperature difference is not significant. This method should be feasible in thin films without producing significant uncertainties in temperature (lower than 1K in low temperatures based on the resistivity of silver and typical size of contacts and wires) and it is very comparable to suppressing the superconductivity by the magnetic field, as the effect of the magnetic field is to induce electric current in a superconductor.

We experienced a systematic silver wire breaking on the samples by increasing the applied current higher than 500mA and that current was not enough in our thin film crystals to reach I_c. We used 25 and 50 μm silver wires and silver paste epoxy as it was explained in chapter two.

Bibliography

[1] Goldstone, J. *Il Nuovo Cimento (1955-1965)* **19**(1), 154–164 (1961).

[2] Zaanen, J. *ArXiv e-prints* July (2018).

[3] Lynton, E. *Superconductivity*. Wiley, (1969).

[4] Bardeen, J., Cooper, L. N., and Schrieffer, J. R. *Physical Review* **108**(5), 1175–1204 12 (1957).

[5] Drozdov, A. P., Eremets, M. I., Troyan, I. A., Ksenofontov, V., and Shylin, S. I. *Nature* **525**, 73 EP – 08 (2015).

[6] Cohen, M. L. and Anderson, P. W. *AIP Conference Proceedings* **4**(1), 17–27 2018/06/20 (1972).

[7] Anderson, P. W. *Science* **235**(4793), 1196 03 (1987).

[8] Cyr-Choinière, O., Daou, R., Laliberté, F., Collignon, C., Badoux, S., LeBoeuf, D., Chang, J., Ramshaw, B. J., Bonn, D. A., Hardy, W. N., Liang, R., Yan, J.-Q., Cheng, J.-G., Zhou, J.-S., Goodenough, J. B., Pyon, S., Takayama, T., Takagi, H., Doiron-Leyraud, N., and Taillefer, L. *Phys. Rev. B* **97**, 064502 Feb (2018).

[9] Matt, C. E., Fatuzzo, C. G., Sassa, Y., Mansson, M., Fatale, S., Bitetta, V., Shi, X., Pailhès, S., Berntsen, M. H., Kurosawa, T., Oda, M., Momono, N., Lipscombe, O. J., Hayden, S. M., Yan, J. Q., Zhou, J. S., Goodenough, J. B., Pyon, S., Takayama, T., Takagi, H., Patthey, L., Bendounan, A., Razzoli, E., Shi, M., Plumb, N. C., Radovic, M., Grioni, M., Mesot, J., Tjernberg, O., and Chang, J. *Physical Review B* **92**(13), 134524– 10 (2015).

[10] Haug, D., Hinkov, V., Sidis, Y., Bourges, P., Christensen, N. B., Ivanov, A., Keller, T., Lin, C. T., and Keimer, B. *New Journal of Physics* **12**(10), 105006 (2010).

[11] Wakimoto, S., Yamada, K., Tranquada, J. M., Frost, C. D., Birgeneau, R. J., and Zhang, H. *Phys. Rev. Lett.* **98**, 247003 Jun (2007).

[12] Moon, E. G. and Sachdev, S. *Physical Review B* **80**(3), 035117– 07 (2009).

[13] Tranquada, J. M., Sternlieb, B. J., Axe, J. D., Nakamura, Y., and Uchida, S. *Nature* **375**, 561 EP – 06 (1995).

[14] Comin, R., Sutarto, R., He, F., da Silva Neto, E. H., Chauviere, L., Fraño, A., Liang, R., Hardy, W. N., Bonn, D. A., Yoshida, Y., Eisaki, H., Achkar, A. J., Hawthorn, D. G., Keimer, B., Sawatzky, G. A., and Damascelli, A. *Nature Materials* **14**, 796 EP – 05 (2015).

[15] Comin, R., Sutarto, R., da Silva Neto, E. H., Chauviere, L., Liang, R., Hardy, W. N., Bonn, D. A., He, F., Sawatzky, G. A., and Damascelli, A. *Science* **347**(6228), 1335 03 (2015).

[16] Emery, V. J., Kivelson, S. A., and Tranquada, J. M. *Proceedings of the National Academy of Sciences* **96**(16), 8814–8817 (1999).

[17] Zachar, O., Kivelson, S. A., and Emery, V. J. *Physical Review B* **57**(3), 1422–1426 01 (1998).

[18] Platé, M., Mottershead, J. D. F., Elfimov, I. S., Peets, D. C., Liang, R., Bonn, D. A., Hardy, W. N., Chiuzbaian, S., Falub, M., Shi, M., Patthey, L., and Damascelli, A. *Phys. Rev. Lett.* **95**, 077001 Aug (2005).

[19] Benhabib, S., Sacuto, A., Civelli, M., Paul, I., Cazayous, M., Gallais, Y., Méasson, M.-A., Zhong, R. D., Schneeloch, J., Gu, G. D., Colson, D., and Forget, A. *Phys. Rev. Lett.* **114**, 147001 Apr (2015).

[20] Schmidt, A. R., Fujita, K., Kim, E.-A., Lawler, M. J., Eisaki, H., Uchida, S., Lee, D.-H., and Davis, J. C. *New Journal of Physics* **13**(6), 065014 (2011).

[21] Doiron-Leyraud, N., Proust, C., LeBoeuf, D., Levallois, J., Bonnemaison, J.-B., Liang, R., Bonn, D. A., Hardy, W. N., and Taillefer, L. *Nature* **447**, 565 EP – 05 (2007).

[22] LeBoeuf, D., Doiron-Leyraud, N., Levallois, J., Daou, R., Bonnemaison, J. B., Hussey, N. E., Balicas, L., Ramshaw, B. J., Liang, R., Bonn, D. A., Hardy, W. N., Adachi, S., Proust, C., and Taillefer, L. *Nature* **450**, 533 EP – 11 (2007).

[23] Tranquada, J. M., Axe, J. D., Ichikawa, N., Nakamura, Y., Uchida, S., and Nachumi, B. *Phys. Rev. B* **54**, 7489–7499 Sep (1996).

[24] Fujita, K., Hamidian, M. H., Edkins, S. D., Kim, C. K., Kohsaka, Y., Azuma, M., Takano, M., Takagi, H., Eisaki, H., Uchida, S.-i., Allais, A., Lawler, M. J., Kim, E.-A., Sachdev, S., and Davis, J. C. S. *Proceedings of the National Academy of Sciences* **111**(30), E3026–E3032 (2014).

[25] Achkar, A. J., Sutarto, R., Mao, X., He, F., Frano, A., Blanco-Canosa, S., Le Tacon, M., Ghiringhelli, G., Braicovich, L., Minola, M., Moretti Sala, M., Mazzoli, C., Liang, R., Bonn, D. A., Hardy, W. N., Keimer, B., Sawatzky, G. A., and Hawthorn, D. G. *Phys. Rev. Lett.* **109**, 167001 Oct (2012).

[26] Ghiringhelli, G., Le Tacon, M., Minola, M., Blanco-Canosa, S., Mazzoli, C., Brookes, N. B., De Luca, G. M., Frano, A., Hawthorn, D. G., He, F., Loew, T., Sala, M. M., Peets, D. C., Salluzzo, M., Schierle, E., Sutarto, R., Sawatzky, G. A., Weschke, E., Keimer, B., and Braicovich, L. *Science* **337**(6096), 821–825 (2012).

[27] Chang, J., Blackburn, E., Holmes, A. T., Christensen, N. B., Larsen, J., Mesot, J., Liang, R., Bonn, D. A., Hardy, W. N., Watenphul, A., Zimmermann, M. v., Forgan, E. M., and Hayden, S. M. *Nature Physics* **8**, 871 EP – 10 (2012).

[28] Wu, T., Mayaffre, H., Krämer, S., Horvatić, M., Berthier, C., Hardy, W. N., Liang, R., Bonn, D. A., and Julien, M.-H. *Nature* **477**, 191 EP – 09 (2011).

[29] Wu, T., Mayaffre, H., Krämer, S., Horvatić, M., Berthier, C., Hardy, W. N., Liang, R., Bonn, D. A., and Julien, M.-H. *Nature Communications* **6**, 6438 EP – 03 (2015).

[30] Yao, H., Lee, D.-H., and Kivelson, S. *Physical Review B* **84**(1), 012507– 07 (2011).

[31] Harrison, N. and Sebastian, S. E. *New Journal of Physics* **14**(9), 095023 (2012).

[32] Cyr-Choinière, O., LeBoeuf, D., Badoux, S., Dufour-Beauséjour, S., Bonn, D. A., Hardy, W. N., Liang, R., Graf, D., Doiron-Leyraud, N., and Taillefer, L. *Physical Review B* **98**(6), 064513– 08 (2018).

[33] Grissonnanche, G., Cyr-Choinière, O., Laliberté, F., Renéde Cotret, S., Juneau-Fecteau, A., Dufour-Beauséjour, S., Delage, M. È., LeBoeuf, D., Chang, J., Ramshaw, B. J., Bonn, D. A., Hardy, W. N., Liang, R., Adachi, S., Hussey, N. E., Vignolle, B., Proust, C., Sutherland, M., Krämer, S., Park, J. H., Graf, D., Doiron-Leyraud, N., and Taillefer, L. *Nature Communications* **5**, 3280 EP – 02 (2014).

[34] Norman, M. R., Pines, D., and Kallin, C. *Advances in Physics* **54**(8), 715–733 12 (2005).

[35] Li, J.-X., Wu, C.-Q., and Lee, D.-H. *Phys. Rev. B* **74**, 184515 Nov (2006).

[36] Souliou, S. M., Gretarsson, H., Garbarino, G., Bosak, A., Porras, J., Loew, T., Keimer, B., and Le Tacon, M. *Phys. Rev. B* **97**, 020503 Jan (2018).

[37] Alloul, H., Ohno, T., and Mendels, P. *Physical Review Letters* **63**(16), 1700–1703 10 (1989).

[38] Warren, W. W., Walstedt, R. E., Brennert, G. F., Cava, R. J., Tycko, R., Bell, R. F., and Dabbagh, G. *Physical Review Letters* **62**(10), 1193–1196 03 (1989).

[39] Marshall, D. S., Dessau, D. S., Loeser, A. G., Park, C.-H., Matsuura, A. Y., Eckstein, J. N., Bozovic, I., Fournier, P., Kapitulnik, A., Spicer, W. E., and Shen, Z. X. *Physical Review Letters* **76**(25), 4841–4844 06 (1996).

[40] Ding, H., Yokoya, T., Campuzano, J. C., Takahashi, T., Randeria, M., Norman, M. R., Mochiku, T., Kadowaki, K., and Giapintzakis, J. *Nature* **382**, 51 EP – 07 (1996).

[41] Loeser, A. G., Shen, Z. X., Dessau, D. S., Marshall, D. S., Park, C. H., Fournier, P., and Kapitulnik, A. *Science* **273**(5273), 325 07 (1996).

[42] Lee, W. S., Vishik, I. M., Tanaka, K., Lu, D. H., Sasagawa, T., Nagaosa, N., Devereaux, T. P., Hussain, Z., and Shen, Z. X. *Nature* **450**, 81 EP – 11 (2007).

[43] Collignon, C., Badoux, S., Afshar, S. A. A., Michon, B., Laliberté, F., Cyr-Choinière, O., Zhou, J.-S., Licciardello, S., Wiedmann, S., Doiron-Leyraud, N., and Taillefer, L. *Phys. Rev. B* **95**, 224517 Jun (2017).

[44] Varma, C. M., Littlewood, P. B., Schmitt-Rink, S., Abrahams, E., and Ruckenstein, A. E. *Physical Review Letters* **63**(18), 1996–1999 10 (1989).

[45] Legros, A., Benhabib, S., Tabis, W., Laliberté, F., Dion, M., Lizaire, M., Vignolle, B., Vignolles, D., Raffy, H., Li, Z. Z., Auban-Senzier, P., Doiron-Leyraud, N., Fournier, P., Colson, D., Taillefer, L., and Proust, C. *ArXiv:1805.02512, Nature physics (in press)* (2019).

[46] Cooper, R. A., Wang, Y., Vignolle, B., Lipscombe, O. J., Hayden, S. M., Tanabe, Y., Adachi, T., Koike, Y., Nohara, M., Takagi, H., Proust, C., and Hussey, N. E. *Science* **323**(5914), 603–607 (2009).

[47] Marel, D. v. d., Molegraaf, H. J. A., Zaanen, J., Nussinov, Z., Carbone, F., Damascelli, A., Eisaki, H., Greven, M., Kes, P. H., and Li, M. *Nature* **425**, 271 EP – 09 (2003).

[48] Giraldo-Gallo, P., Galvis, J. A., Stegen, Z., Modic, K. A., Balakirev, F. F., Betts, J. B., Lian, X., Moir, C., Riggs, S. C., Wu, J., Bollinger, A. T., He, X., Božović, I., Ramshaw, B. J., McDonald, R. D., Boebinger, G. S., and Shekhter, A. *Science* **361**(6401), 479–481 (2018).

[49] Ito, T., Takenaka, K., and Uchida, S. *Physical Review Letters* **70**(25), 3995–3998 06 (1993).

[50] Croft, T. P., Lester, C., Senn, M. S., Bombardi, A., and Hayden, S. M. *Phys. Rev. B* **89**, 224513 Jun (2014).

[51] Laliberté, F., Chang, J., Doiron-Leyraud, N., Hassinger, E., Daou, R., Rondeau, M., Ramshaw, B. J., Liang, R., Bonn, D. A., Hardy, W. N., Pyon, S., Takayama, T., Takagi, H., Sheikin, I., Malone, L., Proust, C., Behnia, K., and Taillefer, L. *Nature Communications* **2**, 432 EP – 08 (2011).

[52] Badoux, S., Afshar, S. A. A., Michon, B., Ouellet, A., Fortier, S., LeBoeuf, D., Croft, T. P., Lester, C., Hayden, S. M., Takagi, H., Yamada, K., Graf, D., Doiron-Leyraud, N., and Taillefer, L. *Phys. Rev. X* **6**, 021004 Apr (2016).

[53] LeBoeuf, D., Doiron-Leyraud, N., Vignolle, B., Sutherland, M., Ramshaw, B. J., Levallois, J., Daou, R., Laliberté, F., Cyr-Choinière, O., Chang, J., Jo, Y. J., Balicas, L., Liang, R., Bonn, D. A., Hardy, W. N., Proust, C., and Taillefer, L. *Phys. Rev. B* **83**, 054506 Feb (2011).

[54] LeBoeuf, D., Doiron-Leyraud, N., Levallois, J., Daou, R., Bonnemaison, J. B., Hussey, N. E., Balicas, L., Ramshaw, B. J., Liang, R., Bonn, D. A., Hardy, W. N., Adachi, S., Proust, C., and Taillefer, L. *Nature* **450**, 533 EP – 11 (2007).

[55] Ando, Y., Komiya, S., Segawa, K., Ono, S., and Kurita, Y. *Physical Review Letters* **93**(26), 267001– 12 (2004).

[56] Segawa, K. and Ando, Y. *Physical Review B* **69**(10), 104521– 03 (2004).

[57] Ong, N. P. *Physical Review B* **43**(1), 193–201 01 (1991).

[58] Ando, Y., Kurita, Y., Komiya, S., Ono, S., and Segawa, K. *Physical Review Letters* **92**(19), 197001– 05 (2004).

[59] Chang, J., Daou, R., Proust, C., LeBoeuf, D., Doiron-Leyraud, N., Laliberté, F., Pingault, B., Ramshaw, B. J., Liang, R., Bonn, D. A., Hardy, W. N., Takagi, H., Antunes, A. B., Sheikin, I., Behnia, K., and Taillefer, L. *Physical Review Letters* **104**(5), 057005–02 (2010).

[60] Taillefer, L. *Journal of Physics: Condensed Matter* **21**(16), 164212 (2009).

[61] Behnia, K. and HervéAubin. *Reports on Progress in Physics* **79**(4), 046502 (2016).

[62] Chu, C. W., Gao, L., Chen, F., Huang, Z. J., Meng, R. L., and Xue, Y. Y. *Nature* **365**, 323 EP – 09 (1993).

[63] Bianconi, A., Saini, N. L., Lanzara, A., Missori, M., Rossetti, T., Oyanagi, H., Yamaguchi, H., Oka, K., and Ito, T. *Physical Review Letters* **76**(18), 3412–3415 04 (1996).

[64] Hücker, M., v. Zimmermann, M., Gu, G. D., Xu, Z. J., Wen, J. S., Xu, G., Kang, H. J., Zheludev, A., and Tranquada, J. M. *Physical Review B* **83**(10), 104506– 03 (2011).

[65] Crawford, M. K., Harlow, R. L., Deemyad, S., Tissen, V., Schilling, J. S., McCarron, E. M., Tozer, S. W., Cox, D. E., Ichikawa, N., Uchida, S., and Huang, Q. *Phys. Rev. B* **71**, 104513 Mar (2005).

[66] Rogalla, H. and Kes, P. H. *100 Years of Superconductivity*. CRC Press, (2011).

[67] Bednorz, J. G. and Müller, K. A. *Zeitschrift für Physik B Condensed Matter* **64**(2), 189–193 (1986).

[68] Hücker, M., v. Zimmermann, M., Debessai, M., Schilling, J. S., Tranquada, J. M., and Gu, G. D. *Physical Review Letters* **104**(5), 057004– 02 (2010).

[69] Axe, J. D., Moudden, A. H., Hohlwein, D., Cox, D. E., Mohanty, K. M., Moodenbaugh, A. R., and Xu, Y. *Physical Review Letters* **62**(23), 2751–2754 06 (1989).

[70] Guguchia, Z., Maisuradze, A., Ghambashidze, G., Khasanov, R., Shengelaya, A., and Keller, H. *New Journal of Physics* **15**(9), 093005 (2013).

[71] Chaikin, P. M., Weyl, C., Malfait, G., and Jérome, D. *Review of Scientific Instruments* **52**(9), 1397–1399 (1981).

[72] Arsenijević, S., Gaál, R., Sefat, A. S., McGuire, M. A., Sales, B. C., Mandrus, D., and Forró, L. *Physical Review B* **84**(7), 075148– 08 (2011).

[73] Zhou, J. S. and Goodenough, J. B. *Physical Review Letters* **77**(1), 151–154 07 (1996).

[74] Zhou, J. S., Goodenough, J. B., Dabrowski, B., and Rogacki, K. *Physical Review Letters* **77**(20), 4253–4256 11 (1996).

[75] Itskevich, E. S., Kraidenov, V. F., and Kuzemskaya, I. G. *Journal of Experimental and Theoretical Physics* **91**(3), 562–567 (2000).

[76] Zhou, J. S., Archibald, W., and Goodenough, J. B. *Physical Review B* **57**, R2017 (1998).

[77] Arumugam, S., Môri, N., Takeshita, N., Takashima, H., Noda, T., Eisaki, H., and Uchida, S. *Physical Review Letters* **88**(24), 247001– 05 (2002).

[78] Ashcroft, N. and Mermin, N. *Solid State Physics*. Saunders College, (1976).

[79] Eiling, A. and Schilling, J. S. *Journal of Physics F: Metal Physics* **11**(3), 623 (1981).

[80] Walker, I. R. *Review of Scientific Instruments* **70**(8), 3402–3412 (1999).

[81] Chaikin, P. M. and Kwak, J. F. *Review of Scientific Instruments* **46**(2), 218–220 (1975).

[82] Choi, E. S., Kang, H., Jo, Y. J., and Kang, W. *Review of Scientific Instruments* **73**(8), 2999–3002 (2002).

[83] Doiron-Leyraud, N., Badoux, S., Renéde Cotret, S., Lepault, S., LeBoeuf, D., Laliberté, F., Hassinger, E., Ramshaw, B. J., Bonn, D. A., Hardy, W. N., Liang, R., Park, J. H. ., Vignolles, D., Vignolle, B., Taillefer, L., and Proust, C. *Nature Communications* **6**, 6034 EP – 01 (2015).

[84] Harrison, N. and Sebastian, S. E. *Phys. Rev. B* **92**, 224505 Dec (2015).

[85] Badoux, S., Tabis, W., Laliberté, F., Grissonnanche, G., Vignolle, B., Vignolles, D., Béard, J., Bonn, D. A., Hardy, W. N., Liang, R., Doiron-Leyraud, N., Taillefer, L., and Proust, C. *Nature* **531**, 210 EP – 02 (2016).

[86] Collignon, C. *De la densité des fluides électroniques dans deux oxydes supraconducteurs*. PhD thesis, Université de Sherbrooke and École Supérieure de Physique et de Chimie Industrielles (CNRS), (2017).

[87] Daou, R., Cyr-Choinière, O., Laliberté, F., LeBoeuf, D., Doiron-Leyraud, N., Yan, J.-Q., Zhou, J.-S., Goodenough, J. B., and Taillefer, L. *Phys. Rev. B* **79**, 180505 May (2009).

[88] Sadewasser, S., Schilling, J. S., Paulikas, A. P., and Veal, B. W. *Phys. Rev. B* **61**, 741–749 Jan (2000).

[89] Balakirev, F. F., Betts, J. B., Migliori, A., Tsukada, I., Ando, Y., and Boebinger, G. S. *Phys. Rev. Lett.* **102**, 017004 (2009).

[90] LeBoeuf, D., Doiron-Leyraud, N., Levallois, J., Daou, R., Bonnemaison, J. B., Hussey, N. E., Balicas, L., Ramshaw, B. J., Liang, R., Bonn, D. A., Hardy, W. N., Adachi, S., Proust, C., and Taillefer, L. *Nature* **450**, 533–536 (2007).

[91] Doiron-Leyraud, N., Cyr-Choinière, O., Badoux, S., Ataei, A., Collignon, C., Gourgout, A., Dufour-Beauséjour, S., Tafti, F. F., Laliberté, F., Boulanger, M. E., Matusiak, M., Graf, D., Kim, M., Zhou, J. S., Momono, N., Kurosawa, T., Takagi, H., and Taillefer, L. *Nature Communications* **8**(1), 2044 (2017).

[92] Axe, J. D. and Crawford, M. K. *Journal of Low Temperature Physics* **95**(1), 271–284 (1994).

[93] Fink, J., Soltwisch, V., Geck, J., Schierle, E., Weschke, E., and Büchner, B. *Physical Review B* **83**(9), 092503– 03 (2011).

[94] Rullier-Albenque, F., Alloul, H., Balakirev, F., and Proust, C. *EPL (Europhysics Letters)* **81**(3), 37008 (2008).

[95] Laliberte, F., Tabis, W., Badoux, S., Vignolle, B., Destraz, D., Momono, N., Kurosawa, T., Yamada, K., Takagi, H., Doiron-Leyraud, N., Proust, C., and Taillefer, L. *arXiv:1606.04491* (2016).

[96] Daou, R., Doiron-Leyraud, N., LeBoeuf, D., Li, S. Y., Laliberté, F., Cyr-Choinière, O., Jo, Y. J., Balicas, L., Yan, J. Q., Zhou, J. S., Goodenough, J. B., and Taillefer, L. *Nature Physics* **5**, 31 EP – 11 (2008).

[97] Tsukada, I. and Ono, S. *Physical Review B* **74**(13), 134508– 10 (2006).

[98] Analytis, J. G., Kuo, H.-H., McDonald, R. D., Wartenbe, M., Rourke, P. M. C., Hussey, N. E., and Fisher, I. R. *Nature Physics* **10**, 194 EP – 01 (2014).

[99] Nakamae, S., Behnia, K., Mangkorntong, N., Nohara, M., Takagi, H., Yates, S. J. C., and Hussey, N. E. *Phys. Rev. B* **68**, 100502 Sep (2003).

[100] Singleton, J. *ArXiv e-prints* October (2018).

[101] Hayes, I. M., McDonald, R. D., Breznay, N. P., Helm, T., Moll, P. J. W., Wartenbe, M., Shekhter, A., and Analytis, J. G. *Nature Physics* **12**, 916 EP – 05 (2016).

[102] Grissonnanche, G., Cyr-Choinière, O., Laliberté, F., Renéde Cotret, S., Juneau-Fecteau, A., Dufour-Beauséjour, S., Delage, M. È., LeBoeuf, D., Chang, J., Ramshaw, B. J., Bonn, D. A., Hardy, W. N., Liang, R., Adachi, S., Hussey, N. E., Vignolle, B., Proust, C., Sutherland, M., Krämer, S., Park, J. H., Graf, D., Doiron-Leyraud, N., and Taillefer, L. *Nature Communications* **5**, 3280 EP – 02 (2014).

[103] Michon, B., Ataei, A., Bourgeois-Hope, P., Collignon, C., Li, S. Y., Badoux, S., Gourgout, A., Laliberté, F., Zhou, J.-S., Doiron-Leyraud, N., and Taillefer, L. *Phys. Rev. X* **8**, 041010 Oct (2018).

[104] Poole, C. P., Prozorov, R., Farach, H. A., Creswick, R. J., Poole, C. P., Farach, H. A., and Creswick, R. J. *Superconductivity (Third Edition)*. Elsevier, London, (2014).